Proposal for the NuPRISM Experiment in the J-PARC Neutrino Beamline

S. Bhadra,[28] A. Blondel,[4] S. Bordoni,[7] A. Bravar,[4] C. Bronner,[10] R.G. Calland,[10] J. Caravaca Rodríguez,[7] M. Dziewiecki,[27] M. Ericson,[12,3] T. Feusels,[1] G.A. Fiorentini Aguirre,[28] L. Haegel,[4] M. Hartz,[10,26] R. Henderson,[26] T. Ishida,[6,*] M. Ishitsuka,[23] C.K. Jung,[14,†] A.C. Kaboth,[29,19] H. Kakuno,[24] H. Kamano,[16] A. Konaka,[26] Y. Kudenko,[9,‡] R. Kurjata,[27] M. Kuze,[23] T. Lindner,[26] K. Mahn,[13] M. Malek,[30] J.F. Martin,[25] M. Martini,[5] J. Marzec,[27] K.S. McFarland,[18] S. Nakayama,[21,†] T. Nakaya,[11,10] S. Nakamura,[15] Y. Nishimura,[22] A. Rychter,[27] F. Sánchez,[7] T. Sato,[15] M. Scott,[26] T. Sekiguchi,[6,*] T. Shima,[16] M. Shiozawa,[21,10] T. Sumiyoshi,[24] R. Tacik,[17,26] H.K. Tanaka,[21,†] H.A. Tanaka,[25,§] S. Tobayama,[1] M. Vagins,[10,2] C. Vilela,[14] J. Vo,[7] D. Wark,[19,8] M.O. Wascko,[8] M.J. Wilking,[14] S. Yen,[26] M. Yokoyama,[20,†] and M. Ziembicki[27]

(The NuPRISM Collaboration)

[1] *University of British Columbia, Department of Physics and Astronomy, Vancouver, British Columbia, Canada*
[2] *University of California, Irvine, Department of Physics and Astronomy, Irvine, California, U.S.A.*
[3] *Physics Department, Theory Unit, CERN, Geneva, Switzerland*
[4] *University of Geneva, Section de Physique, DPNC, Geneva, Switzerland*
[5] *Department of Physics and Astronomy, Ghent University, Gent, Belgium*
[6] *High Energy Accelerator Research Organization (KEK), Tsukuba, Ibaraki, Japan*
[7] *Institut de Fisica d'Altes Energies (IFAE), Bellaterra (Barcelona), Spain*
[8] *Imperial College London, Department of Physics, London, United Kingdom*
[9] *Institute for Nuclear Research of the Russian Academy of Sciences, Moscow, Russia*
[10] *Kavli Institute for the Physics and Mathematics of the Universe (WPI), Todai Institutes for Advanced Study, University of Tokyo, Kashiwa, Chiba, Japan*
[11] *Kyoto University, Department of Physics, Kyoto, Japan*
[12] *Université de Lyon, Université Claude Bernard Lyon 1, IPN Lyon (IN2P3), Villeurbanne, France*
[13] *Michigan State University, Department of Physics and Astronomy, East Lansing, Michigan, U.S.A.*
[14] *State University of New York at Stony Brook, Department of Physics and Astronomy, Stony Brook, New York, U.S.A.*
[15] *Osaka University, Department of Physics, Osaka, Toyonaka, Japan*
[16] *Osaka University, Research Center for Nuclear Physics(RCNP), Ibaraki, Osaka, Japan*
[17] *University of Regina, Department of Physics, Regina, Saskatchewan, Canada*
[18] *University of Rochester, Department of Physics and Astronomy, Rochester, New York, U.S.A.*
[19] *STFC, Rutherford Appleton Laboratory, Harwell Oxford, and Daresbury Laboratory, Warrington, United Kingdom*
[20] *University of Tokyo, Department of Physics, Tokyo, Japan*
[21] *University of Tokyo, Institute for Cosmic Ray Research, Kamioka Observatory, Kamioka, Japan*
[22] *University of Tokyo, Institute for Cosmic Ray Research, Research Center for Cosmic Neutrinos, Kashiwa, Japan*
[23] *Tokyo Institute of Technology, Department of Physics, Tokyo, Japan*
[24] *Tokyo Metropolitan University, Department of Physics, Tokyo, Japan*
[25] *University of Toronto, Department of Physics, Toronto, Ontario, Canada*
[26] *TRIUMF, Vancouver, British Columbia, Canada*
[27] *Warsaw University of Technology, Institute of Radioelectronics, Warsaw, Poland*
[28] *York University, Department of Physics and Astronomy, Toronto, Ontario, Canada*
[29] *Royal Holloway University of London, Department of Physics, Egham, Surrey, United Kingdom*
[30] *University of Sheffield, Department of Physics and Astronomy, Sheffield, United Kingdom*

(Dated: July 7, 2016)

As long-baseline neutrino experiments enter the precision era, the difficulties associated with understanding neutrino interaction cross sections on atomic nuclei are expected to limit experimental sensitivities to neutrino oscillation parameters. The ability to relate experimental observables to the incident neutrino energy relies on uncertain theoretical models of neutrino-nucleus interactions that are not well-constrained with traditional near detectors. In addition, these near detectors only measure ν_μ and $\overline{\nu}_\mu$ interactions, and the relationship between these events and the ν_e and $\bar{\nu}_e$ events that are used to measure CP violation is largely unconstrained by existing near detector data.

By observing charged current ν_μ interactions over a continuous range of off-axis angles from 1° to 4°, the NuPRISM water Cherenkov detector can provide a direct measurement of the relationship between neutron energy and lepton kinematics, which largely removes neutrino interaction modeling uncertainties from T2K oscillation measurements. By measuring a high-statistics

* also at J-PARC, Tokai, Japan

† affiliated member at Kavli IPMU (WPI), the University of Tokyo, Japan

‡ also at Moscow Institute of Physics and Technology and National Research Nuclear University "MEPhI", Moscow, Russia

§ also at Institute of Particle Physics, Canada

ν_e sample, NuPRISM can provide a data-driven constraint on the ν_e/ν_μ cross section ratio. Together, these measurements can enhance the T2K sensitivity to CP violation. Beyond the long baseline oscillation physics, NuPRISM is a sensitive probe of sterile neutrino oscillations with multiple energy spectra, which provides unique constraints on possible background-related explanations of the MiniBooNE anomaly, and NuPRISM can make high-precision measurements of neutrino cross sections on water, such as the first ever measurements of neutral current interactions as a function of neutrino energy. Finally, NuPRISM is the ideal detector for calibrating neutron emission and capture rates for SK-Gd, and for measuring backgrounds to proton decay searches.

The NuPRISM detector consists of an instrumented volume of water that can move vertically within a tall water cavity. Prior to the construction of the vertical water cavity, it is possible to begin the project with a "NuPRISM phase 0", in which the instrumented water volume is constructed first and operated on the surface near ND280. In this configuration, it is possible make low-background measurements of ν_e interactions, detailed measurements of neutron capture on Gd from charged current interactions, and provides an easily accessible setup for commissioning the detector calibration and verifying the detector modeling.

The NuPRISM detector also provides significant benefits to the proposed Hyper-Kamiokande project. A demonstration that neutrino interaction uncertainties can be controlled will be important to understanding the physics reach of Hyper-K. In addition, NuPRISM will provide an easily accessible prototype detector for many of the new hardware components currently under consideration for Hyper-K. The following document presents the configuration, physics impact, and preliminary cost estimates for a NuPRISM detector in the J-PARC neutrino beamline.

CONTENTS

I. NUPRISM UPDATES AND DEVELOPMENTS IN THE FUTURE NEUTRINO PROGAM SINCE THE ORIGINAL PROPOSAL

The NuPRISM experiment at J-PARC was first proposed at the previous J-PARC PAC meeting in July, 2015 [1]. The proposal was deferred pending further clarity about the future neutrino program at J-PARC.

Since that time, there have been several important developments regarding the intermediate Japanese neutrino physics program (i.e. prior to the Hyper-Kamiokande era). The T2K experiment is proposing, at the upcoming July, 2016 PAC meeting, to extend its data taking run to 20×10^{21} POT in an attempt to achieve a 3 σ measurement of CP violation. To reach 3 σ CPV sensitivity, T2K will need to achieve 2-3% systematic uncertainties. The dominant uncertainties are expected to come from the $\sigma_{\nu_e}/\sigma_{\nu_\mu}$ cross section ratios, final state interactions within the target nucleus, and nuclear effects. Currently, these uncertainties rely on theoretical model calculations, and it will be challenging to constrain them to the necessary precision with near detector measurements. In order to make a robust claim of 3 σ evidence for CPV, these uncertainties should be constrained experimentally.

The other major development since the initial proposal is the decision by the Super-Kamiokande collaboration to approve the future loading of gadolinium in the SK detector to enhance the efficiency of neutron capture (SK-Gd). This new capability has the potential to significantly reduce atmospheric neutrino backgrounds to proton decay searches, and to provide an additional mechanism to separate neutrinos and anti-neutrinos in both SK atmospheric neutrinos and T2K, which can enhance the sensitivity to the neutrino mass hierarchy and CP violation (CPV), respectively. However, these improvements rely on a precise knowledge of neutron emission cross sections in neutrino and anti-neutrino interactions, which are currently poorly understood. NuPRISM is an ideal experiment for measuring neutron emission and capture in a Gd-loaded water Cherenkov detector, since the neutron signal can be measured as a function of incident neutrino energy and final state lepton kinematics.

To better explain the NuPRISM contribution to the physics programs of T2K-II and SK-Gd, and to document new developments in the NuPRISM physics studies and program since previous PAC meetings, the following sections of this proposal have been updated:

- An updated description of T2K systematic errors has been included in the introduction in Section II.
- New tools for the detector simulation and event reconstruction are introduced in Section III C.
- New plots of the prediced E_{rec} distributions in the ν_μ disappearance analysis are included in Section III F.
- The new Section III G describes the the impact of NuPRISM on the T2K-II CP violation measurement.
- The sterile neutrino sensitivities in Section III H have been updated for the T2K phase-II exposure.
- A new section on Gd measurements in NuPRISM, Section III K, has been added.
- The option for a phased approach for NuPRISM construction and operation is introduced in Section VI. This section includes the discussion of a phased scenario where the stationary NuPRISM detector is first operated on the surface near the existing 280 m near detector site as Phase 0. The subsequent phase of NuPRISM would include the construction of the NuPRISM vertical water shaft and installation of the detector in the vertical water shaft.

NuPRISM is seeking stage-1 status at the July, 2016 PAC meeting to start the process of developing a full technical design for the detector. In order to determine the feasibility of constructing NuPRISM in time for T2K-II, J-PARC resources are needed to investigate possible off-site locations for the detector, and to refine the cost estimates for the new facility.

Appendix B includes a brief description of the grant requests to international funding agencies to realize the NuPRISM program.

II. INTRODUCTION

With the publications of the first ever observation of ν_e appearance, and the world's most precise measurement of θ_{23}, T2K has achieved its initial experimental goals with only 8.5% of the approved protons on target (POT) [2]. The next phase of the experiment will make even more precise measurements of ν_e appearance and ν_μ disappearance using both neutrinos and anti-neutrinos in order to probe the value of δ_{CP}, the θ_{23} octant, and $\left|\Delta m^2_{32}\right|$. In conjunction with measurements from NOνA, these measurements may also provide a constraint on the neutrino mass hierarchy.

In order to achieve these goals, a more precise understanding of neutrino interaction cross sections is required. Currently, T2K is forced to rely on neutrino interaction models to translate experimental observables at SK into measurements of neutrino oscillation parameters. The current T2K near detector, ND280, measures unoscillated neutrino spectra, which differ from the oscillated spectra at SK. At ND280, the ν_μ spectrum is peaked at the 600 MeV oscillation maximum, while at SK, there is a dip in the ν_μ spectrum at the oscillation maximum. The CP violation signal relies on measurements of ν_e and $\bar{\nu}_e$ at SK, but at ND280 there are no oscillated ν_e events, so it is difficult to acquire sufficient ν_e statistics to constrain ν_e cross sections.

The least constrained component of these neutrino interaction models is the relationship between the experimentally observable lepton kinematics and the energy of the incident neutrino. Current estimates, based solely on new, recently developed models, suggest that this bias may be one of T2K's largest systematic uncertainties, and ND280 cannot provide a constraint on this uncertainty in a manner that does not rely on neutrino interaction models. Had neutrino interaction models been trusted to provide this relationship just 5 years ago, current models suggest that 20 to 30% of events where only the final state lepton was observed would have been reconstructed with an incorrect neutrino energy in a way that would not have been constrained or even detectable. Even a high-performance near detector, capable of precisely measuring all charged particles in the final state, would be forced to rely on additional theoretical relationships between lepton kinematics and hadronic final states, and no modern theoretical models offer a detailed calculation for such a relationship within a nuclear environment.

The NuPRISM water-Cherenkov detector takes advantage of the energy dependence of the neutrino flux with off-axis angle by spanning a continuous range of 1 to 4 degrees in off-axis angle. This technique has the potential to significantly reduce uncertainties from neutrino interaction modeling in the T2K oscillation analyses, as is demonstrated for the muon neutrino disappearance measurement described in Section III. In particular, these measurements will provide the first direct experimental constraint on the relationship between lepton kinematics and neutrino energy using measurements of final state muons at many different off-axis angles. In order to construct a more cost-effective detector that can reasonably be built on a timescale that is applicable to T2K, this document proposes to instrument a subset of the full water volume on a frame that moves vertically within the water tank, which sequentially samples the full off-axis range of the shaft in 5-6 separate running periods.

A large water-Cherenkov detector 1 km from a 600 MeV neutrino source is also an ideal experiment to search for sterile neutrino oscillations at Δm^2 of $\sim$1 eV^2. NuPRISM can provide additional constraints on explanations for the MiniBooNE low-energy excess, since the oscillation signature and the backgrounds vary differently as a function of off-axis angle. NuPRISM can provide a complementary measurement of comparable sensitivity to the Fermilab short-baseline LAr program.

The construction of a NuPRISM detector in the next 3-5 years can also provide significant benefits to Hyper-Kamiokande (Hyper-K). The problems with understanding neutrino interactions can have a larger impact on Hyper-K, since Hyper-K will have much smaller statistical errors, and a demonstration that these uncertainties can be managed with a NuPRISM near detector will significantly enhance the physics case for Hyper-K. In addition, NuPRISM is an easily accessible water Cherenkov detector that provides an ideal environment to test Hyper-K technology. Hyper-K proposes to use new, in-water electronics, new high-voltage box-and-line PMTs, additional photosensors from foreign sources, such as KM3NeT-style multi-PMTs, and a new tank and liner construction to prevent leaks, all of which require extensive testing in a prototype detector. Finally, NuPRISM will provide an intermediate physics program that bridges the gap from T2K phase I to Hyper-K, which can provide continuity within the Japanese physics community while Hyper-K is being designed and constructed.

The remainder of this document provides an overview of the detector components and physics potential of NuPRISM. The results for a full T2K ν_μ disappearance analysis are provided, as well as a discussion of how NuPRISM can measure ν_e events to reduce the systematic uncertainty on δ_{CP}. Cost estimates have been obtained for the items that are expected to dominate the cost of the project, in particular photomultiplier tubes (PMTs) and civil construction. For the additional less expensive items, cost estimates from a very similar project proposed in 2005, the T2K 2 km water Cherenkov detector, are used to guide expectations for the full NuPRISM project cost.

A. Uncertainties in Neutrino Energy Determination

Prior to 2009, neutrino interaction models assumed that neutrinos, when encountering a nuclear target, interact with a single nucleon. The initial state of the nucleon was characterized by a binding energy and Fermi momentum, which were drawn from either a Fermi gas [5, 6] or a more specialized spectral function treatment [7]. In this paradigm, all the remaining dynamics of charge-current quasi-elastic (CCQE) interactions, in which the target neutron is converted into an outgoing proton, are encapsulated in a set of three vector and three axial-vector form factors. Most of these form factors are tightly constrained from external electron and pion scattering experiments (for a detailed discussion, see Ref. [8]). The largest remaining uncertainty is on the axial vector form factor, which is assumed to take a dipole form,

$$F_A(Q^2) = \frac{F_A(0)}{(1+\frac{Q^2}{M_A^2})^2}. \quad (1)$$

The parameter $F_A(0)$ is precisely known from nuclear beta decay, which leaves M_A as the remaining uncertain parameter. Modifying M_A simultaneously alters both the overall CCQE cross section and the shape of the Q^2 distribution.

In 2009, the first comparison of MiniBooNE CCQE-like data at neutrino energies around 1 GeV and NOMAD data at higher energies was released [9]. A reproduction of that comparison is shown in Figure II A. The MiniBooNE data are consistent with an M_A value of 1.35 GeV (an additional empirical parameter, κ is consistent with no modification at 1 σ), while the NOMAD data prefer an M_A of 1.03 GeV. This discrepancy is currently unexplained by neutrino-nucleus interaction models and is an outstanding experimental question that can be addressed by NuPRISM (see Section III L 2).

Later in 2009, the Marteau [10] formalism for the treatment of neutrino scattering on nucleon pairs in nuclei was resurrected by Martini *et al.* [11–13] to explain the higher event rate and muon kinematic distributions observed by MiniBooNE. If this explanation of the MiniBooNE event excess were correct, it would imply that neutrino energy reconstruction for all previous neutrino experiments on nuclei at the GeV scale could have significant biases for 20-30% of CCQE-like events. In the past few years, the models of Martini *et al.* and Nieves *et al.* [14] have begun to incorporate these effects, but such calculations are very difficult and the predictions of just these two models produce significantly different results when applied to T2K oscillation analyses [4].

There exists circumstantial experimental evidence for multinucleon interaction mechanisms in both neutrino and electron scattering, but nothing that allows us to conclusively solve the problem or even to down-select among the various calculations. In electron scattering, the reaction mechanism is different due to the absence of an axial-vector current component. In neutrino scattering experiments with broadband beams, the evidence is only circumstantial, since we must rely on the predictions of the models themselves to extract the neutrino energy for any given event. Other approaches, such as making precise measurements of the hadronic final state, are limited by a lack of theoretical understanding of the expected hadron kinematics for multinucleon events. Even the final state hadron spectra for CCQE events are modified by nuclear effects which are also not well understood.

Figure 2 illustrates the challenge associated with using near detector data to constrain the interaction model that predicts far detector event rates. The detectors measure the convolution of the neutrino spectrum with the interaction model. Since the near and far detector spectra are different due to neutrino oscillations, the measurement of this convolution in the near detector does not directly constrain the event rate in the far detector, and neutrino energies that represent a small fraction of the event rate in the near detector can significantly impact the measurement of oscillation parameters in the far detector.

In addition to multinucleon effects, other effects such as long range correlations and final state interactions within the target nucleus can also produce distortions to the neutrino energy spectrum that can be difficult to model. Figure 3 shows the ratio of the neutrino to antineutrino cross section for ν_μ according to several theoretical models. The MiniBooNE measurement is also shown. In order to perform precision oscillation measurements with uncertainties at the level of the few percent statistical errors expected for 7.8×10^{21} POT, it will be necessary to provide a data-driven constraint on these neutrino interaction model uncertainties.

B. Uncertainties on the T2K CPV Measurement Using ND280

The proposed T2K-II extension to T2K will accumulate 20×10^{21} protons on target (POT) by 2026. Potential beam line and analysis upgrades may further improve the sensitivity of the experiment to detect CP violation. For a favorable value of the CP phase, $\delta_{CP} = -\pi/2$, which is weakly favored by current neutrino oscillation data, T2K-II has the potential to achieve 3σ sensitivity, as shown in Fig. 4. With systematic errors included using the current preliminary update to the T2K systematic error model, the sensitivity barely crosses 3σ with an exposure of $20{\times}10^{21}$ POT. This significance relies on a favorable value of δ_{CP} and the assumption of improvements to the T2K experiment and analysis equivalent to 50% more statistics. T2K-II will not have 3σ sensitivity if either of these conditions are not true, or if the systematic uncertainties are larger than expected. Fig. 4 also shows that a reduction of the systematic errors to 2/3 of their current estimated values will improve the signficance such that the same sensitivity can be achieved with 75% of the statistics. The reduction of systematic uncertainties is required to achieve the best CP discovery sensitivity as soon as possible and also to ensure a robust search for CP violation in T2K-II.

The preliminary update of the T2K systematic error estimates is summarized in Table I, which shows the fractional error on the predicted number of events at Super-K for both horn polarities, ν mode and $\bar{\nu}$ mode, and final state lepton flavors, 1-Ring μ and 1-Ring e. CP violation is detected primarily through the observation of an asymmetry in the oscillation rate observed in the 1-Ring e ν mode and $\bar{\nu}$ mode data samples. The final column in Table I highlights the systematic errors that impact the CP violation measurement most strongly by showing the uncertainty on the ratio of predicted 1-Ring e events in ν mode and $\bar{\nu}$ mode.

The systematic errors with the largest impact on the CP violation detection are the uncertainty on the pion final state and secondary interactions at Super-K (3.7%), and the uncertainties on the electron (anti)neutrino cross section differences from the muon (anti)neutrino cross section (3.1%). The final state and secondary pion interaction uncertainties arise from uncertainties on the cascade model that is used to model the pion propagation through the target nucleus and the Super-K detector. This model has been tuned to pion-nucleus scattering data, however, the uncertainty remains significant since there are large model uncertainties in applying the pion-nucleus scattering data, particularly for the modeling of the final state interactions, where the pion is produced inside the nuclear medium.

The uncertainty on the electron (anti)neutrino cross sections enters the measurement since the rates of muon

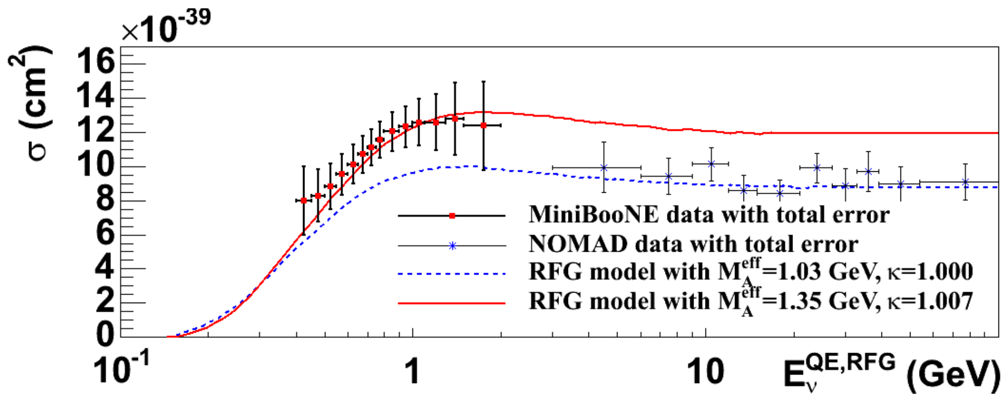

FIG. 1. The CCQE cross section measurements are shown for MiniBooNE and NOMAD. The data show significant differences between measurements made at low and high energies.

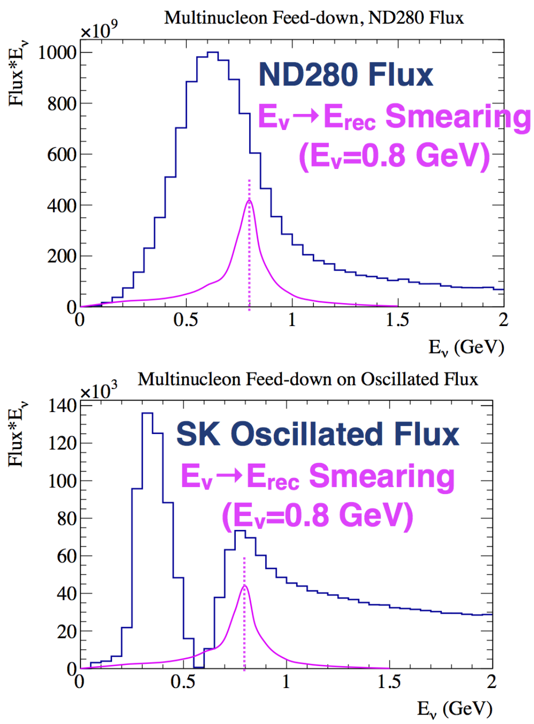

FIG. 2. A cartoon of the effect of energy reconstruction biases is shown for both the T2K near detector (top) and the far detector (bottom). At the far detector, these biases directly impact the measurement of the oscillation dip, but the biases are largely unconstrained at the near detector due to the large unoscillated sample of unbiased CCQE events.

(anti)neutrinos are measured in the near detector while electron (anti)neutrinos are detected in the far detector. Since conventional neutrino beams produce neutrinos from pion decays, there are no precision measurements of electron (anti)neutrino-nucleus scattering at $\mathcal{O}(1\text{ GeV})$ and experiments such as T2K rely on models of neutrino-nucleus scattering to account for the differences in the

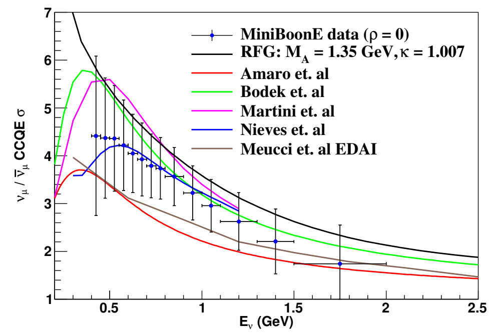

FIG. 3. The ratio of the CCQE cross section ration for muon neutrinos and anti-muon neutrinos is shown for various theoretical models and the MiniBooNE measurement. More precision is required for precision CP violation measurements. (plot courtesy of J. Grange, private communication)

electron (anti)neutrino and muon (anti)neutrino cross sections. Theoretical uncertainties on the differences in the interaction cross sections have been estimated by Day and McFarland [8]. They include the uncertainty arising from the phase space differences due to the lepton mass difference, the uncertainty on the size of second-class currents, and radiative corrections. For the T2K beam, the error on the interaction rates is estimated to be 3% with significant anti-correlations between the neutrino and antineutrino rates. It should be emphasized that this uncertainty is a theoretical estimate. Given the challenges in the theoretical modeling of neutrino-nucleus interactions, the electron (anti)neutrino cross sections should be confirmed directly with measurements, particularly for an experiment that hopes to report a discovery of CP violation.

The uncertainties on the modeling of the Super-K detector response (1.9%), uncertainties on flux and cross section model parameters directly constrained by the ND280 data (2.4%), and the uncertainty on the NC1γ

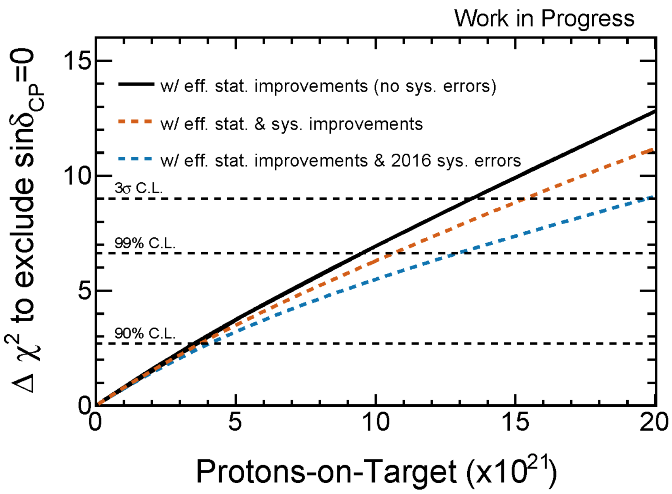

FIG. 4. The significance of T2K-II to disfavor a non-CP violating value of δ_{CP} for a true value of $\delta_{CP} = -\pi/2$ as a function of the accumulated POT assuming 50% neutrino mode data and 50% anti-neutrino mode data. The sensitivity with systematic uncertainties is evaluated using the current preliminary systematic error model (blue dashed), or a systematic error model with uncertainties arbitrarily reduced to 2/3 of their current value (red dashed). For all curves, it is assumed that experimental and analysis improvements for T2K-II will yield the equivalent of a 50% improvement in statistics over the current T2K experimental configuration and analysis techniques.

cross section (1.5%) also contribute significantly to the total systematic error.

C. Detector Overview

The NuPRISM detector uses the same water Cherenkov detection technology as Super-K with a cylindrical water volume that is taller than Super-K (50-100 m vs 41 m) but with a much smaller diameter (10-12 m vs 39 m). The key requirements are that the detector span the necessary off-axis range (1°-4°) and that the diameter is large enough to contain the maximum required muon momentum. The baseline design considers a detector location that is 1 km downstream of the neutrino interaction target with a maximum contained muon momentum of 1 GeV/c. This corresponds to a 50 m tall tank with a 6 m diameter inner detector (ID) and a 10 m diameter outer detector (OD). A larger, 8 m ID is also being considered at the expense of some OD volume at the downstream end of the tank. As the NuPRISM analysis studies mature, the exact detector dimensions will be refined to ensure sufficient muon momentum, ν_e statistics and purity, etc.

The instrumented portion of the tank is a subset of the full height of the water volume, currently assumed to be 10 m for the ID and 14 m for the OD. The novel feature of this detector is the ability to raise and lower the instrumented section of the tank in order to span the full off-axis range in 6 steps. The inner detector will be instrumented with either 8-inch, 5-inch, or 3-inch PMTs to ensure sufficient measurement granularity for the shorter light propagation distances relative to Super-K. Also under consideration is to replace the OD reflectors with large scintillator panels, such as those used in the T2K Side Muon Range Detector (SMRD), although this has not yet been integrated into the overall detector design. More details regarding the detector hardware can be found in Section IV

Finally, we a considering a NuPRISM phase 0, in which the instrumented portion of the detector is constructed and placed on the surface near ND280 prior to the excavation of the water volume. At the surface, the off-axis angle is 6° or larger, which provides even higher purity for measurements of ν_e, and measurements of neutron capture can be made to help calibrate the SKGd. This detector can also be used to demonstrate the detector performance relative to SK in an experimental setup that is easily accessible. This option is discussed in detail in Section VI.

III. PHYSICS CAPABILITIES

The physics goals of NuPRISM can be summarized in 5 main categories:

1. For the T2K CP violation measurement, NuPRISM can provide a data-driven constraint of $\sigma(\nu_e)/\sigma(\nu_\mu)$. The NuPRISM ν_μ flux can be matched to the NuPRISM ν_e flux to remove flux uncertainties, and NuPRISM's large size should allow for sufficient ν_e statistics to reach a 2-3% constraint.

2. By recreating the T2K oscillated ν_μ neutrino energy spectra at the NuPRISM near detector, the outgoing lepton kinematics for any set of disappearance parameters can be measured at NuPRISM and directly compared to the observed lepton kinematics at the far detector. This results in the cancelation of systematic uncertainties related to neutrino interaction modeling to first order. This improved precision on ν_μ may resolve the θ_{23} octant, which further enhances T2K's sensitivity to CP violation.

3. NuPRISM can directly measure the neutrino interaction final state from a range of mono-energetic beams. This allows for unique cross section measurements, such as the first ever energy-dependent neutral current (NC) and charged current (CC) cross section measurements that do not rely on neutrino generators to provide the incident neutrino energy. These measurements can constrain most oscillation analysis backgrounds with high precision. Measurements from mono-energetic beams,

TABLE I. Errors on the number of predicted events in the Super-K samples from individual systematic error sources in neutrino (ν mode) and antineutrino beam mode ($\bar{\nu}$ mode). Also shown is the error on the ratio 1Re events in ν mode/$\bar{\nu}$ mode. The uncertainties represent work-in-progress for T2K neutrino oscillation results in 2016.

	$\delta_{N_{SK}}/N_{SK}$ (%)				
	1-Ring μ		1-Ring e		
Error Type	ν mode	$\bar{\nu}$ mode	ν mode	$\bar{\nu}$ mode	$\nu/\bar{\nu}$
SK Detector	4.6	3.9	2.8	4.0	1.9
SK Final State & Secondary Interactions	1.8	2.4	2.6	2.7	3.7
ND280 Constrained Flux & Cross-section	2.6	3.0	3.0	3.5	2.4
$\sigma_{\nu_e}/\sigma_{\nu_\mu}$, $\sigma_{\bar{\nu}_e}/\sigma_{\bar{\nu}_\mu}$	0.0	0.0	2.6	1.5	3.1
NC 1γ Cross-section	0.0	0.0	1.4	2.7	1.5
NC Other Cross-section	0.7	0.7	0.2	0.3	0.2
Total Systematic Error	5.6	5.5	5.7	6.8	5.6
External Constraint on θ_{12}, θ_{13}, Δm^2_{21}	0.0	0.0	4.2	4.0	0.1

such as the energy transferred to the hadronic system, are also of great interest to the nuclear physics community.

4. The distance between the neutrino production target and NuPRISM is ideal for searching for sterile neutrino oscillations with mass splittings near 1 eV^2. Since the relative populations of the signal and background events vary differently as the off-axis angle changes, NuPRISM can provide unique constraints on many of the background-related hypotheses for the MiniBooNE low energy excess in a manner that is complementary to the Fermilab short-baseline program.

5. The SK-Gd upgrade will provide additional information that can be useful for a wide variety of T2K and SK analyses, however neutron production cross sections in neutrino interactions are poorly understood. NuPRISM can provide a precise calibration of neutron capture rates as a function of lepton kinematics and neutrino energy.

The following sections will describe the NuPRISM detector concept and the impact it can have on a variety of physics analyses at T2K and Super-Kamiokande. A detailed description of the simulation and analysis inputs used to calculate sensitivities, which are largely derived from standard T2K tools, is also provided.

A. Off-Axis Fluxes

The NuPRISM detector concept exploits the fact that as a neutrino detector is moved to larger off-axis angles relative to the beam direction, the peak energy of the neutrino energy spectrum is lowered and the size of the high-energy tail is reduced. This effect can be seen in Figure 5, which shows the neutrino energy spectra at several different off-axis angles in the T2K beam line. Since the off-axis angle for a single neutrino interaction can be determined from the reconstructed vertex position, this extra dimension of incident neutrino energy dependence can be used to constrain the interaction rates and final state particles in a largely model independent way.

A typical NuPRISM detector for the T2K beam line would span a continuous range of off-axis angles from 1° to 4°. For T2K, the best choice of technology is a water Cherenkov detector in order to use the same nuclear target as Super-K, and to best reproduce the Super-K detector efficiencies.

B. Monochromatic Beams

The detector can be logically divided into slices of off-axis angle based on the reconstructed vertex of each event. In each slice, the muon momentum and angle relative to the mean neutrino direction can be measured. By taking linear combinations of the measurements in each slice, it is possible to produce an effective muon momentum and angle distribution for a Gaussian-like beam at energies between 0.4 and 1.2 GeV. Qualitatively, any desired peak energy can be chosen by selecting the appropriate off-axis angle, and then the further on-axis measurements are used to subtract the high energy tail, while the further off-axis measurements are used to subtract the low energy tail. Figure 6 shows three such "pseudo-monochromatic" neutrino energy spectra constructed in this manner. These spectra are for selected 1-ring muon candidates and systematic errors from the flux model are applied using the T2K flux systematic error model. The statistical errors for an exposure of 4.5×10^{20} protons on target are also shown. In all cases the high energy and low energy tails are mostly canceled over the full energy range and the monochromatic nature of the spectrum is stable under the flux systematic and statistical variations.

Figure 7 shows the reconstructed energy distributions for 1-ring muon candidates observed with the pseudo-

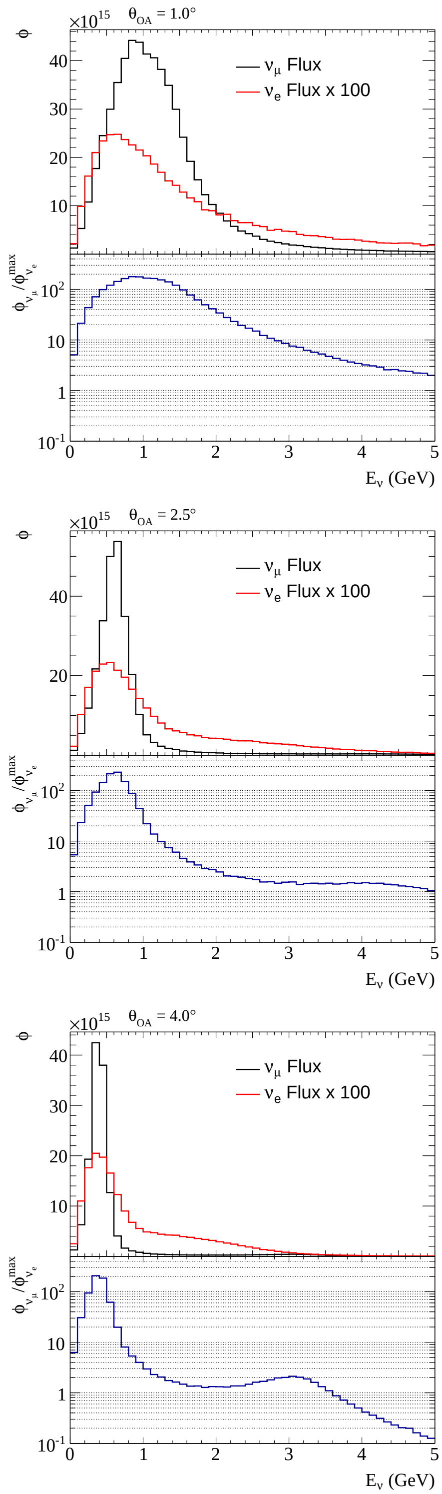

FIG. 5. The neutrino energy spectra for ν_μ and ν_e fluxes in the T2K beam operating in neutrino mode are shown for off-axis angles of 1°, 2.5°, and 4°. The ν_μ flux normalized by the maximum ν_e flux is shown at the bottom of each plot, demonstrating that feed-down from high energy NC backgrounds to ν_e candidates can be reduced by going further off-axis.

monochromatic beams shown in Figure 6. The candidate events are divided into quasi-elastic scatters and non-quasi-elastic scatters, which include contributions from processes related to nuclear effects such as multinucleon interactions or pion absorption in final state interactions. With these pseudo-monochromatic beams, one sees a strong separation between the quasi-elastic scatters and the non-quasi-elastic scatters with significant energy reconstruction bias, especially in the 0.8 to 1.2 GeV neutrino energy range. These measurements can be used to directly predict the effect of non-quasi-elastic scatters in oscillation measurements and can also provide a unique constraint on nuclear models of these processes.

Since the pseudo-monochromatic beams have a well definined energy with a 1σ width typically less than 0.15 GeV and a well defined direction, it is possible to use the known neutrino energy and direction to construct observables that are typically used in electron scattering experiments where the beam's four momentum is known. These include the energy transfer to the target, ω, the square of the three momentum transfer to the target, q^2, the square of the four momentum transfer, $Q^2 = q^2 - \omega^2$, and the Bjorken x, $x_B = Q^2/(2m\omega)$. Unlike the typical treatment in neutrino scattering data, where the energy and momentum transfer are calculated assuming quasielastic kinematics with a single bound nucleon target, the energy and momentum transfer can be calculated from the pseudo-monochromatic beam constraint and the observed final state muon kinematics. Hence the cross section as a function of these observables can be measured for non-quasielastic as well as quasielastic interactions. Figure 8 shows the distribution of reconstructed single μ ring events with an $E_\nu = 1$ GeV pseudo-monochromatic beam in the energy and momentum transfer variables, broken down by true quasielastic and non-quasielatic events. Figure 9 shows the energy transfer for a single slice of $q^2 = 0.7 - 0.9$ $(\mathrm{GeV}/c)^2$ with flux and statistical error bars included. By making measurements in these variables, NuPRISM measures neutrino-nucleus cross sections as a function of the kinematics of probe of the nucleus, independent of the interaction type. This is a unique capability among neutrino scattering experiments.

The NuPRISM technique can be expanded beyond these pseudo-monochromatic beams. This linear combination method can be used to reproduce a wide variety of flux shapes between 0.4 and 1.0 GeV. In particular, as described later in this section, it is possible to reproduce all possible oscillated Super-K spectra with a linear combination of NuPRISM measurements, which significantly reduces many of the uncertainties associated with neutrino/nucleus interaction modeling.

C. Simulation Inputs

To perform NuPRISM sensitivity analyses, the official T2K flux production and associated flux uncertainties

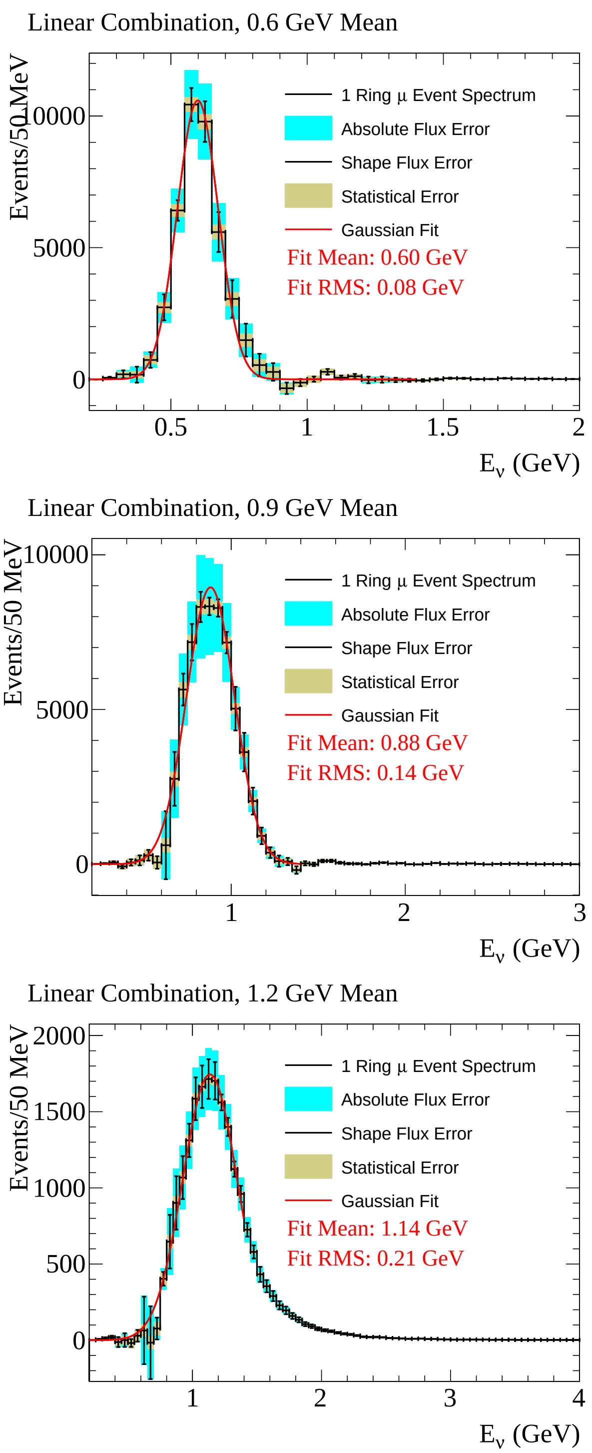

FIG. 6. Three "pseudo-monochromatic" spectra centered at 0.6 (top), 0.9 (middle) and 1.2 (bottom) GeV. The aqua error bars show the 1 σ uncertainty for flux systematic variations, while the black error bars show the flux systematic variation after the overall normalization uncertainty is removed. The tan error bars show the statistical uncertainty for samples corresponding to 4.5×10^{20} protons on target.

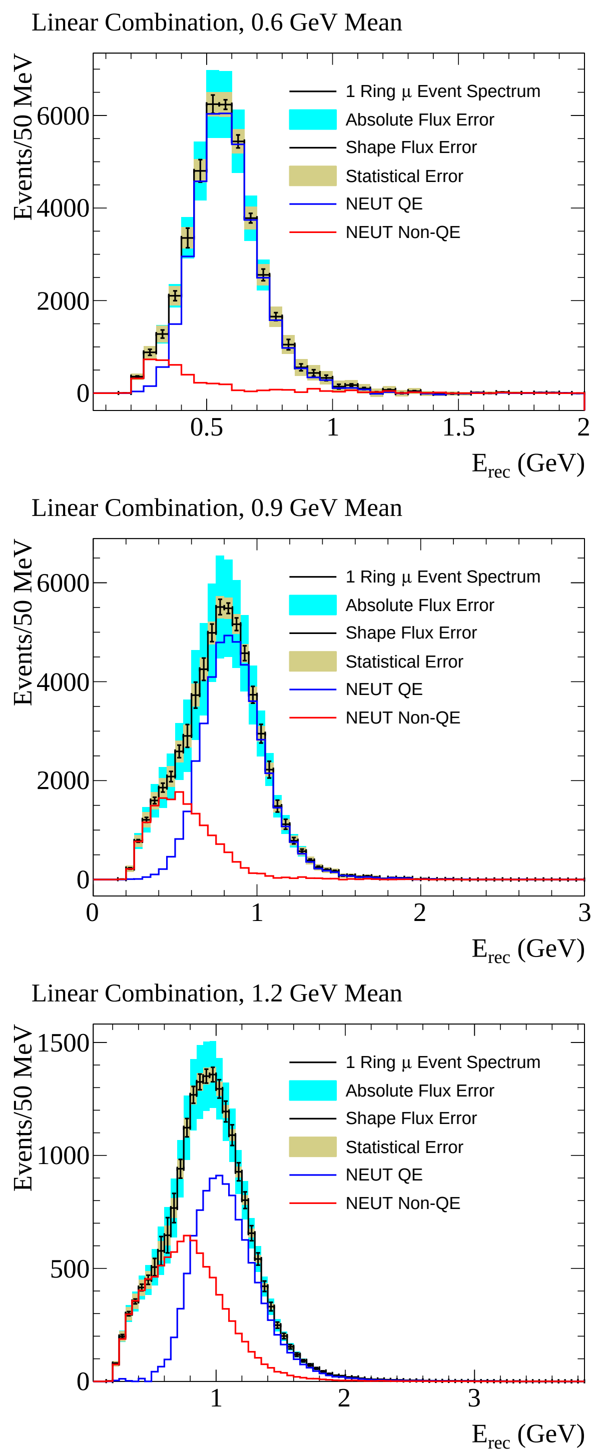

FIG. 7. The reconstructed energy distributions for 1-ring muon candidate events produced using "pseudo-monochromatic" spectra centered at 0.6 (top), 0.9 (middle) and 1.2 (bottom) GeV. The aqua error bars show the 1 σ uncertainty for flux systematic variations, while the black error bars show the flux systematic variation after the overall normalization uncertainty is removed. The tan error bars show the statistical uncertainty for samples corresponding to 4.5×10^{20} protons on target. The red and blue histograms show the contributions from non-quasi-elastic and quasi-elastic scatters respectively.

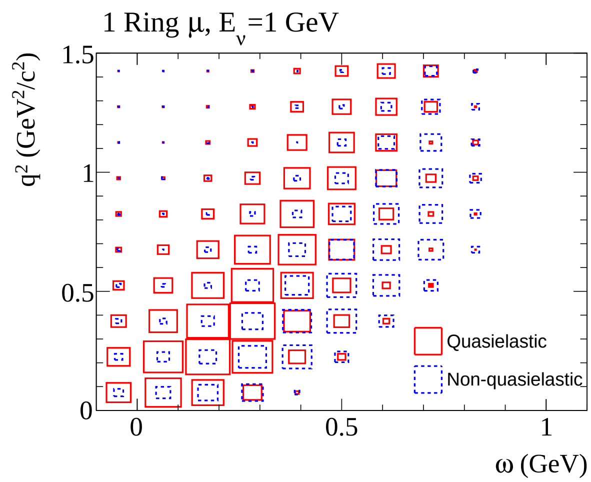

FIG. 8. For an $E_\nu = 1$ GeV pseudo-monochromatic beam, the distribution of observed single muon ring events in reconstructed energy transfer and reconstructed square of the three momentum transfer. The true quasielastic events are shown in red and the true non-quasielastic events are shown in blue.

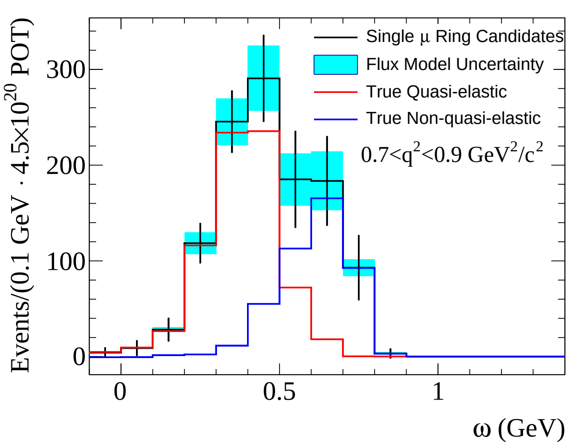

FIG. 9. For an $E_\nu = 1$ GeV pseudo-monochromatic beam, the distribution of observed single muon ring events in reconstructed energy transfer when the reconstructed q^2 is between 0.7 and 0.9 GeV$^2/c^2$. The true quasielastic events are shown in red and the true non-quasielastic events are shown in blue. The flux and statistical uncertainties (for a $4.5{\times}10^{20}$ proton on target exposure) are shown.

have been extended to cover a continuous range of off-axis angles, and the standard T2K package used to generate vertices in ND280 has also been modified to handle flux vectors with varying energy spectra across the detector. Two different methods are used to simulate interactions in the NuPRISM detector. In the original method for studying selected event samples in NuPRISM, selection efficiencies and reconstruction resolutions for vertex, direction, and visible energy were tabulated using the results of fiTQun (the new Super-K reconstruction algorithm) run on Super-K events. The efficiency for electrons (muons) was defined as events passing the following cuts: OD veto, 1-ring, e-like (μ-like), 0 (1) decay electrons, and the T2K fiTQun π^0 rejection (no π^0 cut). The efficiency tabulation was performed in bins of the true neutrino energy, the visible energy and distance along the track direction to the wall of the most energetic ring, and separate tables were produced for charged current events with various pion final states (CC0π, CC1$\pi^{\pm}0\pi^0$, CC0$\pi^{\pm}1\pi^0$, CCN$\pi^{\pm}0\pi^0$, and CCother) for both ν_e and ν_μ events, as well as a set of neutral current final states, also characterized by pion content (NC0π, NC1$\pi^{\pm}0\pi^0$, NC0$\pi^{\pm}1\pi^0$, NCN$\pi^{\pm}0\pi^0$, and NCother). To determine the smearing of true quantities due to event reconstruction, vertex, direction, and visible energy resolution functions were also produced for the 1-ring e-like and μ-like samples in bins of visible energy and distance along the track direction to the wall of the most energetic ring.

Recently, a dedicated NuPRISM detector simulation has been developed. It uses the GEANT4 based WCSim software to simulate the detector response and fiTQun-based event reconstruction. Fig. 10 shows example event displays from simulated neutrino interations. Where indicated in this document, results based on the NuPRISM simulation will be presented. The NuPRISM simulation was carried out for a 6 m diameter, 10 m height inner detector with 8 in diameter PMTs providing 40% photochathode coverage.

The neutrinos in NuPRISM are simulated with the T2K flux simulation tool called JNUBEAM [15]. The version of JNUBEAM used is consistent with what is currently used by T2K and it includes the modeling of hadronic interactions based on data from the NA61/SHINE experiment [16, 20]. We define the off-axis angle for a particular neutrino as the angle between the beam axis and the vector from the average neutrino production point along the beam axis to the point at which the neutrino crosses the flux plane, as illustrated in Fig. 11. The off-axis angle is defined in terms of the average neutrino production point so that an off-axis angle observable can be constructed based on the location of the interaction vertex in NuPRISM. The off-axis angle and energy dependence for each neutrino flavor is shown in Fig. 12. The neutrino flux files are produced for both neutrino mode (focussing positively charged hadrons) and antineutrino mode (focussing negatively charged hadrons), although only the neutrino mode flux is used for the analysis presented in this note.

The positions of the neutrino interaction vertices in the NuPRISM water volume are shown in Fig. 13. The rate of simulated interactions has been cross checked against the observed INGRID rates and found to be consistent.

D. Event Pileup

The baseline design of NuPRISM is an outer detector (OD) volume with radius of 5 m and height of 14 m, and

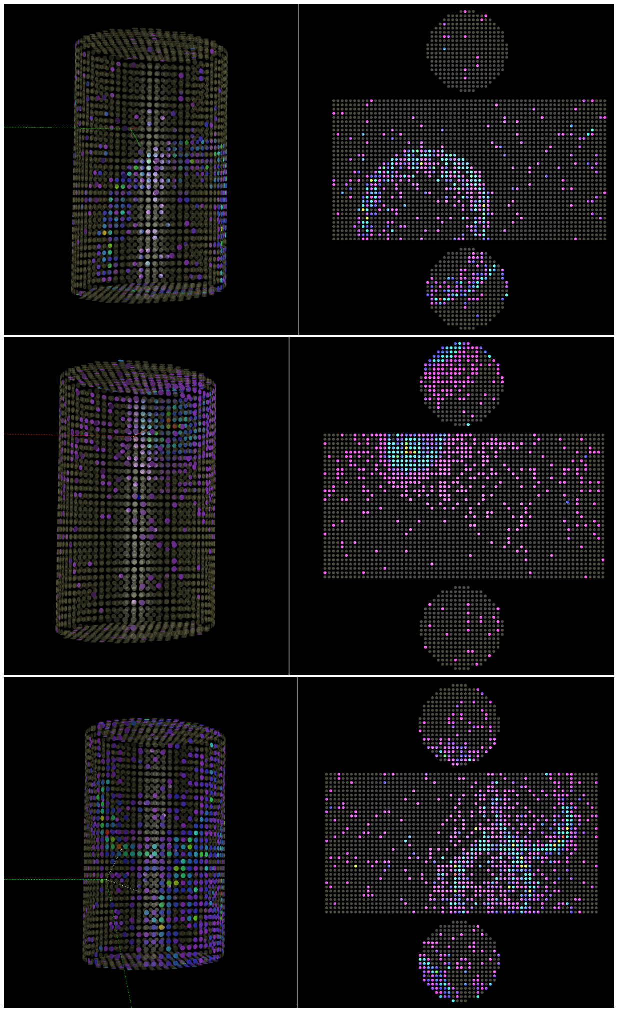

FIG. 10. Example event displays from the WCSim based simulation of NuPRISM for ν_μ-CCQE (top), ν_e-CCQE (middle) and NCπ^0 (bottom) interactions.

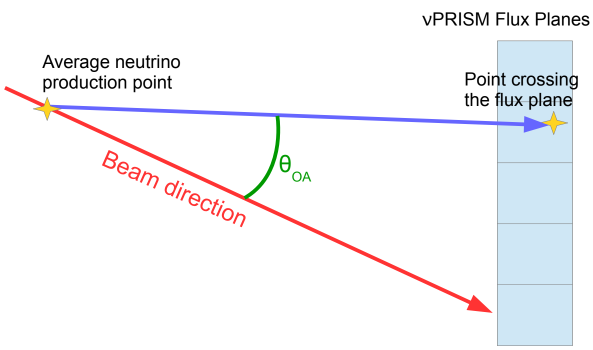

FIG. 11. The definition of the off-axis angle for individual neutrinos.

an inner detector (ID) volume with a radius of 3 m and height of 10 m, located 1 km from the T2K target. We also consider a design where the ID volume has a radius of 4 m and height of 12 m, leaving 1 m of OD surrounding the ID.

We have carried out a simulation of events in the NuPRISM ID and OD volumes, as well as the surrounding earth and water column to study the event pile-up in NuPRISM. Interactions and particle propagation in the earth+NuPRISM geometry shown in Fig. 14 are simulated. The flux at the upstream end of the volume is simulated using the JNUBEAM package with horn currents set to 320 kA (neutrino beam) or -320 kA (antineutrino beam). Interactions in the earth and detector volumes are generated using the NEUT neutrino interaction generator. The earth volume is filled with SiO_2 with a density of 2.15 g/cm^3. The water volume has three detector sub-volumes: the ID detector, the OD detector and an intermediate volume corresponding the the 4 m radius ID. The vertical position of the detector volumes in the water column can be adjusted to study the event pile-up at different off-axis angles. A GEANT4 simulation of the particles from the neutrino vectors is carried out and all particles with visible energy greater than 10 MeV are recorded if they originate in any of the detector volumes or cross any of the detector volume boundaries. Entering neutrons are considered separately from charged particles and photons.

Events can be categorized in two ways: by where the original interaction takes place and by the detector volumes in which particles produce Cherenkov radiation. In the first case, events are categorized as originating in the ID, OD or the earth and water surrounding the OD. In the second case, events are categorized as producing light exclusively in the OD, exclusively in the ID, or in both the ID and OD. Events that orginate in the ID and are contained in the ID are the signal events.

The J-PARC beam consists of 8 microbunches per spill. The microbunches are ∼15 ns long and separated by ∼600 ns. For 750 kW beam operation with a 1 Hz spill frequency, there are 2×10^{13} protons in each microbunch. For the pile-up studies presented here, we consider 2×10^{13} protons per bunch and 1.6×10^{14} protons per spill. Event rates are considered with the NuPRISM detector placed at off-axis positions of 1.0-1.6°, 2.0-2.6° and 3.0-3.6°. Event rates are also produced at 0.0-0.6° off-axis so that comparisons can be made to the observed event rates in the T2K on-axis INGRID detectors.

1. *Visible particle rates and pile-up*

Tables II and III show the simulated event rates with visible particles for the 3 m and 4 m radius IDs respectively. For the $1.0-1.6°$ off-axis angle position, the total rate of ID+OD visible events in a spill (8 bunches) is 8.10. If a bunch contains an event, the probability that the next bunch contains at least one visible event is 63.7%.

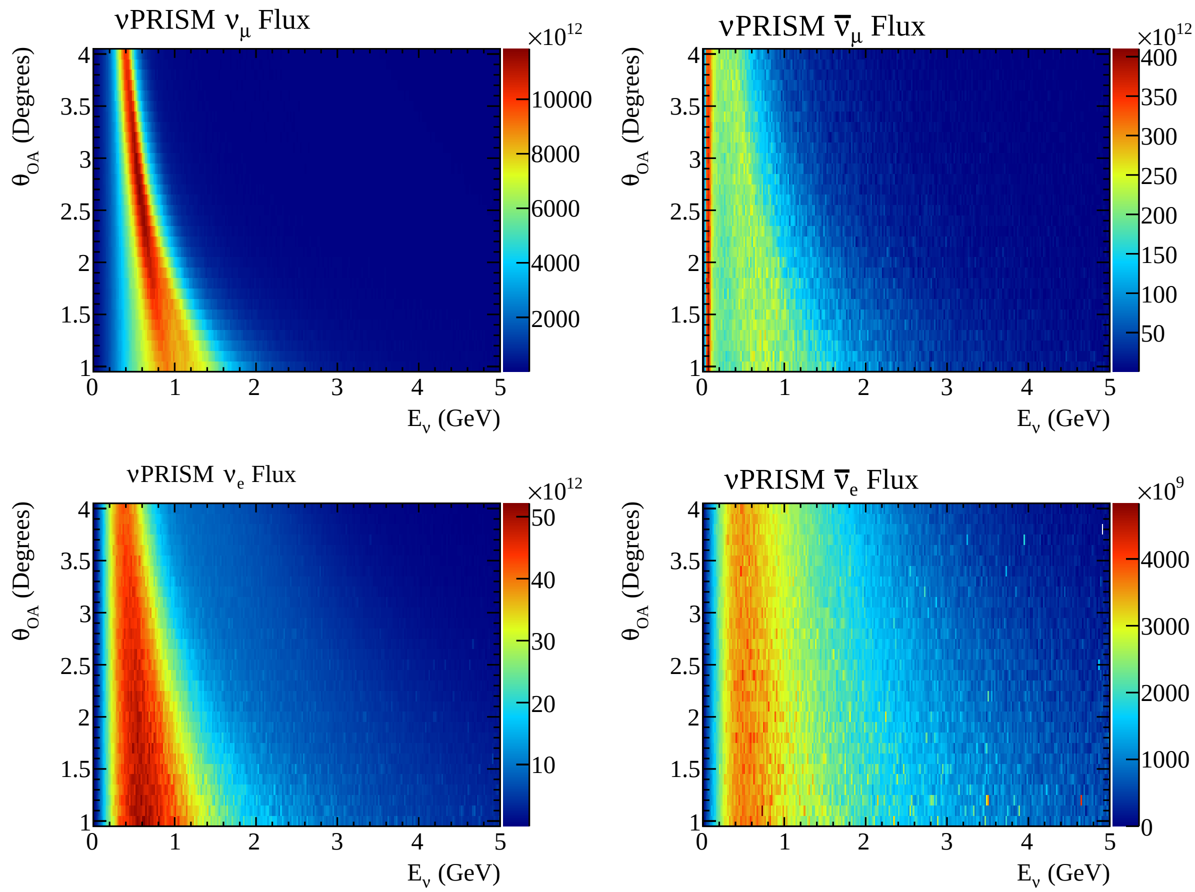

FIG. 12. The neutrino flux (arbitrary normalization) as a function of off-axis angle and energy for each neutrino flavor with the horn in neutrino-mode operation.

This suggests that NuPRISM should employ deadtimeless electronics that can record events in neighboring bunches and that the after-pulsing of PMTs should be carefully considered.

For the 3 m ID case in the $1.0-1.6°$ position, there are 0.917 events with OD light per bunch. If a simple veto on any OD light in the same bunch is applied, 60.0% of fully contained ID events are vetoed due to the accidental coincidence rate in the OD. This simple OD veto rate drops to 25.8% and 10.7% for the $2.0-2.6°$ and $3.0-3.6°$ positions respectively. For the 4 m ID case, the simple OD veto rates are 54.2%, 22.2% and 9.5% for the $1.0-1.6°$, $2.0-2.6°$ and $3.0-3.6°$ positions respectively. A more intelligent OD veto may be applied if entering charged particles are tracked by scintillator panels at the OD and ID detector boundaries. These events may be kept in the analysis and the reconstruction can be seeded with the entering particle position and trajectory as measured by the scintillator panels. In that case, the OD veto rates can be as low as 30.7% and 28.6% for the $1.0-1.6°$ position with the 3 m and 4 m radius IDs respectively.

The importance of the OD veto depends on the type of reconstructed candidate event. For reconstructed muon candidates, it is expected that entering backgrounds can be controlled by fiducialization, and a tight OD veto may not be required. For reconstructed electron candidates, entering backgrounds may need to be controlled with an OD veto. However, the most pure electron candidate samples will be collected in the most off-axis positions, where the OD pile-up is the smallest. Hence it is expected that pile-up in the OD will not drastically reduce the efficiency to select the event samples of most interest.

When the OD veto is applied, there may also be pile-up of fully contained ID events. There are on average 0.095, 0.035 and 0.016 fully contained ID events per bunch in the 3 m radius ID for the $1.0-1.6°$, $2.0-2.6°$ and $3.0-3.6°$ off-axis positions respectively. The percentage of fully contained ID events with 2 or more interactions is 4.6%, 1.7% and 0.8% for the 3 off-axis positions. For the 4 m radius ID, these percentages increase to 10.9%, 4.1% and 1.8%. It is expected that this level of pile-up can be handled by the reconstruction, either by vetoing on the presence of multiple vertices, or by reconstructing multiple vertices.

The probability for a selected FC ID event to be the only ID event in a spill is 22.4%. Since the muon de-

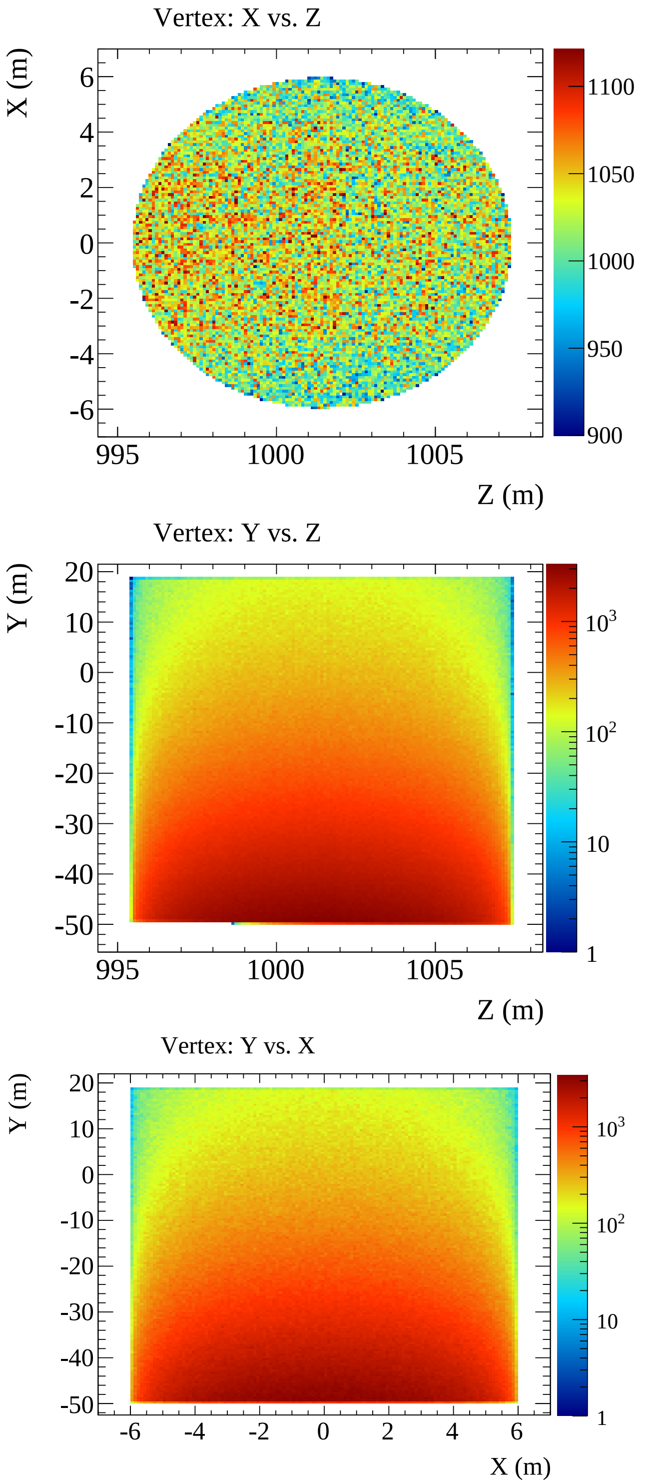

FIG. 13. The distribution of simulated vertices shown in projections to the x-z (top), y-z (middle) and x-y (bottom) planes. Here x is defined as the horizontal axis perpendicular to the beam, z is the horizontal axis in the beam direction and y is the vertical axis.

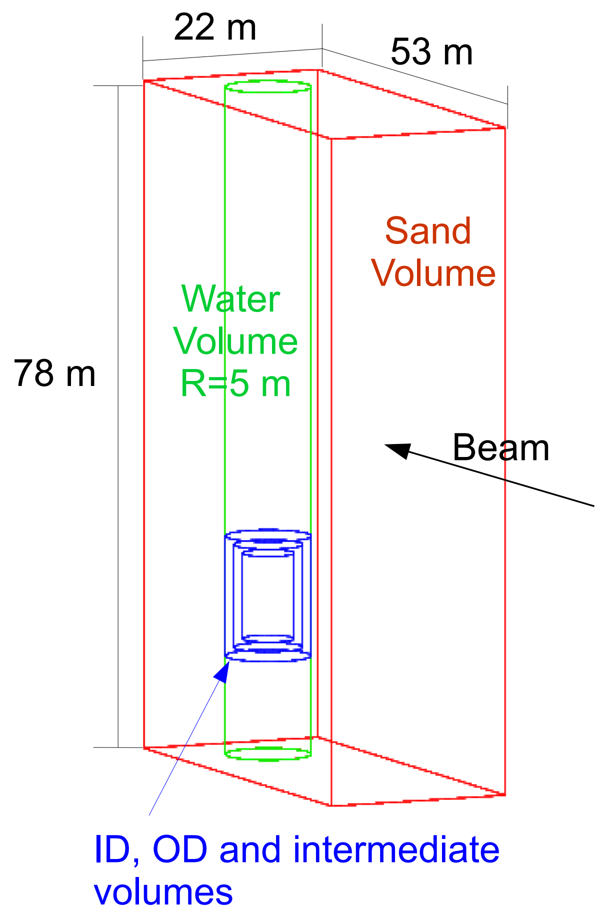

FIG. 14. The GEANT4 geometry used in the pile-up simulation.

cay time (2.2 μs) is comparable to the bunch spacing (600 ns), electrons from muon decays cannot be matched to their primary interaction using only the decay electron production time. For interactions inside the ID, a spatial likelihood matching the decay electron to the primary vertex may be constructed based on the reconstructed decay electron vertex position and the reconstructed primary vertex or reconstructed stopping point of the candidate muons or charged pions in the event. For decay electrons originating from muons produced outside of the ID, a similar spatial likelihood may be constructed using OD light, ID light, and hits from scintillator panels (if they are installed between the OD and ID) from the entering particle. Since the muon mean lifetime is shorter than the spill length (5 μs), there will also be statistical power to match decay electrons to their primary vertex based on the time separation of the decay electron vertex and primary vertex. On the other hand, the muon lifetime may provide a cross-check for the spatial matching of primary and decay electron vertices since significant mismatching would tend to smear the time separation distribution beyond the muon lifetime.

The event rates for an antineutrino beam are simulated by changing the horns' operating currents to -320 kA. Due to the smaller antineutrino cross section, the pile-up rates for antineutrinos are smaller than the comparable neutrino rates for every detector configuration.

2. *Entering neutron background*

Neutrons entering NuPRISM may interact to produce visible particles. Visible particles from neutron interactions have been included in the rates calculated in the previous section. If NuPRISM is doped with Gd to detect neutrons produced in neutrino interactions in the ID, entering beam induced neutrons will be a source of background. The number of neutrons entering the OD, 4 m radius ID and 3 m radius ID have been simulated.

Since the neutron capture time on Gd is ~ 30 μs and the spill length is ~ 5 μs, the entering neutron rates for a full spill (1.6×10^{14} protons on target) are shown in Table IV. In the $1.0 - 1.6°$ position, 9.120 neutrons enter the OD, but only 1.844 enter the 4 m radius ID. This reduction is greater than what is expected based on the relative surface areas of the OD and ID, and is due to the fact that there are no free protons in the SiO_2 earth simulation to moderate low energy neutrons. However, the inclusion of 0.5% by mass of H in the earth does not significantly change the rate of neutrons entering the ID. Since the rate of neutrons entering the ID for the most on-axis position is ~1-2 neutrons per spill, the reconstruction of neutron capture vertices with sufficient spatial resolution to separate signal neutrons from entering background neutrons is an important design consideration if NuPRISM will include Gd doping.

3. *Cross-check with INGRID*

We can cross-check the estimated NuPRISM event rates by extrapolating from the event rates observed by INGRID [21]. We assume that the rate of interactions inside the detector will scale with the detector mass, and the rate of entering events from the earth will scale with the cross-sectional area of the detector. The rates should also scale with $1/d^2$, were d is the distance from the average neutrino production point to the detector, about 240 m for INGRID and 960 m for NuPRISM.

INGRID observes 1.74 neutrino events per 1×10^{14} protons on target in 14 INGRID modules with a total mass of 5.7×10^4 kg. For an OD+ID mass of 1.1×10^6 kg, we extrapolate the INGRID rate, assuming 60% detection efficiency in INGRID, to obtain 0.69 interactions in the OD+ID for 2.0×10^{13} protons on target. The simulated rates of visible OD+ID interactions in NuPRISM are 2.33 and 0.67 for the $0.0 - 0.6°$ and $1.0 - 1.6°$ positions respectively. Since INGRID covers an angular range of about $\pm 1°$, it is reasonable that the extrapolated value from INGRID falls between the simulated NuPRISM values at these two positions.

INGRID also observes a event rate from earth interactions of 4.53 events per 1×10^{14} POT in 14 modules with a cross-sectional area of 21.5 m^2. These earth interaction candidates are INGRID events failing the upstream veto and fiducial volume cuts. The selection of entering earth-interaction events is $> 99\%$ efficient and 85.6% pure. Scaling to the OD cross-sectional area and distance while correcting for the efficiency and purity gives a rate of 0.32 events entering the OD per bunch. The rates from the NuPRISM simulation are 1.10 and 0.34 for the $0.0 - 0.6°$ and $1.0 - 1.6°$ degree positions respectively. Once again, the extrapolated INGRID rate is close to the range observed in the NuPRISM simulation.

In summary, the event pile-up rates for NuPRISM appear manageable. Even for the most on-axis position and high power beam, most bunches with interactions will only have a single interaction with visible light in the ID. The OD veto rate from pile-up can be as large as 60%, hence detailed studies of the OD design and performance will be carried out. The OD veto rate may be reduced and better understood with the inclusion of scintillator panels at the outer edge of the OD or at the OD/ID boundary. The electronics for NuPRISM should be deadtime-less to handle multiple events per spill. The rate of entering neutrons per spill is ~1-2 for the most on-axis position, so the reconstruction of neutron capture on Gd vertices will be considered in the optimization of the ID photo-detector configuration.

E. Event Selection for Sensitivity Studies

We select samples of single ring muon and electron candidates for the long and short baseline sensitivity studies described in the following sections. As described in Section III C, the efficiencies for single ring electron or muon selections are applied using tables calculated from the SK MC. The efficiency tables are calculated with the following requirements for muon and electron candidates:

- Muon candidate requirements: fully contained, a single muon-like ring, 1 or fewer decay electrons
- Electron candidate requirements: fully contained, a single electron-like ring, no decay electrons, passes the fiTQun π^0 cut

Additional cuts are applied on the smeared NuPRISM MC. For the muon candidates the cuts are similar to the SK selection for the T2K disappearance analysis:

- Muon candidate cuts: $dWall > 100$ cm, $toWall > 200$ cm, $E_{vis} > 30$ MeV, $p_\mu > 200$ MeV/c,

where $dWall$ is the distance from the event vertex to the nearest wall, and $toWall$ is the distance from the vertex to the wall along the direction of the particle.

TABLE II. The event rates per 2×10^{13} protons on target for NuPRISM with horn currents at 320 kA and ID radius of 3 m.

	Interaction Outside OD			Interaction Inside OD			Interaction Inside ID		
	Producing light in:								
Off-axis Angle (°)	OD only	ID only	ID & OD	OD only	ID only	ID & OD	OD only	ID only	ID & OD
0.0-0.6	0.877	0.001	0.226	1.464	0.005	0.241	0.007	0.341	0.271
1.0-1.6	0.273	0.000	0.068	0.428	0.001	0.071	0.002	0.094	0.075
2.0-2.6	0.084	0.000	0.021	0.149	0.000	0.021	0.000	0.035	0.024
3.0-3.6	0.034	0.000	0.007	0.062	0.000	0.001	0.000	0.016	0.009

TABLE III. The event rates per 2×10^{13} protons on target for NuPRISM with horn currents at 320 kA and ID radius of 4 m.

	Interaction Outside OD			Interaction Inside OD			Interaction Inside ID		
	Producing light in:								
Off-axis Angle (°)	OD only	ID only	ID & OD	OD only	ID only	ID & OD	OD only	ID only	ID & OD
0.0-0.6	0.612	0.004	0.488	0.763	0.007	0.265	0.008	0.807	0.479
1.0-1.6	0.193	0.001	0.147	0.227	0.002	0.079	0.002	0.227	0.134
2.0-2.6	0.061	0.000	0.044	0.077	0.001	0.026	0.001	0.084	0.042
3.0-3.6	0.025	0.000	0.016	0.033	0.000	0.011	0.000	0.036	0.015

For the single ring electron candidates, the cuts on $toWall$ and E_{vis} were reoptimized since the separation between electrons and muons or electrons and π^0s degrades closer to the wall. The cut on $dWall$ is set to 200 cm to avoid entering backgrounds. The cuts are:

- Electron candidate cuts: $dWall > 200$ cm, $toWall > 320$ cm, $E_{vis} > 200$ MeV.

The tight fiducial cuts for the electrons candidates are needed to produce a relatively pure sample, but there is a significant impact to the electron candidate statistics. A simulation with finer PMT granularity may allow for the $toWall$ cut to be relaxed, increasing the statistics without degrading the purity.

F. T2K ν_μ Disappearance Sensitivities

The most straightforward application of the NuPRISM concept to T2K is in the ν_μ disappearance measurement. The main goal of this ν_μ disappearance analysis is to demonstrate that NuPRISM measurements will remove most of the neutrino cross section systematic uncertainties from measurements of the oscillation parameters. This is achieved by directly measuring the muon momentum vs angle distribution that will be seen at Super-K for any choice of θ_{23} and Δm^2_{32}.

To clearly compare the NuPRISM ν_μ analysis with the standard T2K approach, the full T2K analysis is reproduced using NuPRISM in place of ND280. This is done by generating fake data samples produced from throws of the flux and cross section systematic parameters and fitting these samples using the standard oscillation analysis framework.

In the T2K analysis, for each flux, cross section and statistical throw, three fake data samples using different cross section models were produced at both ND280 and Super-K: 1) default NEUT with pionless delta decay, 2) NEUT with the Nieves multinucleon model replacing pionless delta decays, and 3) NEUT with an ad-hoc multinucleon model that uses the final state kinematics of the Nieves model and the cross section from Martini *et al.* For each throw, all three fake data samples were fit using model 1) to derive estimates of the oscillation parameters. The differences between the fitted values of $\sin^2\theta_{23}$ for the NEUT nominal and NEUT+Nieves or NEUT+Martini fake data fits are shown in Figure 15. The systematic uncertainty associated with assuming the default NEUT model rather than the model of Martini or Nieves is given by the quadrature sum of the RMS and mean (i.e. bias) of these distributions. For the ND280 analysis, there is a 3.6% uncertainty when comparing with the Nieves model, and a 4.3% uncertainty in the measured value of $\sin^2\theta_{23}$ when comparing with the Martini model. These uncertainties would be among the largest for the current T2K ν_μ disappearance analysis, and yet they are based solely on model comparisons with no data-driven constraint.

As was discussed in Section II A the limitation of using ND280 data to predict observed particle distributions at Super-K is that the neutrino flux at these two detectors is different due to oscillations. Therefore, any extrapolation has significant and difficult to characterize cross section model dependent uncertainties. In the NuPRISM based analysis, this limitation is resolved by deriving linear combinations of the fluxes at different off-axis angles to produce a flux that closely matches the predicted oscillated flux at Super-K. The observed particle distributions measured by NuPRISM are then combined with the same linear weights to predict the particle distribution at Super-K. In this way, the analysis relies on the flux model to determine the weights that reproduce the oscillated flux while minimizing cross section model de-

TABLE IV. The entering neutron rates per 1.6×10^{14} protons on target for NuPRISM with horn currents at 320 kA.

Off-axis Angle (°)	Entering OD	Entering ID (r=4 m)	Entering ID (r=3 m)
1.0-1.6	9.120	1.844	1.073
2.0-2.6	2.954	0.598	0.354
3.0-3.6	1.189	0.232	0.132

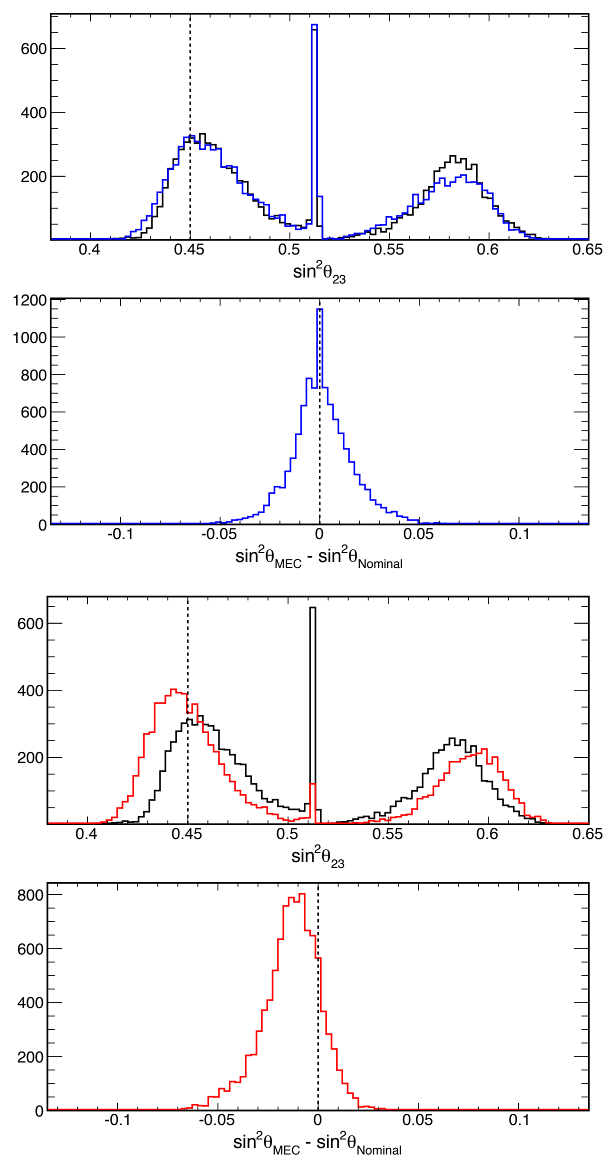

FIG. 15. The results of fitting fake data with and without multinucleon effects are shown. The measured differences in $\sin^2\theta_{23}$ when comparing the Nieves model to default neut (blue) and the Martini model to default neut (red) give RMS values of 3.6% and 3.2%, respectively, and biases of 0.3% and -2.9%, respectively.

pendence in the extrapolation.

The first stage of the NuPRISM ν_μ analysis is to separate the 1-4 degree off-axis range of the detector into 30 0.1 degree or 60 0.05 degree bins in off-axis angle. The neutrino energy spectrum in each off-axis bin is predicted by the T2K neutrino flux simulation. For each hypothesis of oscillation parameter values that will be tested in the final oscillation fit, the oscillated Super-K energy spectrum is also predicted by the T2K neutrino flux simulation. A linear combination of the 30 (60) off-axis fluxes is then taken to reproduce each of the Super-K oscillated spectra,

$$\Phi^{SK}\left(E_\nu;\theta_{23},\Delta m^2_{32}\right)E_\nu = \sum_{i=1}^{30} c_i\left(\theta_{23},\Delta m^2_{32}\right)E_\nu\Phi_i^{\nu P}(E_\nu), \tag{2}$$

where $c_i\left(\theta_{23},\Delta m^2_{32}\right)$ is the weight of each off-axis bin, i. The extra factors of E_ν are inserted to approximate the effect of cross section weighting. The $c_i\left(\theta_{23},\Delta m^2_{32}\right)$ are determined by a fitting routine that seeks agreement between the Super-K flux and the linear combination over a specified range of energy. An example linear combination of NuPRISM off-axis fluxes that reproduces the SK flux is shown in Figure 16. These fits can successfully reproduce Super-K oscillated spectra, except at neutrino energies below $\sim$ 400 MeV. The maximum off-axis angle is 4°, which peaks at 380 MeV, so at lower energies it is difficult to reproduce an arbitrary flux shape. This could be improved by extending the detector further off-axis.

The determination of the $c_i\left(\theta_{23},\Delta m^2_{32}\right)$ weights to reproduce the oscillated flux is subject to some optimization. Figure 17 shows two sets of weights for a particular oscillation hypothesis. In the first case a smoothness constrain was applied to the weights so that they vary smoothly between neighboring off-axis angle bins. In the second case the weights are allowed to vary more freely relative to their neighbors. Figure 18 shows the comparisons of the NuPRISM flux linear combinations with the Super-K oscillated flux for a few oscillation hypotheses in the smoothed and free weight scenarios. The oscillated flux in the maximum oscillation region is nearly perfectly reproduced when the weights are allowed to vary more freely. When they are constrained to vary smoothly, the agreement is less perfect, although still significantly better than the agreement between ND280 and Super-K fluxes. An analysis using the free weights is less dependent on the cross section model assumptions in the extrapolation to Super-K since the Super-K flux is more closely matched. On the other hand, the analysis with the smoothed weights is less sensitive to uncertainties on the flux model and NuPRISM detector model that have an off-axis angle dependence since neighboring bins have similar weight values. The statistical errors are also smaller for the smoothed weight case since the sum in quadrature of the weights in a given neutrino energy bin is smaller when there are less fluctuations in weight values. In the analysis presented here, the smoothed weights are used, although the optimization of the level of smoothness is an area where the analysis will be improved in the future.

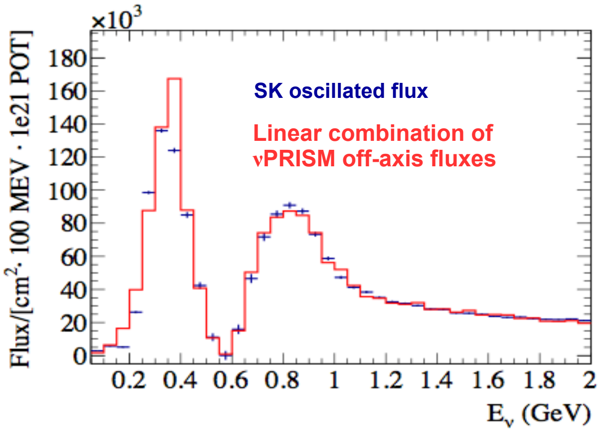

FIG. 16. A sample fit of the flux in 30 NuPRISM fluxes to an oscillated Super-K flux is shown. Good agreement can be achieved, except at low energies due to the 4° maximum off-axis angle seen by NuPRISM.

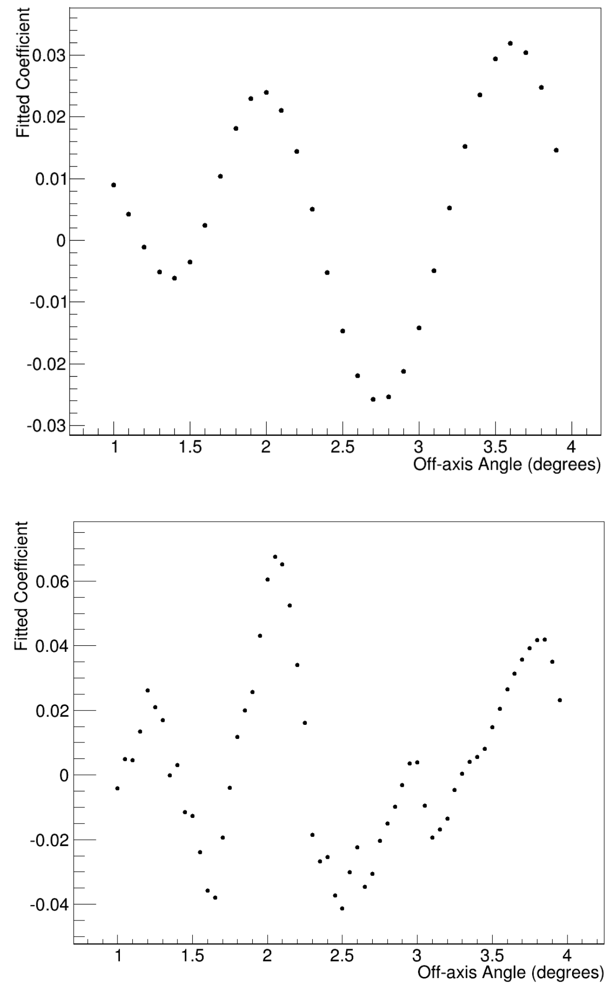

FIG. 17. The weights for each off-axis bin produced in the NuPRISM flux fits are shown after requiring that neighboring bins have similar values (top; as in Figure 18 left column) and with neighboring bins allowed to vary more freely relative to each other (bottom; as in Figure 18 right column).

The NuPRISM candidate events are events with a single observed muon ring and no-other observed particles, matching the selection applied at Super-K. After the $c_i\left(\theta_{23}, \Delta m^2_{32}\right)$ coefficients are derived, they are used to make linear combination of observed candidate event distributions from each NuPRISM off-axis bin. In this case the observables are the momentum and polar angle of the scattered muon candidate, and hence the expected Super-K distribution of these observables is predicted by the linear combination of observed NuPRISM events.

In order to use these NuPRISM measurements to make an accurate prediction of Super-K muon kinematics, a series of corrections are required. First, non-signal events from either neutral current events or charged current events with another final state particle above Cherenkov threshold, must be subtracted from each near detector slice. This is particularly important for neutral current events, which depend on the total flux rather than the oscillated flux at Super-K, but depend on the oscillated flux in the NuPRISM linear combination. This background subtraction is model dependent, and is a source of systematic uncertainty, although neutral current interactions can be well constrained by in situ measurements at NuPRISM. The differences in detector efficiency and resolution must also be corrected. The efficiency differences are due to differences in detector geometry and are largely independent of cross section modeling. Detector resolutions must be well determined from calibration data, but this effect is somewhat mitigated due to the fact that the near and far detector share the same detector technology. Finally, for the present analysis, the two dimensional muon momentum vs angle distribution is collapsed into a one dimensional E_{rec} distribution using a transfer matrix, $M_{i,p,\theta}\left(E_{rec}\right)$. This is an arbitrary choice that does not introduce model dependence into the final result, and has only been used for consistency with existing T2K ν_μ disappearance results. Future analyses can be conducted entirely in muon momentum and angle variables.

The final expression for the NuPRISM prediction for

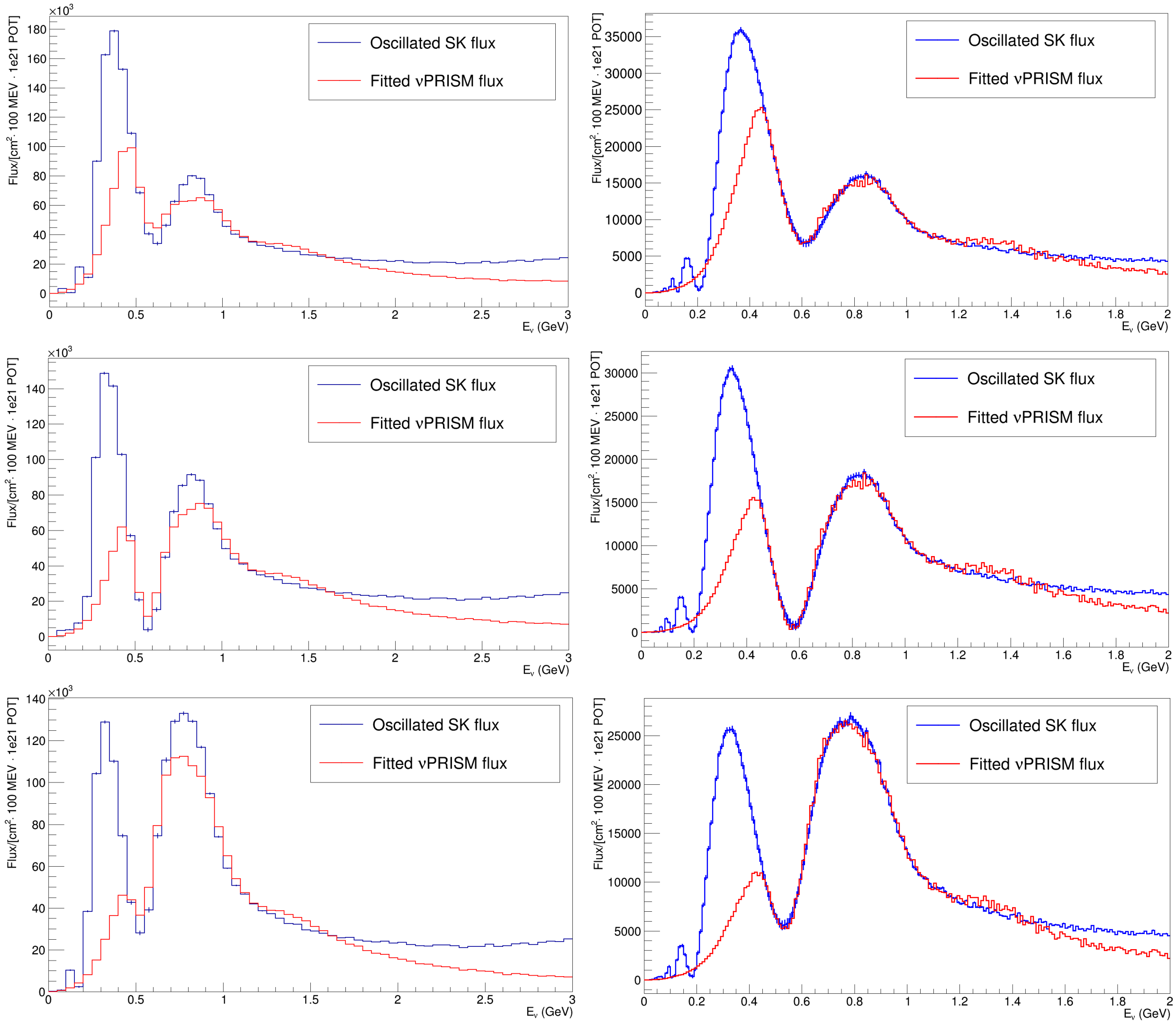

FIG. 18. Fits of the NuPRISM flux bins to oscillated Super-K fluxes are shown for three different sets of $(\theta_{23}, \Delta m^2_{32})$: top - $(0.61,\ 2.56 * 10^{-3})$, middle - $(0.48,\ 2.41 * 10^{-3})$, and bottom - $(0.41,\ 2.26 * 10^{-3})$. In the left column, the weights for the off-axis bins are forced to vary smoothly with off-axis angle, while in the right column they are allowed to vary more freely.

the Super-K event rate is then

$$N^{SK}\left(E_{rec}; \theta_{23}, \Delta m^2_{32}\right) = \delta\left(E_{rec}\right) + B^{SK}\left(E_{rec}; \theta_{23}, \Delta m^2_{32}\right) + \sum_{i=1}^{30} \sum_{p,\theta} c_i\left(\theta_{23}, \Delta m^2_{32}\right)\left(N^{\nu P}_{i,p,\theta} - B^{\nu P}_{i,p,\theta}\right) \times \frac{\epsilon^{SK}_{p,\theta}}{\epsilon^{\nu P}_{i,p,\theta}} M_{i,p,\theta}\left(E_{rec}\right), \tag{3}$$

where $N^{SK}\left(E_{rec}\right)$ and $N^{\nu P}_{i,p,\theta}$ are the number of expected events in Super-K E_{rec} bins and NuPRISM off-axis angle, muon momentum, and muon angle bins, respectively, $B^{SK}\left(E_{rec}\right)$ and $B^{\nu P}_{i,p,\theta}$ are the corresponding number of background events in these samples, and $\epsilon^{SK}_{p,\theta}$ and $\epsilon^{\nu P}_{i,p,\theta}$ are the efficiencies in each detector. The final correction factor, $\delta\left(E_{rec}\right)$, accounts for any residual differences between the NuPRISM prediction and the Super-K event rate predicted by the Monte Carlo simulation. These are mostly due to the previously described imperfect flux fitting, and the fact that NuPRISM is not sensitive to neutrino energies above $\sim$ 1.5 GeV since most muons at that energy are not contained within the inner detector. Comparisons of the Super-K event rate and the NuPRISM prediction for Super-K prior to applying the $\delta\left(E_{rec}\right)$ correction factor are given in Figure 19.

The NuPRISM technique effectively shifts uncertainties in neutrino cross section modeling into flux prediction systematic uncertainties. This is quite helpful in oscillation experiments since many flux systematic uncertainties cancel, and the important physical processes in the flux prediction, the hadronic scattering, can be directly measured by dedicated experiments using well characterized proton and pion beams. Figure 20 shows

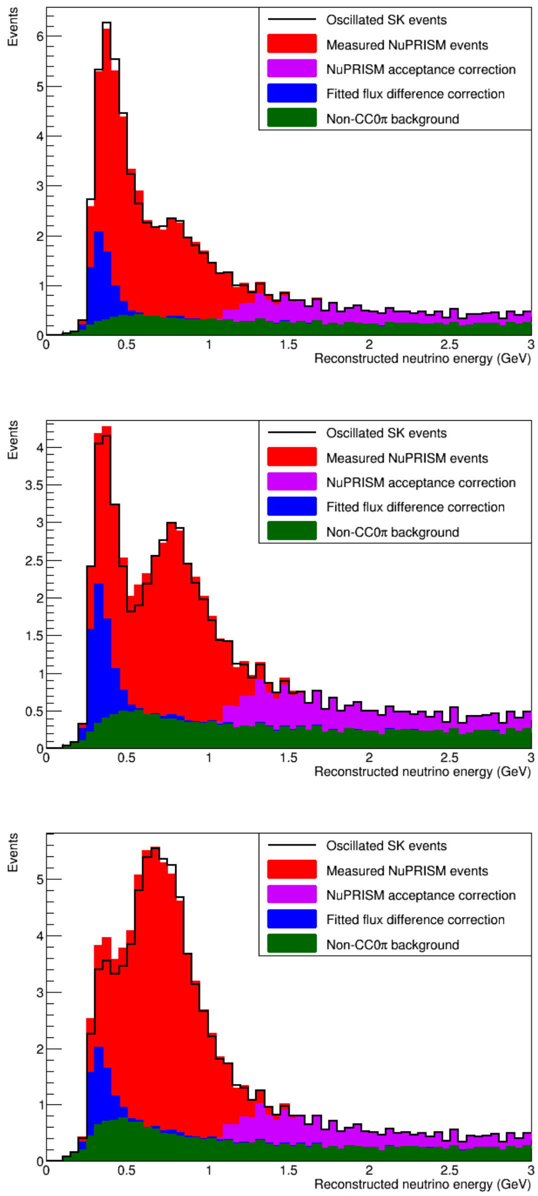

FIG. 19. The Super-K E_{rec} distributions and NuPRISM E_{rec} predictions corresponding to the flux fits in Figure 18 (left column) are shown. The red area shows the portion of the SK directly measured by NuPRISM, the blue are shows the correction needed due to the imperfect flux fit, the purple area shows the correction due to detector acceptance, and the green portion shows the SK NC backgrounds.

the effect of a few selected flux uncertainties on the Super-K energy spectrum and the NuPRISM linear combination. The largest flux uncertainty is due to pion production in proton-carbon interactions, but this uncertainty mostly cancels when applied at both the near and far detector. The more problematic uncertainties are those that affect the off-axis angle, such as horn current and proton beam positioning, since these effects will impact Super-K and the NuPRISM linear combinations differently. Figure 21 shows four examples of how the Super-K E_{rec} distribution and the corresponding NuPRISM predicted distribution vary for different throws of all the flux and cross section systematic uncertainties. The predicted spectra from the NuPRISM linear combination closely tracks the true spectrum at SK, indicating a correlated effect from most systematic parameters on the NuPRISM linear combination and SK event rates.

The final covariance matrices are shown in Figure 22. The largest errors are at high energies where no NuPRISM events are present due to the smaller diameter of the detector relative to Super-K. In this region, the Super-K prediction is subject to the full flux and cross section uncertainties with no cancelation at the near detector. Similarly, at energies below 400 MeV the errors get larger since the current 4° upper bound in off-axis angle prohibits the NuPRISM flux fit from matching the Super-K spectrum at low energies.

Using the NuPRISM covariance matrices shown in Figure 22 in place of those produced by ND280, the standard T2K ν_μ disappearance oscillation analysis is repeated. The results are shown in Figure 23. As expected, the NuPRISM analysis is largely insensitive to cross section modeling. Replacing the default new model with the Nieves multinucleon model now produces a 1.0% uncertainty in $\sin^2\theta_{23}$, and the corresponding Martini uncertainty is 1.2%. More importantly, this uncertainty is now constrained by data rather than a pure model comparison. These uncertainties are expected to be further reduced as the flux fits are improved, and NuPRISM constraints on NC backgrounds and information from ND280 are incorporated into the analysis.

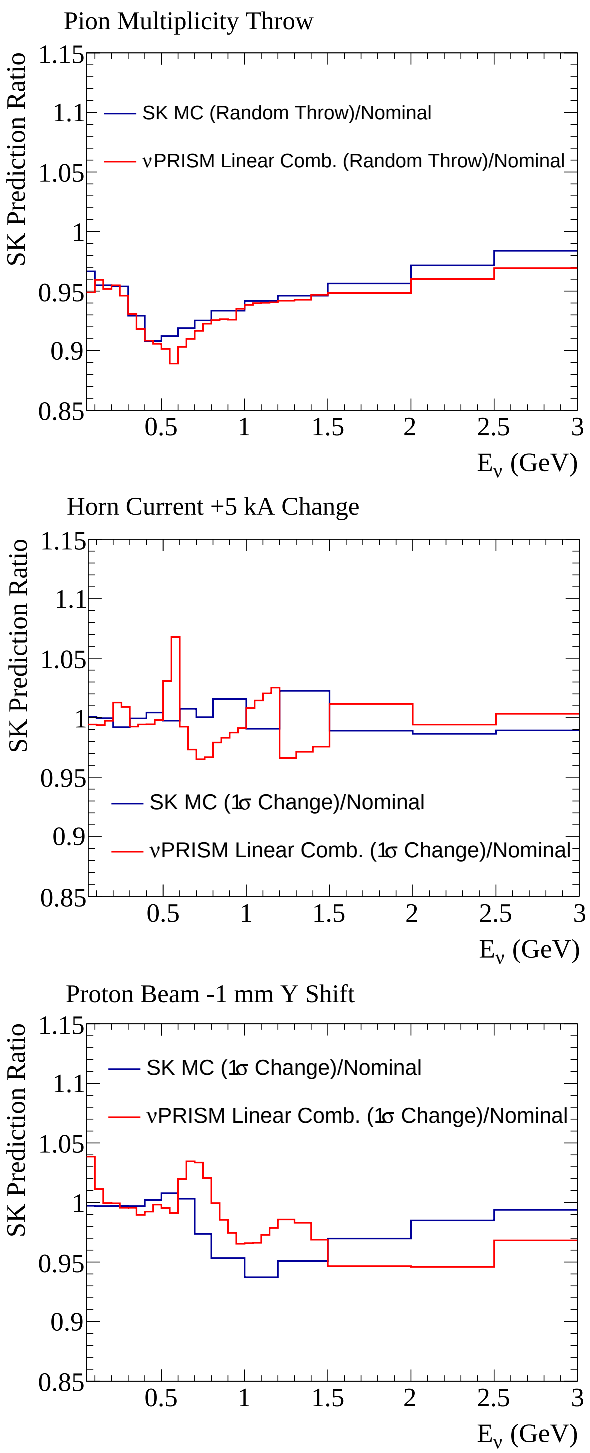

FIG. 20. Systematic uncertainties on the neutrino flux prediction due to pion production (top), horn current (middle), and proton beam y-position (bottom) are shown.

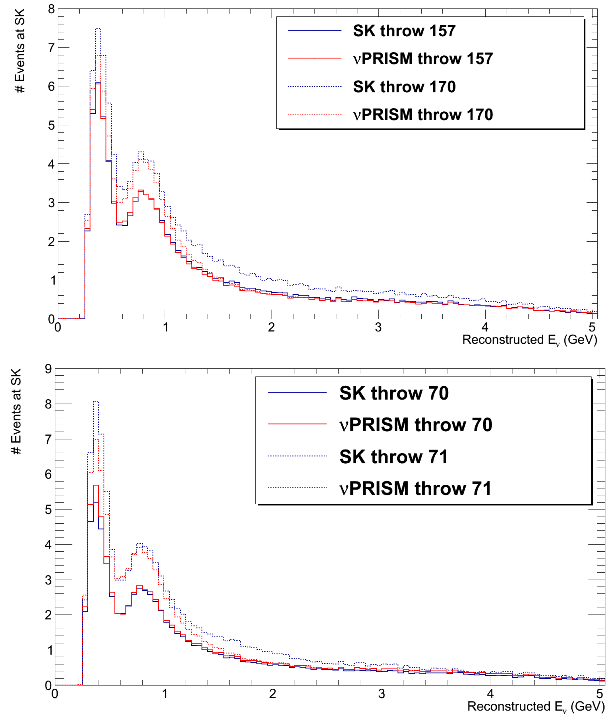

FIG. 21. Variations in the Super-K E_{rec} spectrum and the corresponding NuPRISM prediction are shown for 4 throws of all the flux and cross section parameters. Significant correlations exist between the the near and far detector, which help to reduce the systematic uncertainty.

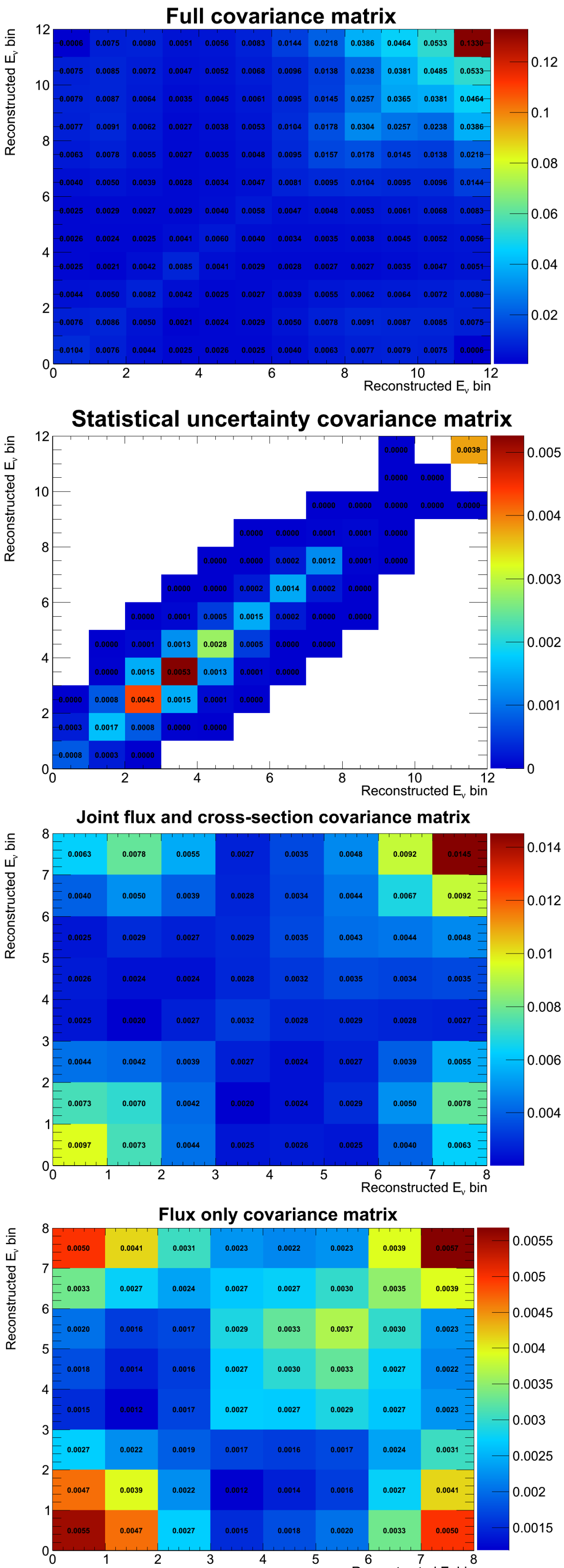

FIG. 22. Covariance matrices are shown (from top to bottom) for the total, statistical, systematic, and flux only uncertainties. The bin definitions (in GeV) are 0: (0.0,0.4), 1: (0.4,0.5), 2: (0.5,0.6), 3: (0.6,0.7), 4: (0.7,0.8), 5: (0.8,1.0), 6: (1.0,1.25), 7: (1.25,1.5), 8: (1.5,3.5), 9: (3.5,6.0), 10: (6.0,10.0), 11: (10.0,30.0)

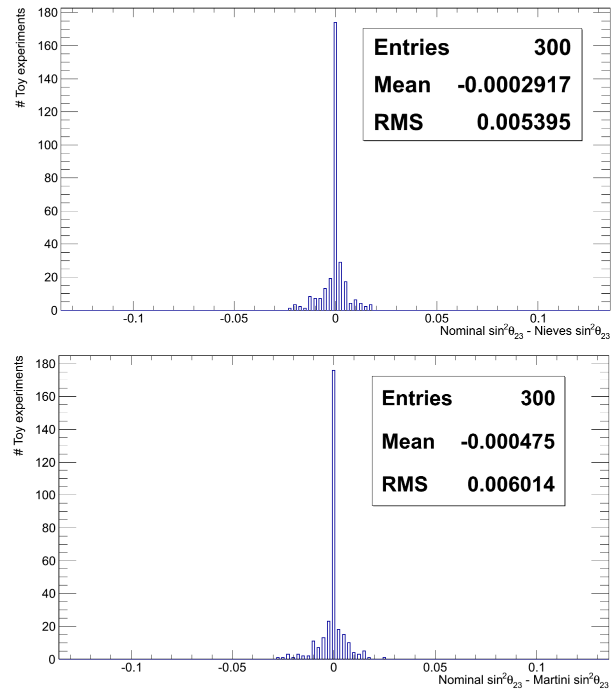

FIG. 23. The variation in the measured $\sin^2\theta_{23}$ due to multinucleon effects in the NuPRISM ν_μ analysis are shown. For the Nieves and Martini fake datasets, the RMS produces 1.0% and 1.2% uncertainties, respectively, with no measurable bias. This is a large improvement over the standard T2K results shown in Figure 15

G. NuPRISM Contributions to CP Violation Measurements

For the detection of CP violation in T2K phase 2 or Hyper-K, NuPRISM measurements should be used to predict the Super-K or Hyper-K 1Re candidate rates for neutrino and antineutrino mode. The method to use NuPRISM data to predicted the far detector 1Re rate will be described here for the neutrino mode operation of the beam. A similar method can also be applied for the antineutrino mode beam operation with the additional step of subtracted out the antineutrino mode wrong sign background using measurements made with the neutrin mode beam.

When using NuPRISM to predict the 1Rμ rate at the far detector (described in the previous section), a linear combination of NuPRISM off-axis slices is taken to more closely match the NuPRISM neutrino spectrum to the far detector neutrino spectrum after oscillations. This approach minimizes the cross section model dependence that enters when extrapolating near detector measurements made with a different neutrino spectrum than what is predicted at the far detector. For the 1Re predictions, the extrapolation is complicated further by the fact that the neutrino flavor has changed, so the interaction cross sections in the near and far detectors are different. Hence, for predicting the appearance candidate samples, a multi-step approach is necessary:

1. The $\sigma_{\nu_e}/\sigma_{\nu_\mu}$ ratio is measured in NuPRISM using the intrinsic ν_e component of the beam.

2. The final state lepton spectrum for the ν_e appearance signal at the far detector is predicted using the linear combination method and 1Rμ candidates in NuPRISM. The model is used to correct for the cross-section ratio $\sigma_{\nu_e}/\sigma_{\nu_\mu}$, and this model is constrained by the measurement made in the first step.

3. The intrisic ν_e and neutral current backgrounds are predicted by measuring the ν_e candidate rate at the 2.5° off-axis position in NuPRISM.

1. *Measurement of $\sigma_{\nu_e}/\sigma_{\nu_\mu}$*

The intrinsic beam ν_e represents only 1% of the total neutrino flux and about 0.5% at the off-axis peak energy at E_ν=600MeV. Thanks to the excellent μ/e particle identification and π^0 suppression in water Cherenkov detectors when using fiTQun, the ν_μ background is expected to be suppressed, similar to the suppression seen at Super-K. Since the beam ν_e's originate from three body decays of muons and kaons, their off-axis dependence is more mild than the dependence seen in the ν_μ flux. By taking advantage of the steep off-axis angle dependence of the ν_μ flux, it is possible to study background contamination in detail. For example, the ν_μ backgrounds are largely suppressed compared to beam ν_e at an off-axis angle larger than 2.5 degrees. The beam ν_e events at NuPRISM provide an opportunity to precisely study ν_e cross sections, for which there is currently very little data available. The cross section difference between ν_e and ν_μ, which does not cancel in the near to far detector extrapolation in $\nu_\mu \to \nu_e$ appearance, is considered to be an eventual limitation of the CP violation sensitivity [33]. The differences in the ν_e and ν_μ cross sections arise from kinematical phase space differences due to the difference in mass between electron and muons, radiative corrections, possible second class currents, which also depend on lepton mass, and nuclear effects [8].

Measurements of the cross section for electron (anti)neutrino scattering on nuclei at $\mathcal{O}(1\text{ GeV})$ are challenging due to the small ν_e content of conventional neutrino beams. NuPRISM has a number of features that will allow it to measure the cross section ratio $\sigma_{\nu_e}/\sigma_{\nu_\mu}$ with unprecedented precision:

- NuPRISM extends to 4° off-axis. At 4° the low energy ν_e fraction of the beam relative to ν_μ is 50% larger than it is as 2.5° off-axis. This will allow for the selecton of higher purity ν_e candidate samples.

- By using the active outer detector as a veto and applying tight fiducial volume cuts, NuPRISM can strongly reject backgrounds from photons produced in ν_μ interactions.

- Water Cherenkov detectors can now reject most NCπ^0 background events. The current T2K-SK ν_e event selection removes 99.5% of all events containing a π^0 that are produced in the SK fiducial volume.

- For the measurement of the ratio $\sigma_{\nu_e}/\sigma_{\nu_\mu}$, the ν_μ flux can be matched to the ν_e flux using the linear combination method, ensuring that observed differences can be attributed to cross section differences and not flux differences.

The selection of 1Re ν_e-CC candidates in NuPRISM is studied with a simulation of neutrino interactions in the NuPRISM detector with the WCSim based simulation. Event reconstruction is applied using fiTQun, and candidate events are required to have a single electron-like ring, no Michel electron candidates, a reconstructed vertex more than 135 cm from the detector wall, a distance to the detector wall along the candidate electron direction of propagation of more than 275 cm, visible energy of more than 100 MeV and the event must be contained. Each event is also fitted with a π^0 hypothesis and rejected if it is consistent with a π^0 candidate The 1Re selection is applied to events in the 2.5-4.0° off-axis range, where it is assumed that 1.5×10^{21} POT are accumulated for each position of the NuPRISM detector in the verticle shaft. This POT assumes 7.5×10^{21} POT are accumulated in neutrino mode after NuPRISM is built.

The selected 1Re candidates in bins of neutrino energy are shown in Fig. 24. Below a reconstructed energy of

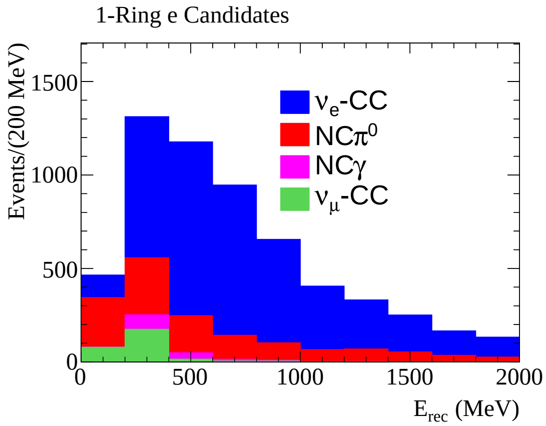

FIG. 24. Selected 1Re candidates in the 2.5-4.0° off-axis range for NuPRISM.

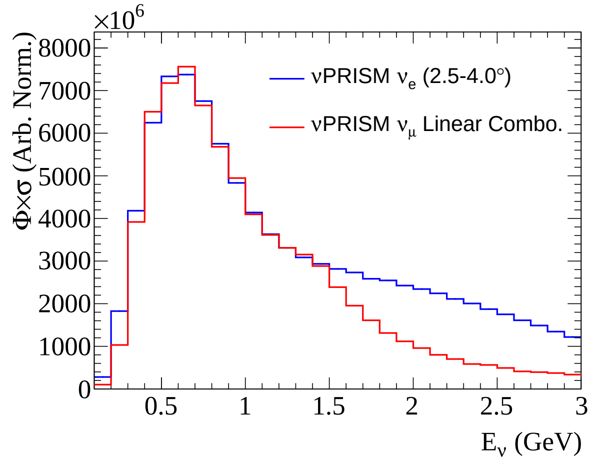

FIG. 25. The intrinsic ν_e spectrum and the matched ν_μ spectrum using the linear combination method.

1.2 GeV, the purity for ν_e-CC events is 71% and the expected signal is 3500 events. It should be noted that this simulation was carried out with 3 m radius inner detector. Since the time of this work, the baseline design for NuPRISM has changed to a 4 m radius inner detector and new Monte Carlo simulations are being generated. The larger inner detector will give an increased event rate due to the larger fiducial volume and higher purity since the particle ID performance improves as the distance to the detector wall increases. Additional tuning of the fiTQun π^0 rejection is also planned, but has not yet been implemented.

The $\sigma_{\nu_e}/\sigma_{\nu_\mu}$ ratio measurement is best carried out with the same energy spectrum for ν_e and ν_μ fluxes so that differences in the measured ratio can be attributed to cross-section differences. The ν_μ spectrum is matched to the ν_e spectrum using the linear combination of off-axis spectra that has been previously described. Fig. 25 shows the matched ν_μ, which has good agreement with the ν_e spectrum up to 1.5 GeV. Agreement up to 1.5 GeV is sufficient since ν_μ interactions above 1.5 GeV will typically produce muons that are not contained in the NuPRISM inner detector. It is also the case that the $\nu_e(\bar{\nu}_e)$ appearance probabilities and CP violation effect are dominant below 1 GeV, so it is most important to measure the relative cross-section in the sub GeV region.

Using the simulated and selected 1Re candidates, we have estimated the expected uncertainty on the $\sigma_{\nu_e}/\sigma_{\nu_\mu}$ ratio measurement. The uncertainty on the ratio of the fluxes $\Phi_{\nu_e}/\Phi_{\nu_\mu}$ is estimated using the T2K flux systematic error model with the assumption that hadron production errors will be reduced to 1/2 of their current values with replica target measurements and new thin target measurements. As mentioned previously, the linear combination of NuPRISM ν_μ spectra is matched to the intrinsic NuPRISM ν_e spectrum, as shown in Fig. 25, and the flux error estimate is evaluated on this linear combination. The statistical error is estimated for the background subtracted signal. Systematic errors on the background modeling are assumed to be 5% for NCπ^0 and $\nu_\mu - CC$ backgrounds since these can be constrained with control samples in NuPRISM. The error on the modeling of the NC1γ background is set to 50%, which is conservative compared to an estimate of 12% by Wang *et al* [34]. It is assumed that a relative signal efficiency of 1% between 1Re and 1Rμ candidates can be achieved.

The estimate of the uncertainty on the $\sigma_{\nu_e}/\sigma_{\nu_\mu}$ as a function of reconstructed energy is shown in Fig. 26. For the region below a reconstructed energy of 1 GeV, the estimated total error is ∼4.5%. It is expected that this will be reduced with the change to a 4 m radius inner detector, and additional tuning of the reconstruction. The uncertainty on the $\Phi_{\nu_e}/\Phi_{\nu_\mu}$ flux ratio is the dominant error at 3.2% and may be reduced by more precise hadron production measurements.

The measurement of the $\sigma_{\bar{\nu}_e}/\sigma_{\bar{\nu}_\mu}$ ratio does present additional challenges beyond the $\sigma_{\nu_e}/\sigma_{\nu_\mu}$ measurement. The lower antineutrino interaction cross section implies a smaller statistical sample, however Hyper-K will use a longer exposure with the antineutrino beam so as to balance the total event rates for neutrinos and antineutrinos. Hence, we expect a similar statistical precision can be achieved for the $\sigma_{\bar{\nu}_e}/\sigma_{\bar{\nu}_\mu}$ ratio. The $\bar{\nu_e}$ candidate sample will include a larger neutral current background, so the purity of the electron reconstruction is most important for the antineutrino measurement. The antineutrino candidates also have a significant wrong-sign (neutrino) background. The wrong-sign background can be constrained by the measurement made in the neutrino beam.

2. *Event Rate Prediction Ignoring σ_{ν_e} σ_{ν_μ} differences*

The linear combination method can be applied to reproduce the predicted SK spectrum from $\nu_\mu \rightarrow \nu_e$ oscil-

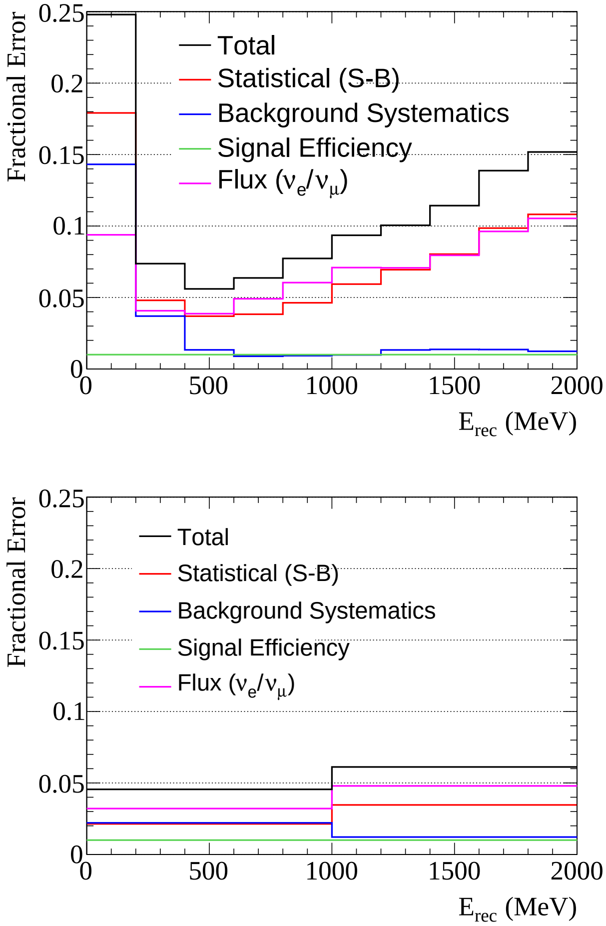

FIG. 26. The estimates of the uncertainties on the $\sigma_{\nu_e}/\sigma_{\nu_\mu}$ measurement in 200 MeV (top) and 1 GeV (bottom) bins of reconstructed energy.

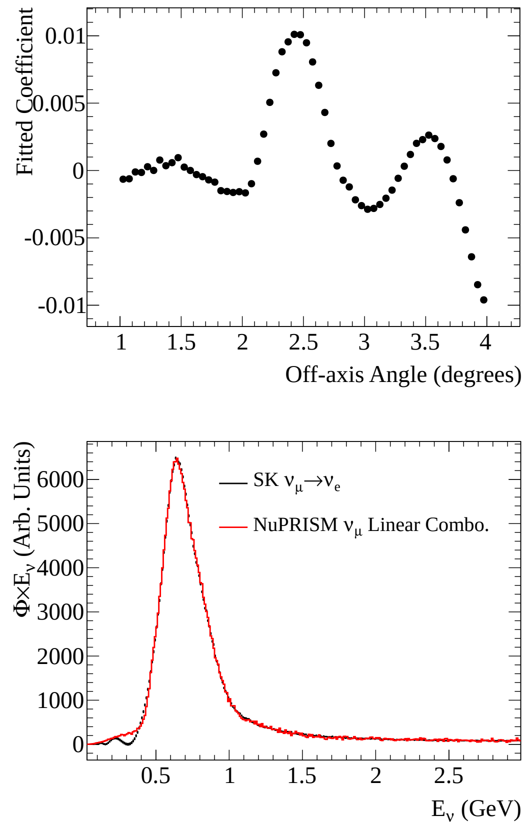

FIG. 27. The coefficients (left) and linear combination of NuPRISM spectra (right) that reproduce the Super-K $\nu_\mu \rightarrow \nu_e$ spectrum with $\sin^2 2\theta_{13}$=0.95 and $\delta_{CP} = 0$.

lations using the ν_μ off-axis spectra in NuPRISM. Fig. 27 shows the linear combination that matches the far detector spectrum for $\sin^2 2\theta_{13}$=0.95 and $\delta_{CP} = 0$. Similar agreement can be achieved for other choices of the oscillation parameters.

The coefficients in Fig. 27, are used to sum the measured muon $p_\mu - \theta_\mu$ distributions in NuPRISM, predicting the expected muon $p_\mu - \theta_\mu$ distribution for a ν_μ spectrum that matches the Super-K $\nu_\mu \rightarrow \nu_e$ spectrum. To predict the $p_e - \theta_e$ spectrum at Super-K from $\nu_\mu \rightarrow \nu_e$ oscillations, an additional model dependent correction for the difference in the σ_{ν_e} and σ_{ν_μ} cross sections must be applied. This model dependent correction is constrained by the $\sigma_{\nu_e}/\sigma_{\nu_\mu}$ cross section ratio measurement described in Section III G 1.

NuPRISM and Super-K/Hyper-K share target nuclei and are both unable to detect pions below Cherenkov threshold that don't produce a decay electron. We expect that final state pion interactions and secondary pion interactions in the detectors will have a similar effect in NuPRISM and the far detectors. Furthermore, if the linear combination of NuPRISM spectra match the SK spectrum, the initial spectrum of pions produced in the neutrino-nucleus interactions should be identical for NuPRISM and the far detector. Hence, the effect of final state and secondary interactions, one of the largest will be directly measured in NuPRISM and accounted for in the prediction of the far detector event distributions using the NuPRISM linear combination. However, since we observe ν_μ interactions in NuPRISM and predict rates for ν_e interactions in the far detector, there will be a difference in the initial pion spectra in NuPRISM and the far detector. This difference will introduce an additional model dependence in the extrapolation that accounts for the effect of the charged lepton mass difference on the initial pion spectrum. Fig. 28 shows the predicted initial π^+ spectra for ν_e-CC and ν_μ-CC interactions from identical neutrino spectra with 1Re and 1Rμ selections applied respectively. The differences in the spectra are small, so we can assume that the model dependent correction applied to account for charged lepton mass difference on the pion spectra will be small. It should also be noted that the final state and secondary interactions for ν_e-CC and ν_μ-CC will also be constrained by the $\sigma_{\nu_e}/\sigma_{\nu_\mu}$ cross section ratio measurement described in Section III G 1.

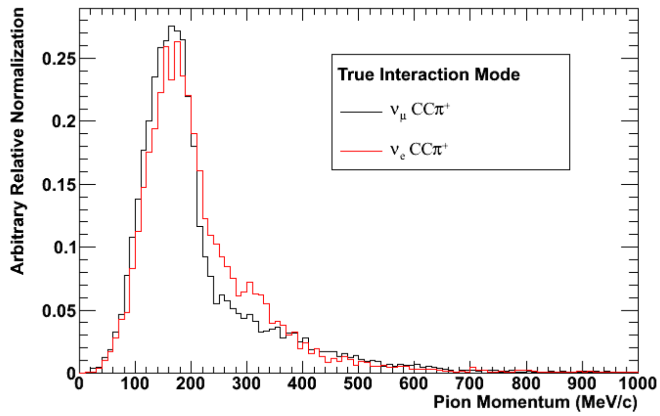

FIG. 28. The π^+ spectra after final state interactions in simulated ν_e-CC and ν_μ-CC events in SK generated with identical spectra and with 1Re and 1Rμ selections applied respectively.

3. *Measurement of the intrinsic backgrounds*

In the 2.5° off-axis slice of NuPRISM, the spectra for neutral current interactions and intrinsic ν_e are nearly identical to those at Super-K, as shown in Fig. 29. The intrinsic 1Re backgrounds can be directly measured in NuPRISM without resorting to the linear combination method by measuring the rates at 2.5° off-axis. This measurement only requires a small model dependent correction for the <10% flux differences between NuPRISM and Super-K, and a correction for the relative efficiency between NuPRISM and Super-K.

The measured intrinsic 1Re background in the 2.4-2.6° reconstructed off-axis angle range for an exposure of 1.5×10^{21} POT is shown in Fig. 30. The expected number of events with reconstructed energy less than 1.2 GeV is 933, giving a statistical precision of 3%. The statistics will increase with the move to a 4 m radius inner detector.

H. Sterile Neutrino Sensitivity

The NuPRISM detector will provide a unique and sensitive search for sterile neutrinos in the $\nu_\mu \to \nu_e$ channel, and eventually the $\nu_\mu \to \nu_\mu$ channel, particularly when ND280 is incorporated into the analysis. The 1km location of NuPRISM for the off-axis peak energies of 0.5-1.0GeV matches the oscillation maximum for the sterile neutrinos hinted by LSND and MiniBooNE. The presence or absence of an excess of ν_e events as a function of off-axis angle will provide a unique constraint to rule out many currently proposed explanations of the MiniBooNE excess, such as feed-down in neutrino energy due to nuclear effects. The off-axis information also allows for a detailed understanding of the backgrounds, since they have a different dependence on off-axis angle than

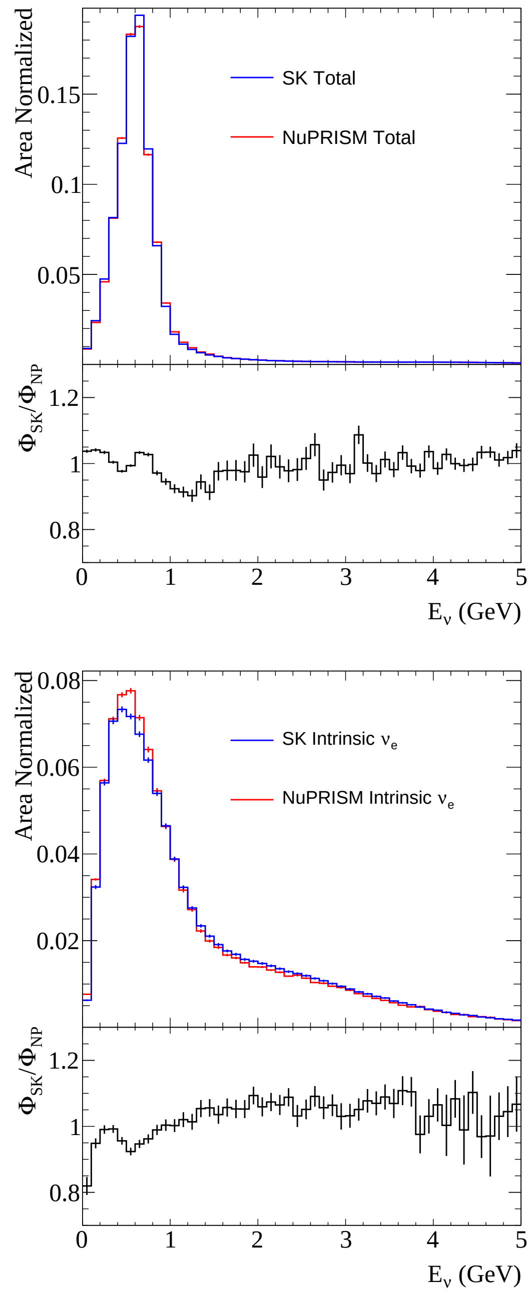

FIG. 29. The spectra for all neutrinos (left) and intrinsic ν_e (right) at NuPRISM and Super-K and the ratio of area normalized spectra at NuPRISM and SK. For NuPRISM, the spectra are chose for the 2.4-2.6° off-axis angle range, corresponding to region of transverse size of 3.5 m in NuPRISM.

the oscillated signal events.

Figure 31 shows the single ring e-like events observed by MiniBooNE. There are several sources of events:

- Beam ν_e from muon and kaon decays
- NCπ^0 with one of the photons missed

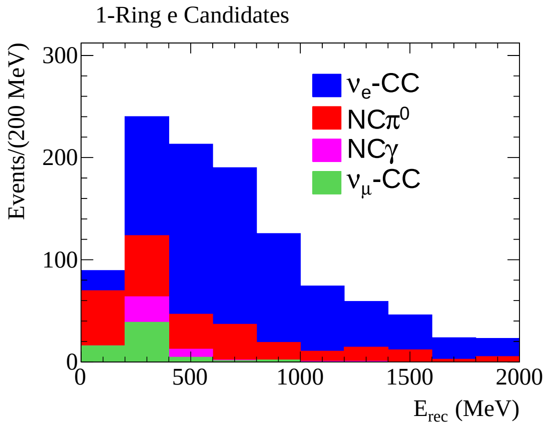

FIG. 30. The reconstructed energy spectrum intrinsic 1Re background measured in the NuPRISM 2.4-2.6° reconstructed off-axis angle range for an exposure of 1.5×10^{21} POT.

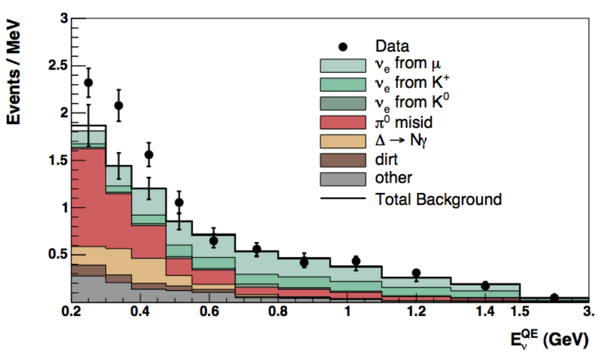

FIG. 31. Reconstructed neutrino energy distribution for the ν_e appearance analysis of MiniBooNE [32].

- NCγ ($\Delta \rightarrow N\gamma$)
- "Dirt" events: background γ coming from outside
- Others, such as CC events with μ misidentified as electron
- Possible sterile neutrino contribution causing $\nu_\mu \rightarrow \nu_e$ oscillation

There is a significant discrepancy between data and the Monte Carlo prediction. For precision ν_e appearance studies, such as CP violation, it is essential to understand the origin of this discrepancy.

This section presents an initial, conservative sensitivity of NuPRISM to sterile neutrino oscillations. The present sensitivities are based on reconstruction efficiencies taken from Super-K, which performs much worse near the wall than NuPRISM due to the much coarser granularity provided by 20-inch PMTs relative to 8-inch PMTs. In addition, we do not yet incorporate any constraints on the backgrounds from in situ measurements in NuPRISM, and thus the full T2K neutrino cross section uncertainty is assumed for each background process. This is a particularly conservative assumption for NCπ^0 events, since this process will be measured to high precision with NuPRISM. Finally, the T2K near detector, ND280, provides a secondary measurement at a much shorter baseline, and on a water target, which can further constrain flux and cross section uncertainties, however no information from ND280 has been incorporated into the measurement at this stage.

The LSND and MiniBooNE experiments detect an undetermined excess in their ν_e and $\overline{\nu}_e$ channels, which may be explained by sterile neutrino mixing with a $\sin^2(2\theta_{\mu e}) \sim 10^{-3}$ and $\Delta m^2_{41} \sim 2eV^2$ in the 3+1 model [32].

The sensitivity studies in this section assume a 4 m inner detector and an exposure of 7.5×10^{20} p.o.t with a horn configuration enhancing neutrinos and defocusing antineutrinos. The possible ν_e disappearance due to sterile mixing is neglected as in the case of the LSND analysis. This is justified by the fact that ν_e composes only 1% of the beam and the $\nu_\mu \rightarrow \nu_e$ channel will be dominant. For simplicity, the effect of ν_μ disappearance was also neglected, although this is done in order to establish a first comparison to the LSND results. In the case where both ν_e appearance and ν_μ disappearance signals are considered, the sensitivity to the mixing angle is expected to improved, and the results shown here can be considered a conservative estimate.

We test the simplest sterile neutrino model by adding to the standard three-neutrino parametrization one additional mass state, mainly sterile, with a squared mass difference to the other states Δm^2_{41}. Since the mixing with the sterile neutrino is dominant at short baselines, such as the NuPRISM baseline, the new mass state is expected to be of the order of 1 eV^2. Such heavy mass state, much larger than the two standard neutrino mass splittings, makes the two-neutrino approximation to be valid. The ν_e appearance probability can be then written as:

$$P_{\nu_\mu \rightarrow \nu_e} = \sin^2(2\theta_{\mu e}) \sin^2 \left(1.27 \Delta m^2_{41} [eV^2] \frac{L[km]}{E[GeV]} \right) \tag{4}$$

where L is the neutrino flight path fixed at 1 km, and E is the energy of the neutrinos. The effective mixing angle could be rewritten in terms of the extended PMNS matrix, U, in the way $\sin^2(2\theta_{\mu e}) = 4|U_{\mu 4}|^2 |U_{e4}|^2$. We consider an analysis on both the reconstructed energy (E_{Rec}) and the off-axis angle (OAA) shape information, so both rate and shape are taken into account by building bidimensional binned templates. Although we are neglecting any possible effect coming from a short baseline muon neutrino disappearance, we use muon neutrino candidate events to constrain flux and cross section uncertainties affecting the estimation of the nue signal events.

Both ν_μ selection events and $\nu_\mu \rightarrow \nu_e$ appearance signal events for different oscillation hypothesis are presented in Table V.

The systematic errors due to the flux and cross-section uncertainties are included through a covariance matrix

TABLE V. number of events for ν_μ selection and expected number of signal events for ν_e selection (for each oscillation hypothesis)

ν_μ Selection		
		Events
ν_μ		1.689×10^6
ν_e Selection		
	$(\sin^2(2\theta_{\mu e}), \Delta m^2_{41})$	Events
$\nu_\mu \to \nu_e$	(0.013, 0.43)	4158.1
	(0.001, 1)	456.6
	(0.005, 1)	2283.2
	(0.01, 10)	3657.4
	(0.001, 10)	365.7

calculated using toy Monte Carlo throws. We performed a χ^2 test for a binned template of 10 E_{Rec} bins between 0.2 GeV and 4 GeV and 10 OAA bins between 1° and 4° for both ν_e and ν_μ selections, in order to obtain the expected sensitivity in the bidimensional oscillation parameter space $(\sin^2(2\theta_{\mu e}), \Delta m^2_{41})$. For each oscillation hypothesis, the χ^2 value is given by:

$$\chi^2 = \vec{n_s}(\sin^2(2\theta_{\mu e}), \Delta m^2_{41})^T \times V^{-1} \times \times \vec{n_s}(\sin^2(2\theta_{\mu e}), \Delta m^2_{41}), \quad (5)$$

where $\vec{n_s}$ is a vector of 200 elements (in E_{Rec} and OAA bins) containing the number of expected ν_e appearance signal events in the first 100 entries, followed by the expected number of events due to the muon neutrino disappearance. These last entries are all set to 0 since we assumed no ν_μ disappearance. V is a thus a 200×200 covariance matrix including the statistical and systematic errors for both ν_e and ν_μ selections. This V matrix is constructed in the following way:

$$V = \begin{pmatrix} W_{ee} & W_{e\mu} \\ W_{\mu e} & W_{\mu\mu} \end{pmatrix}, \quad (6)$$

where W_{ee} and $W_{\mu\mu}$ involve statistical and systematic errors coming only from ν_e and ν_μ selections, respectively; while $W_{e\mu}$ and $W_{\mu e}$ take into account the correlations between both selections. In Figure 32, we can see that the correlations between ν_e and ν_μ are significant.

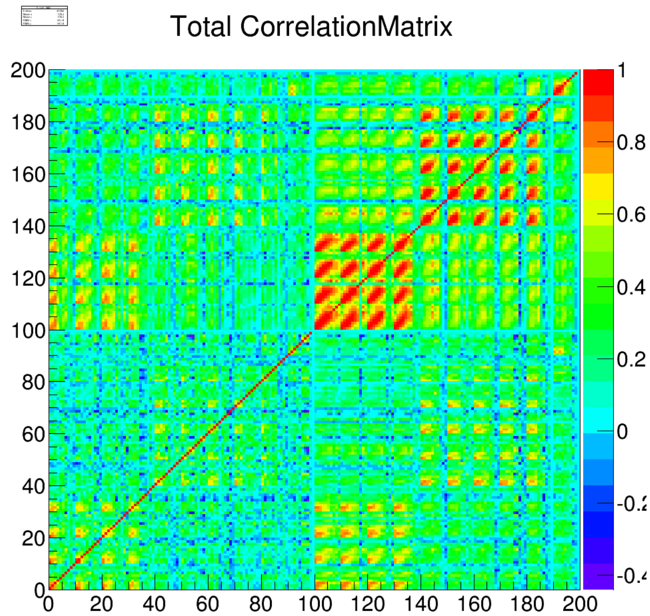

FIG. 32. Correlation matrix corresponding to V covariance matrix, including both flux and cross-section systematic uncertainties

1. Background

The background after the final event selection is composed of electron-like reconstructed events coming from two different sources: a) the intrinsic ν_e contamination of the incident ν_μ neutrino flux; and b) events coming from ν_μ neutrinos which are reconstructed as electron-like events. The two background components have been investigated respectively in terms of their origin (parent particle) or their interaction mode. The ν_e intrinsic background mainly come from μ^+ decay and, at higher energy, from K^+ decay. Background events coming from ν_μ have been instead classified into 5 categories based on the neutrino interaction mode. We distinguish between events having a π^0 in the final state ($CC\nu_\mu\pi^0$ and $NC\nu_\mu\pi^0$), $CCQE\nu_\mu$ (misreconstructed as electron-like) and other events coming from both NC and CC but with no π^0 in the final state. Figure 33 show the Monte Carlo energy spectrum for background events broken down into its different contributions. A ν_e appearance signal simulated for the oscillation hypothesis $\Delta m^2_{41} = 0.43\ eV^2$ and $\sin^2(2\theta_{\mu e}) = 0.013$ is also shown. The dominant component comes from $NC\nu_\mu\pi^0$ events, where a photon coming from the π^0 decay has been identified as an electron. The ν_μ background, dominant in the low energy region, quickly decrease and its contribution become almost negligible for $E_{rec} \sim 1$ GeV. On the contrary, the ν_e intrinsic background presents a longer tail, characteristic of the 3-body decay kinematics from which they are generated.

A unique feature of measuring sterile neutrinos in NuPRISM is the variation in background composition as a function of the off-axis angle. This can be seen by dividing the off-axis range of 1.1 to 3.9 degrees into 4 bins, as shown in Figure 34. The signal and background shapes show significantly different responses to changes in the off-axis angle.

Table VI summarizes the signal and background event rates as a function of off-axis angle. Both the NC and CC components are reduced by an order of magnitude when moving to the highest off-axis angles. On the contrary,

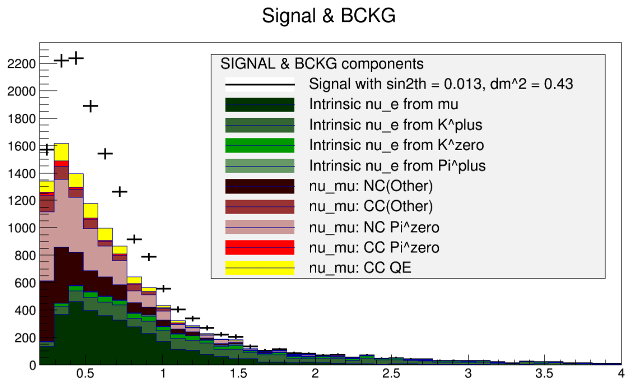

FIG. 33. Background broken down by component and signal for sterile mixing parameters $\sin^2(2\theta_\mu e) = 0.013$ and $\Delta m^2_{41} = 0.43\ eV^2$

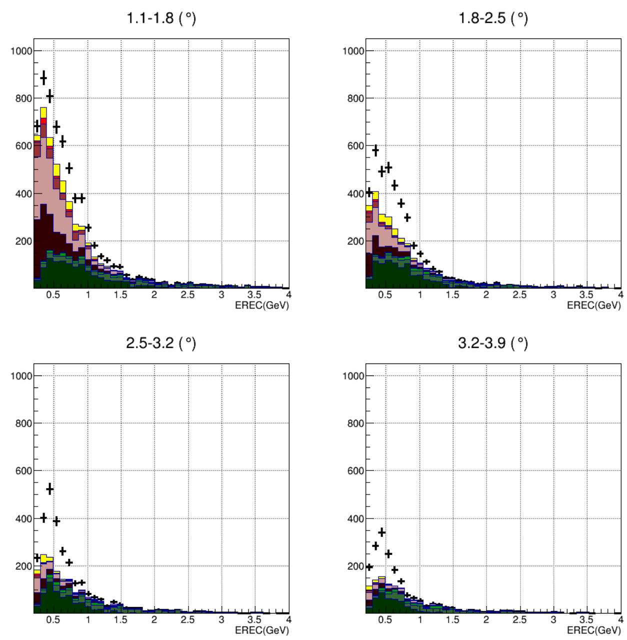

FIG. 34. Background broken-down by component and for 4 slices in OAA range, and signal for sterile mixing parameters $\sin^2(2\theta_\mu e) = 0.013$ and $\Delta m^2_{41} = 0.43\ eV^2$

the intrinsic background components (especially coming from K^+ and K^0) almost remain constant. This characteristic behavior of the intrinsic background can also be used to isolate a pure sample of ν_e events to perform cross-section measurements.

2. *Systematics*

To estimate of the size of the flux and cross section uncertainties, we consider the diagonal terms of the covariance matrix built separately for each source of background: for the intrinsic component (K^+, K^0, μ^+ and π^+), and also for the NC ($NC\nu_\mu\pi^0$ and $NC\nu_\mu Other$) and CC ($CC\nu_\mu\pi^0$ and $CC\nu_\mu Other$) components.

From this study, we observe that the NC component is the largest source of systematic errors only in the low OAA and reconstructed energy region. Furthermore, we noticed that the CC component error sizes are quite smaller than the NC. In the high OAA and reconstructed energy region, the dominant source of systematics is instead related to the instrinsic ν_e component.

Since this intrinsic component is an irreducible background, we conclude that the main efforts should go in the direction of reducing the rest of the components of the background (specially the NC).

TABLE VI. Expected number of events for every component of the background as a function the OAA.

OAA(°)	1.1-1.8	1.8-2.5	2.5-3.2	3.2-3.9
BCKG: ν_e Component				
K^+	443	440	391	347
μ^+	1168	949	669	423
K^0	184	141	155	125
π^+	17	25	22	9
BCKG: ν_μ Component				
$CCQE\nu_\mu$	332	196	98	44
$CC\nu_\mu\pi^0$	78	31	15	8
$NC\nu_\mu\pi^0$	1454	558	231	131
$CC\nu_\mu Other$	328	129	32	24
$NC\nu_\mu Other$	1029	368	198	119

3. *Sensitivity*

The χ^2 is computed for each point of a bidimensional grid and the constant $\Delta\chi^2$ method is applied to determine the contours for the regions excluded at the 90%, 3σ and 5σ C.L. The resulting NuPRISM sensitivity is presented in Figure 35 (top) and compared to the LSND allowed region.

Despite the current conservative assumptions on the size of the NC background and its uncertainty, NuPRISM can provide a precise check of the LSND/MiniBooNE oscillation signal, comparable to the sensitivity of the upcoming Fermilab short-baseline program, by covering the LSND 90% allowed range at 5σ for all values of Δm^2 outside of 2 eV^2. As the analysis matures, and information from ND280 is incorporated, additional improvements in the sensitivities are expected.

I. Atmospheric neutrino CP violation

The observed atmospheric neutrino rates at Super-K with energy below $\sim$ 1 GeV are sensitive to the CP phase

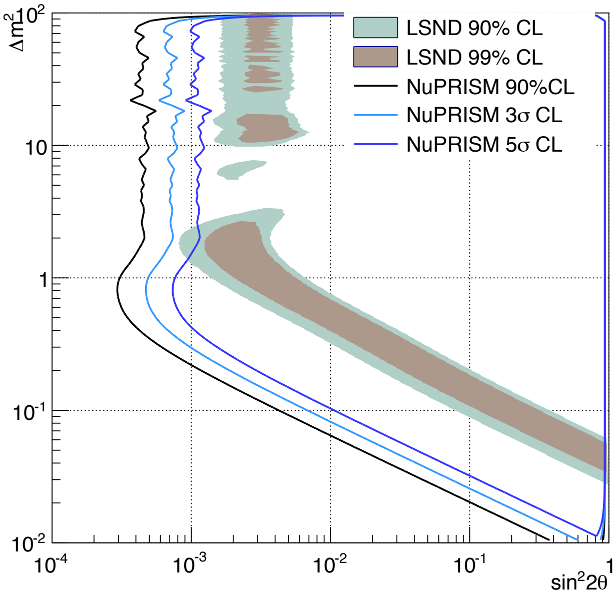

FIG. 35. 90%, 3σ and 5σ C.L. expected sensitivities for an exposure of 7.5×10^{20} POT for statistical uncertainties with flux and cross-section systematic uncertainties. For comparison, the LSND allowed region at 90% and 99% C.L. is also showed.

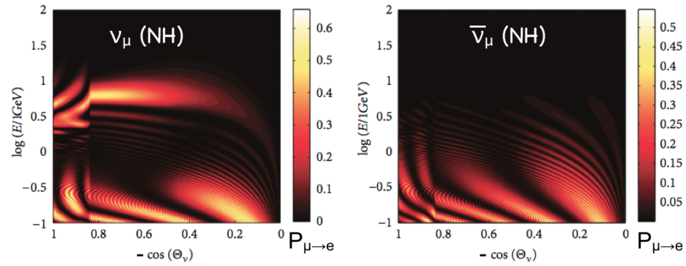

FIG. 36. $\nu_\mu \to \nu_e$ oscillation probability in neutrino energy, $log_{10}(E_\nu)$, vesus zenith angle, $\cos\theta_Z$, space (oscillogram). Left plot is for neutrinos with the normal hierarchy and the right plot is for antineutirnos with the normal hierarchy.

δ_{CP}. While the fractional change to the observed rate due to the value of δ_{CP} is small, it is statistically significant due to the large number of sub-GeV atmospheric neutrino candidates. Hence, the measurement is limited by systematic uncertainties on the neutrino rates. NuPRISM can play a role in this measurement through the reduction of the cross section systematic uncertainties. The measurement and need for NuPRISM inputs are described here.

Atmospheric neutrinos provide baseline lengths of up to 13,000 km which can be tagged by the zenith angle of the charged lepton produced in the charged current interactions of the neutrinos. The availability of neutrinos and antineutrinos of both electron and muon flavors over this wide range of baseline lengths and energies provides rich information about the neutrino oscillations. The matter effect gives additional information such as determination of the mass hierarchy.

Figure 36 shows the $\nu_\mu \to \nu_e$ oscillation probability assuming the normal hierarchy for neutrinos (left) and antineutrinos (right). The vertical axis is the neutrino energy, $log_{10}E_\nu$, and the horizontal axis is the zenith angle, $\cos\theta_Z$. There is a large enhancement for upward going ($\cos\theta_Z \sim -1$) neutrinos at several GeV but not for antineutrinos. In the case of inverted hierarchy, the resonance appears for antineutrinos instead of neutrinos, allowing the study of the neutrino mass hierarchy. There is also a strong interference patterns in the sub-GeV region, which comes from the θ_{12} oscillation. The atmospheric neutrino flux is the largest in this sub-GeV region, and SuperK has already accumulated more than 10,000 sub-GeV ν_e events over 5000 days of running.

The subGeV oscillation pattern comes from the $\nu_\mu \to \nu_e$ and $\bar{\nu}_\mu \to \bar{\nu}_e$ appearance oscillations as well as the original cosmic ν_e's and $\bar{\nu}_e$'s oscillating away (disappearance). Since the anti-neutrino cross section is a factor of 4 smaller than neutrino cross section in the sub-GeV energy range, mainly neutrinos are detected. Because ν_e's can disappear into ν_μ and ν_τ, the probability of ν_e disappearance, $P_{e\mu} + P_{e\tau} \sim 2P_{e\mu}$, assuming maximal θ_{23} mixing $\sin 2\theta_{23}$=1, which leads to $P_{e\mu} \sim P_{e\tau}$. Since the ν_μ to ν_e flux ratio, $r = \Phi_{\nu_\mu}/\Phi_{\nu_e} \sim 2$, the number of ν_e's that are added from $\nu_\mu \to \nu_e$ appearance is r$P_{\mu e} \sim 2P_{e\mu}$. If the T (CP) is conserved, $P_{e\mu} = P_{\mu e}$, the oscillation effect in observed atmospheric ν_e is cancelled and we would not be able to observe the oscillation as shown in Figure 37. This natural cancellation provides an opportunity for a sensitive tests for CP violation as well as maximal θ_{23} mixing.

The above simplified discussion ignores the matter effect, which enhances the oscillation effects, as described in Reference [35]:

$$P_{e\mu} = c_{23}^2|A_{e2}|^2 + s_{23}^2|A_{e3}|^2 + 2s_{23}c_{23}Re(e^{i\delta}A_{e2}^*A_{e3})$$
$$P_{e\tau} = s_{23}^2|A_{e2}|^2 + c_{23}^2|A_{e3}|^2 - 2s_{23}c_{23}Re(e^{i\delta}A_{e2}^*A_{e3}),$$

where A_{e2} and A_{e3} are the transition amplitudes to the mass eigenstates in the earth matter. For the maximal θ_{23} mixing or $s_{23}^2 = c_{23}^2 = 0.5$ and r=2, the oscillation effect for ν_e flux Φ_e compared to without oscillation Φ_e^0 becomes:

$$\Phi_e/\Phi_e^0 = r \times P_{\mu e} - P_{e\mu} - P_{e\tau} = 2P_{e\mu}(-\delta) - P_{e\mu} - P_{e\tau}$$
$$= Re(e^{i\delta}A_{e2}^*A_{e3}) = |A_{e2}A_{e3}|cos(\delta + \phi),$$

where we used the relation $P_{\mu e}(\delta) = P_{e\mu}(-\delta)$ and $\phi = arg(A_{e2}^*A_{e3})$. The oscillation effect is enhanced by the matter effect and is proportional to $cos(\delta + \phi)$.

Since the high energy muons above several GeV have more chance to reach the ground before decaying, the ratio r becomes significantly larger than 2 and the cancellation does not work anymore. This allows the study

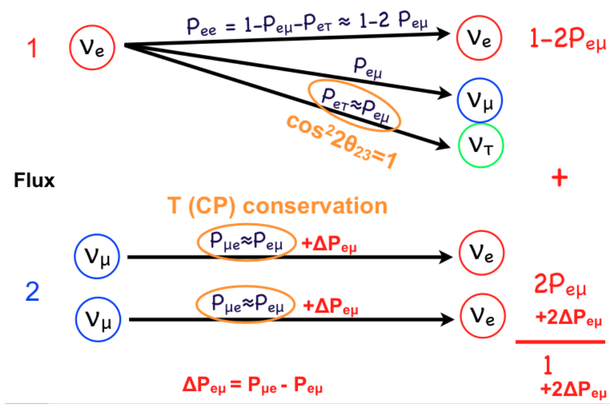

FIG. 37. Assuming that the atmospheric ν_μ and ν_e ratio is two, the maximum θ_{23} mixing ($\theta_{23} = 45^o$), and T(CP) conservation, the oscillation effect in ν_e observed spectrum is totally cancelled. If there is T(CP) violation (ΔCP), the observed ν_e spectrum would show the oscillation effect.

of the $\nu_\mu \to \nu_e$ matter oscillation resonance at several GeV to study the mass hierarchy.

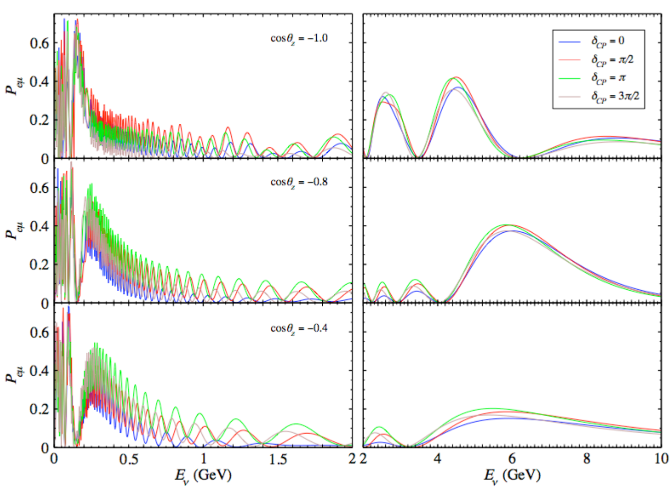

FIG. 38. $\nu_\mu \to \nu_e$ oscillation probability $P_\mu e$ as a function of neutrino energy E_ν for the zenith angle of $\cos_{zenith} = -1.0, -0.8, -0.4$ for the CP phase $\delta_{CP} = 0(blue), \pi/2(red), \pi(green), 3\pi/2(orange)$ [36]

Figure 38 shows the $\nu_\mu \to \nu_e$ appearance probability as a function of the neutrino energy for three typical zenith angles, $\cos_Z = -1.0, -0.8, -0.4$, where sub-GeV resonance effect is enhanced [36]. The sub-GeV and multi-GeV resonances come from the θ_{12} and θ_{23} matter effects, respectively. The colour of the curves corresponds to different CP phases. The blue curve, which is the smallest, represents δ_{CP}=0 case, and the other colour lines represents for different δ_{CP} values. The CP violation effect is as large as 20% in the sub-GeV neutrino energy range.

The zenith angle resolution, which is the correlation between the initial neutrino direction and the out-going lepton direction, starts to become measureable for the neutrino energies above E_ν=400-500MeV.

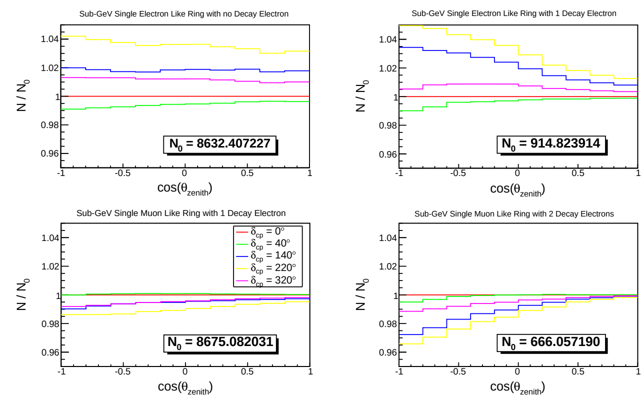

FIG. 39. Expected zenith angle distributions for sub-GeV electron-like with 0 and 1 decay electrons (top left and right) and μ-like events with 1 and 2 decay electrons (bottom left and right). The colour of the lines are for different CP violation phases.

Figure 39 shows the expected zenith angle distributions for the standard SK Monte Carlo for sub-GeV electron-like events with 0 and 1 decay electrons and μ-like events with 1 and 2 decay electrons. The colour of the lines are for different CP violation phases. As much as a several % CP violation effect is expected.

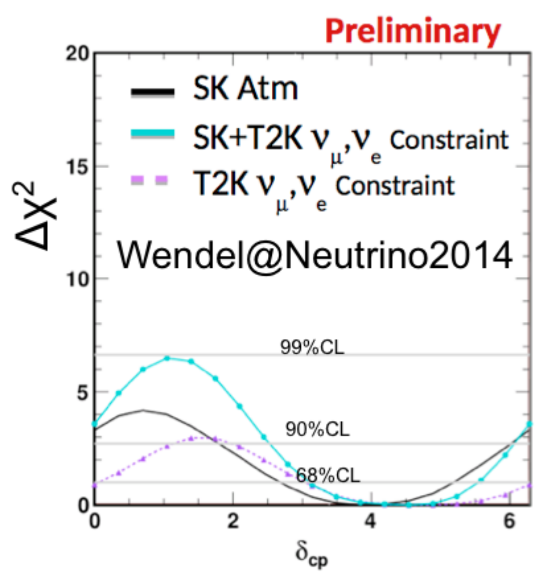

FIG. 40. Preliminary CP sensitivity of SK data along with T2K sensitivity presented at the Neutrino2014 conference.

Figure 40 shows the current preliminary CP sensitivity of SK data along with T2K sensitivity presented at the Neutrino2014 conference. The $\delta_{CP} = 0$ is disfavoured at Δ^2_χ of 3.5 or at 90%CL, which is better than T2K. On the other hand, the sensitivity is worse than T2K in rejecting $\delta_{CP} = \pi$. The $\delta_{CP} = \pi$ region can be explored by using antineutrinos which can be tagged by detecting neutrons with existing $np \to d\gamma$ trigger (Eff.=20%) or the planned Gd upgrade (GAZOOKS!), The antineutrino events provide better zenith angle measurements due to their strong forward scattering and thus enhance the signal sensitivity, although the statistical power is lower due to the smaller antineutrino interaction cross section.

The current SK CP sensitivity is limited by the systematic uncertainties on the atmospheric neutrino flux and cross section. Figure 41 shows the expected CP sensitivity to exclude $\delta_{CP} = 0$ for given $\delta_{CP} = 0$ when the systematic uncertainty is not considered. The black curve is with 50 bins in energy and zenith angle. The $\Delta\chi^2$ is more than 16 (4σ) at the best fit point and 13 (3.6σ) at $\delta_{CP} = -\pi/2$, which is the current best fit point. If we consider integrated date till 2020, the expected CP sensitivity exceeds 5σ at the best fit point and exceeds 4σ at $\delta_{CP} = -\pi/2$ for the statistical sensitivity. The red curve is zenith angle binning only and blue curve is energy binning only. Both energy and zenith angle contribute to the CP sensitivity. The likelihood to reject $\delta_{CP} = \pi$, which is also CP conserving, can be obtained by shifting the horizontal axis by π. There is little sensitivity for the current best fit point ($\delta_{CP} = -\pi/2$), which corresponds to $\delta_{CP} = \pi/2$ point in the figure.

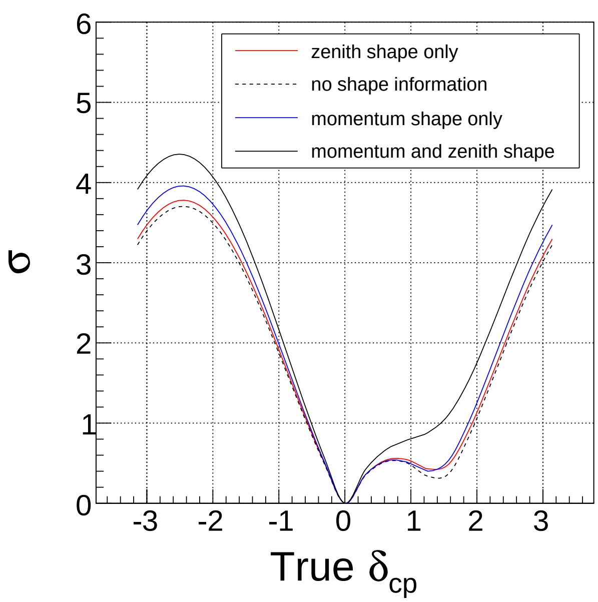

FIG. 41. CP sensitivity (σ) when only the statistical uncertainty is considered for the existing 5000-days of SK data set. The black curve is with 50 bins in energy and 50 bins in zenith angle and the black dashed line is normalization only (no binning). The red curve and blue curves are for only zenith angle or energy binning, respectively.

Atmospheric neutrinos provide wide range of baseline length, energy, and neutrino species. As seen above, sub-GeV atmospheric neutrinos have good statistical sensitivity even with the data already taken by SK. However, the atmospheric neutrino results are often limited by systematic uncertainties which are difficult to quantify.

The main systematic uncertainties in the atmospheric neutrino oscillation come from the atmospheric neutrino flux and neutrino cross sections. One effective way to reduce the systematic uncertainties is taking the ratio between ν_e and ν_μ candidates. The ν_e and ν_μ flux ratio prediction below a few GeV is almost independent of the flux models as they are originating from the same parent pions produced in the atmosphere. The main uncertainty comes from the charge asymmetry in pion production in the atmosphere which creates the ν_e and $\bar{\nu}_e$ asymmetry. The systematic uncertainty is estimated to be about 5% in an earlier study [37]. The cross section systematics come from the difference between the ν_e and ν_μ interaction cross sections, which are in the first order the same at a few % level. The difference comes from the phase space difference due to electron and muon mass difference and the radiative corrections and possible other unknown effects. This can be addressed by NuPRISM as discussed below. To match the statistical uncertainty of 1% (∼10,000events) to perform the precision CP measurement, further reduction in systematic uncertainties is essential.

The neutrino flux uncertainty comes from the primary cosmic ray flux and the hadron production in the atmosphere. Recently, there has been a big progress towards understanding the atmospheric neutrino flux. The new AMS result [38] announced in April 2015 provides a very precise measurement of the primary cosmic ray flux at a wide range of energies with a systematic uncertainty of 1-2% making this component to the systematic uncertainty to ν_e and ν_μ flux ratio negligible. The CERN NA61 experiment developed a very precise measurement of hadron production at the 5% level which greatly improved the systematic uncertainty of the neutrino flux for the T2K long baseline neutrino experiment [16]. However, the current CERN SPS beamline used by NA61 is capable of delivering the beam above 15 GeV/c, and there remains large systematic uncertainty (tens of %) in hadron production cross section below 15 GeV/c which is the main source of atmospheric neutrino flux uncertainty. A discussion is taking place with NA61 group to modify the SPS beamline to study hadron production in the primary proton energy of 1-15 GeV/c in NA61 for the atmospheric neutrino studies as well as T2K and other long baseline experiments.

For the neutrino cross section, the critical measurement is the cross section difference between ν_e and ν_μ. NuPRISM will improve this as discussed in a previous section. It is also important to study the differential cross section in lepton direction and energy, as the dependence of these variables improves the sensitivity significantly as shown in Figure 41.

With a new hadron production measurements considered by NA61 and the sub-GeV neutrino cross section measurement by NuPRISM, along with the recent very precise AMS primary cosmic ray measurement, precise atmospheric neutrino oscillation study including CP violation would be possible using the existing SK data set.

J. $\bar{\nu}_\mu$ Measurements

In principle, the NuPRISM technique of using multiple off axis angles to measure the oscillated p_μ and θ_μ for each oscillated flux will work for anti-neutrinos as well. However, when running the T2K beam in anti-neutrino mode, there is a significant wrong-sign background from neutrino interactions. To disentangle these neutrino and anti-neutrino interactions, linear combinations of the neutrino-mode data can be used to construct the wrong-sign flux in anti-neutrino mode, analogous to the procedure used in Section III F to construct the Super-K oscillated spectra and in Section III G 1 to construct the electron neutrino spectrum. Hence, the neutrino flux in the anti-neutrino mode is described with the linear combination of neutrino mode fluxes:

$$\Phi^{\bar{\nu}mode}_{\nu_\mu}(E_\nu, \theta_{oa}) = \sum c_i(\theta_{oa}) \Phi^{i,\nu mode}_{\nu_\mu}(E_\nu). \qquad (7)$$

$\Phi^{\bar{\nu}mode}_{\nu_\mu}(E_\nu, \theta_{oa})$ is the anti-neutrino mode ν_μ (wrong-sign) flux for a given off-axis angle θ_{oa}. $\Phi^{i,\nu mode}_{\nu_\mu}(E_\nu)$ is the neutrino mode ν_μ (right-sign) flux for the i^{th} off-axis bin and c_i is the weight for the i^{th} off-axis bin that depends on the off-axis angle for which the anti-neutrino mode wrong sign flux is being modeled.

Linear combinations to reproduce the wrong-sign $1.0-2.0°$, $2.0-3.0°$ and $3.0-4.0°$ anti-neutrino mode fluxes are shown in Figure 42. As with the combinations to produce the ν_e flux, the agreement is good up to about 1.5 GeV in neutrino energy. As discussed in Section III G 1, it is less important to reproduce the high energy part of the flux since high energy interactions are suppressed by the event topology selected and the muon acceptance of NuPRISM.

As shown Figure 43, there is significant correlation between the wrong-sign neutrino flux in anti-neutrino mode and the neutrino-mode flux, so the flux uncertainties will give some cancelation using this method. After subtracting the neutrino background, the remaining $\bar{\nu}_\mu$ events can then be combined as in the neutrino case to produce oscillated spectra at Super-K.

K. Gd doping in NuPRISM

In 2015, the Super-K collaboration approved the plan to load the Super-K detector with 0.2% gadolinium sulfate, $Gd_2(SO_4)_3$ to enhance the neutron detection capability. Gadolinium, Gd, has a thermal neutron capture cross-section of 49,000 barns, 5 orders of magnitude larger than the capture cross-section on free protons. The neutron capture time for 0.1% Gd loading has been measured to be 28 μs [17]. The Gd-capture produces an 8 MeV gamma cascade which is detectable in NuPRISM.

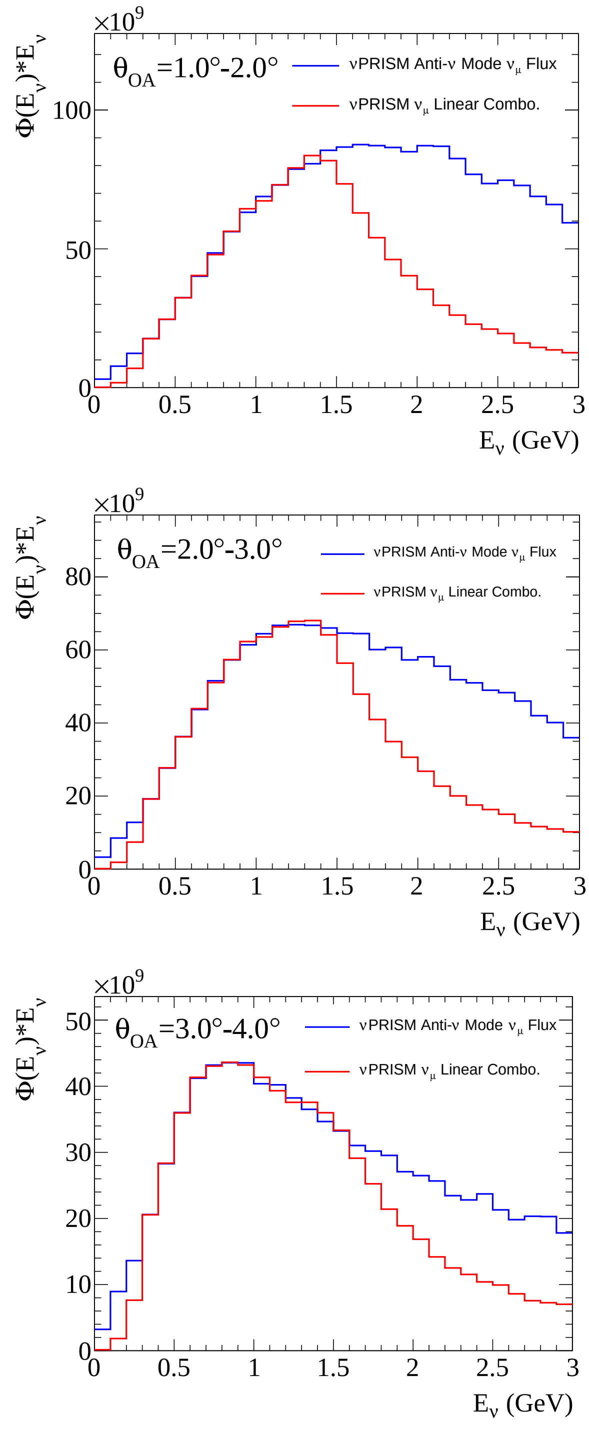

FIG. 42. The NuPRISM anti-neutrino mode wrong-sign ν_μ fluxes for $1.0-2.0°$ (top), $2.0-3.0°$ (middle) and $3.0-4.0°$ (bottom), and the NuPRISM linear combinations of neutrino mode ν_μ fluxes.

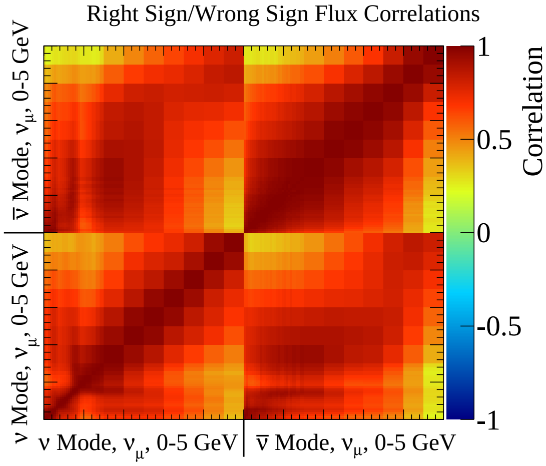

FIG. 43. The correlations between the flux normalization parameters for energy bins from 0 to 5 GeV for the neutrino mode and anti-neutrino mode ν_μ fluxes.

The detection of neutron captures on Gd can be used to improve the sensitivities of measurements made at $\mathcal{O}(1\ GeV)$ energies. Proton decays are expected to produce a final state neutron less than 10% of the time [18], while atmospheric neutrino interactions have on average 1 or more final state neutrinos (depending on the energy) [19]. The detection of final state neutrons can be used to reduced the atmospheric neutrino background for proton decay searches. Among the atmospheric neutrino interactions, the final state neutron multiplicity is expected to vary depending on whether a neutrino or antineutrino interacts, and whether the interaction is quasi-elastic or inelastic. In the absence of final state and secondary interactions in the detector, the quasi-elastic scattering of a neutrino will produce no neutrons, while the quasi-elastic scattering of an antineutrino will produce a neutron. The presence of final state and secondary interactions will smear these distributions, but a statistical separation of neutrino and antineutrino interactions will be possible. The same neutron tagging can be applied to accelerator neutrino samples to reduce the wrong-sign contamination arising of neutrino (antineutrino) contamination in the antineutrino (neutrino) beam mode.

The application of neutron detection in the proton decay, atmospheric and accelerator neutrino measurements requires accurate knowledge of final state neutron multiplicities for $\mathcal{O}(1\ GeV)$ neutrino interactions. By loading NuPRISM with $Gd_2(SO_4)_3$, the neutron multiplicities can be measured in the NuPRISM detector using the accelerator produced neutrino interactions. The capability to load NuPRISM with Gd has been described in Section III.H.1 of the NuPRISM proposal. The primary challenge for Gd loading is containment of the Gd loaded water to avoid leaking into the local environment. For containment, a water tight instrumented detector tank is being considered. The determination of the NuPRISM site location is a critical input for the tank design since the size of the instrumented region will depend on the baseline from the neutrino source to NuPRISM.

The backgrounds for neutron detection in NuPRISM have been considered. The dominant background is neutrons that are produced in the outer detector (OD) or surrounding rock from interactions of beam neutrinos. These neutrons coincide with the beam timing, so they cannot be reduced by a timing cut around the beam spill arrival time. The simulated rate of entering neutrons is described in Section II.D.2 of the NuPRISM proposal. The entering neutron rate is estimated with a GEANT4 simulation of the NuPRISM water column and the surrounding rock with neutrino interactions simulated by NEUT 5.1.4.2. The simulation results presented in the proposal assume a 1 km baseline to NuPRISM and 1.6×10^{14} protons per spill. The current accelerator performance projection is for 3.2×10^{14} protons per spill after 2025, hence the simulation has been updated for twice the protons per spill. The potential of an OD veto to select events with a reduced number of entering neutrons has also been investigated. Table VII shows the rates of neutrons entering the inner detector (ID) for 320 kA horn currents at three different off-axis positions. In the most on-axis position the average neutron rate is 3.89 events for a 4 m radius ID and 2.28 for a 3 m radius ID. The entering neutron rate can be reduced by 27% and 36% respectively by only selecting spills with less than 6 visible interactions in the OD. The background may also be reduced by applying a tight fiducial cut on the reconstructed neutron vertex to exclude neutron captures near the detector wall. Since neutrons produced in a neutrino interaction will typically capture within 1-1.5 m of the primary neutrino interaction, the background can be further reduced by selecting neutron captures near the neutrino interaction vertex, excluding most entering neutrons which will have reconstructed vertices near the detector wall. In the further off-axis positions the entering neutron rate is reduced and a tighter OD veto is required to reduce the entering neutron rate. After OD and vertex position cuts the remaining neutron background can be directly measured in spills with no ID interactions, and a statistical subtraction can be applied to the neutron multiplicity measurements. It is expected that the entering neutron rate at 1 km is low enough to perform neutron multiplicity measurements, however given the uncertainties associated with neutron production and low energy neutron scattering, the rate of neutrons produced in the rock should be measured with a dedicated experiment after NuPRISM achieves Stage 1 approval.

The number of charged current ν_μ candidate events expected in NuPRISM for the T2K-II exposure is 2×10^6, 1×10^6 and 4×10^5 for the 1.0-2.0°, 2.0-3.0° and 3.0-4.0° off-axis angle positions respectively. Given these large sample sizes, precision measurements of the neutron multiplicities will be possible, even with tight cuts on the OD activity and vertex position. For given four-momentum

TABLE VII. The entering neutron rates per 3.2×10^{14} protons on target for NuPRISM with horn currents at 320 kA.

	No OD Veto		< 6 OD Interactions	
Off-axis Angle (°)	ID r=4 m	ID r=3 m	ID r=4 m	ID r=3 m
1.0-1.6	3.89	2.28	2.84	1.46
2.0-2.6	1.26	0.70	1.26	0.70
3.0-3.6	0.48	0.28	0.48	0.28

transfers, the neutron multiplicities for ν_μ and ν_e interactions are expected to be the same, so the ν_e neutron multiplicity rates can be constrained with the ν_μ candidate data.

NuPRISM can perform unique measurements of the neutron multiplicities that are not possible in other experiments. As illustrated in Fig. 44, the three momentum and energy transfer can be reconstructed for NuPRISM mono-chromatic beams, or the energy can be reconstructed using the quasi-elastic formula, and quasi-elastic and non-quasi-elastic events can be separated kinematically. By measuring the neutron multiplicity as a function of three momentum and energy transfer, the NuPRISM measurements can be applied to different neutrino energies, including higher energy interactions in the SK atmospheric sample. By kinematically separating the quasi-elastic and non-quasi-elastic events, NuPRISM can measure neutron multiplicities for both event types. Any differences can be used to statistically separate quasi-elastic and non-quasi-elastic types in Super-K, improving the reconstructed energy resolution for atmospheric neutrino and accelerator neutrino measurements.

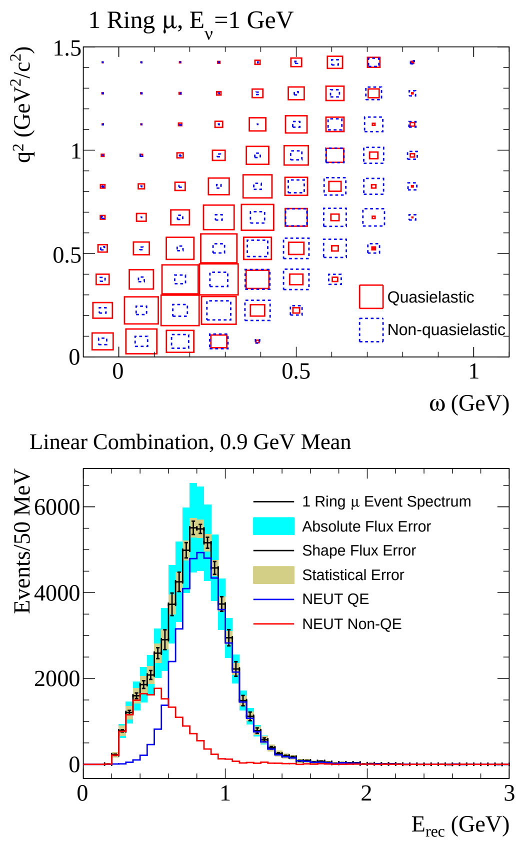

FIG. 44. The distribution of reconstructed three momentum and energy transfer for a 1 GeV mono-chromatic beam in NuPRISM (left) and the distribution of reconstructed energy for a 0.9 GeV mono-chromatic beam in NuPRISM (right).

L. Cross Section Measurements

A unique feature of NuPRISM is the ability to measure the true neutrino energy dependence of both CC and NC interactions using nearly monoenergetic beams. These measurements are expected to significantly enhance the reach of oscillation experiments, since the energy dependence of signal and background processes must be understood in order to place strong constraints on oscillation parameters. As explained in Section III F, additional multinucleon processes, with a different energy dependences than the currently modeled CCQE and CC1π cross sections can affect the T2K oscillation analysis. In the current disappearance analysis, there are also substantial uncertainties on NC1π^+ and NC1π^0 processes (for disappearance and appearance respectively). As a result, future proposed experiments which use water as a target (e.g. Hyper-Kamiokande and CHIPS) will directly benefit from the NuPRISM cross section program; other programs benefit less directly through a critical validation of our assumptions of the energy dependence of the cross section on oxygen. It is also not just long baseline oscillation programs which benefit, as cross section processes at T2K's flux peak are also relevant for proton decay searches and atmospheric neutrino oscillation analyses. Finally, should T2K run an antineutrino beam during NuPRISM operation, all arguments made above equally apply for antineutrino cross section measurements at NuPRISM.

One should also consider the study of neutrino interactions interesting in its own right as a particle/nuclear theory problem. As an example, MiniBooNE's cross section measurements have received much attention from the nuclear theory community who predominantly study electron scattering data.

Some of the difficulties in improving our understanding of neutrino cross sections stems from the fact that we do not know, for a given interaction, the incident neutrino energy. Any given measurement is always averaged over the entire flux. The observed rate N in a given observable bin k depends on the convolution of the cross section, σ, and the flux, Φ:

$$N^k = \epsilon_k \int \sigma(E_\nu)\Phi(E_\nu)dE_\nu, \tag{8}$$

where ϵ is the efficiency. Therefore, our understanding of the energy dependence of neutrino interaction for a particular experiment is limited by the flux width and shape. One then attempts to use different neutrino fluxes (with different peak energies) to try to understand the cross section energy dependence. As discussed later in this section, for CC interactions we have many examples of disagreements between experiments, and for NC, we have a limited number of measurements made, and the lack of information and conflicting information leaves unresolved questions about the true energy dependence of the cross section.

In addition to providing new measurements on oxygen, there are two main advantages of NuPRISM over the current paradigm. First, we can directly infer the energy dependence of the cross section by combining measurements at different off-axis angles into a single measurement, as if we would have had a Gaussian neutrino flux source. Second, and equally important, we can fully understand the correlations between energy bins, in a way not possible previously when comparing across experiments with entirely different flux setups.

In CC interactions, previous experiments use the muon and hadronic system to try to infer the neutrino energy dependence. NuPRISM has the capability to directly test if the neutrino energy dependence inferred from the lepton information is consistent with the energy information determined from the off-axis angle. NuPRISM will also for the first time probe the energy dependence of NC cross sections within a single experiment.

Furthermore, there is no data for the kinematic information of pions out of NCπ^+ interactions. However, NCπ^+ is one of the backgrounds in the current T2K $1R_\mu$-like selection used for the disappearance analysis. A direct measurement of NCπ^+, and a measurement of the pion momentum and angular distributions would reduce the substantial uncertainties on this process (in both cross section and detector efficiency) in the analysis.

Oxygen is an interesting target material for studying cross sections because few measurements exist and it is a medium sized nucleus where the cross section is calculable. NuPRISM will provide differential measurements in muon and final state pion kinematic bins. While these kinds of measurements will be done with the ND280 P0D and FGD2 detectors in the near term, NuPRISM will have more angular acceptance than those measurements and so enhances the T2K physics program.

Possible cross section measurements, based on observable final state topologies, at NuPRISM include:

- CC inclusive
- CC0π
- CC1π^+, π^0 (resonant and coherent)
- NC1π^+, π^0 (resonant and coherent)
- NC1γ

TABLE VIII. Expected number of events in the fiducial volume of NuPRISM for 4.5×10^{20} POT, separated by true interaction mode in NEUT.

Int. mode	1-2°	2-3°	3-4°
CC inclusive	1105454	490035	210408
CCQE	505275	271299	128198
CC1π^+	312997	111410	39942
CC1π^0	66344	23399	8495
CC Coh	29258	12027	4857
NC 1π^0	86741	32958	12304
NC 1π^+	31796	11938	4588
NC Coh	18500	8353	3523

The above list is based on expected water Cherenkov detector capabilities from experience with MiniBooNE, K2K 1 kton and Super-Kamiokande (SK) analyses. All CC measurements can be done for ν_μ and ν_e flavors due to the excellent e-μ separation at NuPRISM. Antineutrino cross section measurements are also possible with similar selections. A brief summary of each measurement follows. Table VIII shows the number of events in the FV of NuPRISM, broken down by interaction mode.

1. *CC Inclusive*

Inclusive measurements are valuable because they are the most readily comparable to electron scattering measurements and theory, as there is minimal dependance on the hadronic final state. Also, external CC inclusive neutrino data was used in the estimation of the T2K neutrino oscillation analyses to help determine the CCDIS and CC multi-π uncertainties.

The CC ν_μ cross section has been measured on carbon by the T2K [39] and SciBooNE [40] experiments. MINERvA has produced ratios of the CC inclusive cross section on different targets (C,Fe,Pb) to scintillator [41]. In addition, the SciBooNE results include the energy dependence of the CC inclusive cross section from the muon kinematic information. The CC ν_e cross section on carbon is in preparation by T2K.

NuPRISM should be able to select CC ν_μ and ν_e events with high efficiency and produce a CC inclusive measurement vs. true neutrino energy on water. Using the latest T2K simulation tools, we estimate a CC inclusive ν_μ (ν_e) selection to be 93.7% (50.4%) efficient relative to FCFV and 95.9% (39.5%) pure based on observable final state. The low purity of the ν_e selection is predominantly due to the small ν_e flux relative to ν_μ.

2. CC0π

The CCQE ν_μ cross section has been measured on carbon by MiniBooNE [9] and is consistent with a larger cross section than expected which could correspond to an increased value of an effective axial mass (M_A) over expectation; SciBooNE's analysis was presented at NuInt2011 [42] but not published and is consistent with MiniBooNE. In addition, a measurement by NOMAD [43] done at higher neutrino energies which is in agreement with MiniBooNE and SciBooNE. This is shown in Figure 45, along with the recent T2K ND280 Tracker analysis results. An indirect measurement of the cross section was done with the K2K near detectors, where a higher than expected value of the QE axial mass, M_A, was also reported [45]. There are also recent results from MINERvA [44].

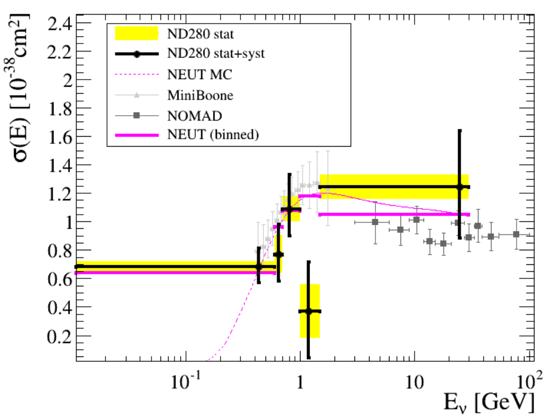

FIG. 45. The CCQE cross section as predicted by NEUT (pink dashed) vs. true neutrino energy. Also overlaid are results from MiniBooNE, NOMAD and T2K.

MiniBooNE's selection was CC0π, that is 1 muon and no pions in the final state, and was 77.0% pure and 26.6% efficient; the 1R_μ-like selection at SK is 91.7% pure and 93.2% efficient, based on observable final state. It is postulated that the MiniBooNE selection, but not the NOMAD one, is sensitive to multinucleon processes, where a neutrino interacts on a correlated pair of nucleons and that this resulted in the higher cross section reported by MiniBooNE. However, the two experiments have very different flux, selection and background predictions and systematics.

By measuring the CC0π cross section at different vertex points in NuPRISM, we should be able to infer the different energy dependence and constrain multinucleon and CC1π^+ pionless Δ decay (PDD) processes. This can be seen in Figure 7, which shows the momentum of CCQE and MEC (Nieves' npnh) events for a particular angular range (0.85 $<\cos(\theta)<$ 0.90) generated according to the T2K flux, and for a 1 GeV NuPRISM flux. MiniBooNE and T2K have difficulty separating the MEC component of the CCQE cross section due to the shape of their neutrino energy spectra, but the NuPRISM detector would give us additional information to separate out that component and characterize it, as demonstrated in Figure 7. Even though NuPRISM is not a measurement on carbon, oxygen is of a similar density to carbon and so will be helpful in understanding the difference between the MiniBooNE and NOMAD results if it is indeed due to MEC.

3. CC1π^+ and CC1π^0

The CC1π^+ and CC1π^0 cross sections have been measured on carbon by MiniBooNE [46],[47]; K2K also produced measurements CC1π^+ [48] and CC1π^0 [49] with the SciBar detector. One may infer the coherent contribution to the CC1π cross section from the angular distribution of the pion; this was done by K2K [50] and SciBooNE. Improvements to the SK reconstruction could yield a similar efficiency and purity to the the MiniBooNE selections for CC1π^+ (12.7%, 90.0%) and CC1π^0 (6.4%, 57.0%) based on observable final state.

The CC1π resonant cross section for the T2K flux is dominated by contributions from the Δ resonance [51], so NuPRISM would provide clear information about the NΔ coupling and form factors. We can also compare the pion momentum produced out of CC1π^+ interactions for different neutrino energies in order to better understand how final state interactions affect pion kinematics.

4. NC1π^+ and NC1π^0

The NC1π^0 cross section has been measured on carbon by MiniBooNE [52] (36% efficient, 73% pure) and SciBooNE. A measurement of the ratio of NC1π^0 to the CCQE cross section has been done water by the K2K 1kton near detector [53]. The efficiency and purity of the K2K selection is 47% and 71% respectively. A measurement of NCπ^+ exists [55] on a complicated target material ($C_3H_8CF_3Br$) but has no differential kinematic information. Figure 46 shows this measurement with a prediction from the NUANCE neutrino event generator.

A measurement of NCπ^+ will be challenging but possible at NuPRISM. T2K already has developed an "NC" enhanced selection for Super-K that is 24% NCπ^+, 14% NC1proton, and 55% CCν_μ, by interaction mode. Recent developments in event reconstruction at Super-K include a dedicated pion ring finder, which should make possible a more pure selection of NCπ^+ from which the pion momentum and angular distribution can also be measured. Since NuPRISM will allow for a first measurement of the energy dependence of the NC channels and like the CC channels, it will be particularly interesting to measure the outgoing pion spectra of these events in order to probe nuclear final state interactions.

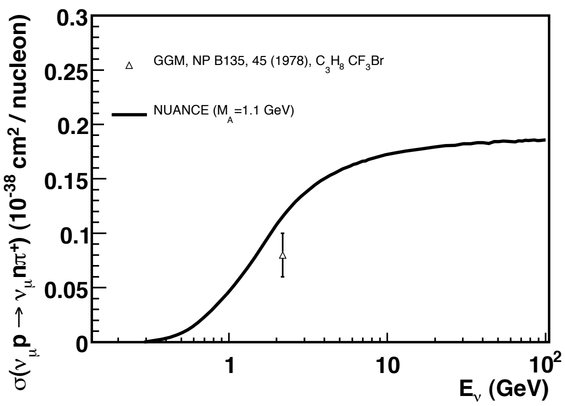

FIG. 46. The NCπ^+ cross section as predicted by NUANCE vs. true neutrino energy overlaid with the only measurement (on $C_3H_8CF_3Br$). Figure from Ref. [54]

To summarize, NuPRISM's measurement of true neutrino energy dependence of the cross section is a unique and potentially critical input to our overall understanding of cross section processes around 1 GeV neutrino energy. In particular, NuPRISM will help us understand for CC0π events, if the shape and size of the PDD and mulitnucleon components are modeled correctly. Furthermore, NuPRISM can provide new information on the pion kinematics out of NC interactions relevant to the oscillation analysis and the energy dependence of those cross sections.

IV. DETECTOR DESIGN AND HARDWARE

The NuPRISM detector uses the same water Cherenkov detection technology as Super-K with a cylindrical water volume that is taller than Super-K (50-100m vs 41m) but with a much smaller diameter (6-10m vs 39m). The key requirements are that the detector span the necessary off-axis range (1°-4°) and that the diameter is large enough to contain the maximum required muon momentum. The baseline design considers a detector location that is 1 km downstream of the neutrino interaction target with a maximum contained muon momentum of 1 GeV/c. This corresponds to a 50 m tall tank with a 6 m diameter inner detector (ID) and a 10 m diameter outer detector (OD), as shown in Figure 47. A larger, 8 m ID is also being considered at the expense of some OD volume in the downstream portion of the tank. As the NuPRISM analysis studies mature, the exact detector dimensions will be refined to ensure sufficient muon momentum, ν_e statistics and purity, etc.

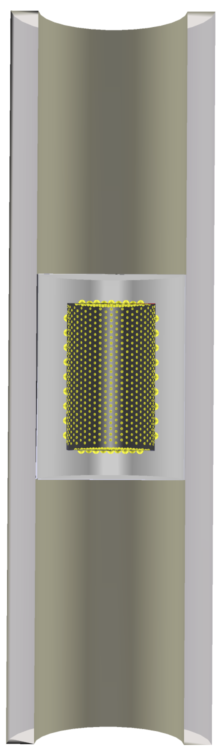

FIG. 47. The planned configuration of the nuPRISM detector within the water tank is shown. The instrumented portion of the tank moves vertically to sample different off-axis angle regions.

The instrumented portion of the tank is a subset of the full height of the water volume, currently assumed to be 10 m for the ID and 14 m for the OD. The novel feature of this detector is the ability to raise and lower the instrumented section of the tank in order to span the full off-axis range in 6 steps. The inner detector will be instrumented with either 5-inch or 8-inch PMTs to ensure sufficient measurement granularity for the shorter light propagation distances relative to Super-K. Also under consideration is to replace the OD reflectors with large SMRD-style scintillator panels, as discussed in Section IV E.

The remainder of this section describes the elements needed for NuPRISM and corresponding cost estimates, where available. The cost drivers for the experiment are the civil construction and the cost of the PMTs, and, correspondingly, more detailed cost information is presented in those sections.

A. Site Selection

The NuPRISM detector location is determined by several factors, such as signal statistics, accidental pile-up rates, cost of digging the pit, and potential sites available. At 2.5^o off-axis position at 1 km with a fiducial volume size of 4 m diameter and 8 m high cylinder, the neutrino event rate at NuPRISM is more than 300 times that of SK. At 2km, the number of events drops by a factor of 4, which yields 75 times more events than SK, for the same size of the detector. The impact of the number of events collected on the physics sensitivities is described in Section III. The event pile-up is dominated by sand muons, but at 1 km, the pile-up rate appears to be acceptable, which is explained in more detail in Section III, The detector size and the depth scales with the distance to the NuPRISM detector. In order to cover from 1-4° off-axis angles, the depth of the detector is 50m at 1km and 100m at 2km. There are standard Caisson approach available the pit depth of up to 65m and diameter of up to 12m. For deeper depth or larger diameter, more specialized construction may be required, and could increase the cost per cubic meter of excavation dramatically.

The two far detector sites that must be considered are the Mozumi mine, where Super-K is located, and Tochibora, which is a candidate site for Hyper-K. There are four potential unused sites in the Tochibora and Mozumi directions, not including rice fields, a shown in Figure 48:

- 750m site near the Muramatsu community meeting centre: This location is right next to R245 and owned by the local government. The space is limited but covers the Mozumi direction and the central line between Mozumi and Tochibora. This site would have the highest event pile-up rate.
- 1km site: a large un-cultivated private land covering both Tochibora and Mozumi directions
- 1.2km site: a large patch of private land at the foot of a forest covering both Tochibora and Mozumi directions
- 1.8km site: the originally considered 2km detector site owned by the local government covering Tochi-

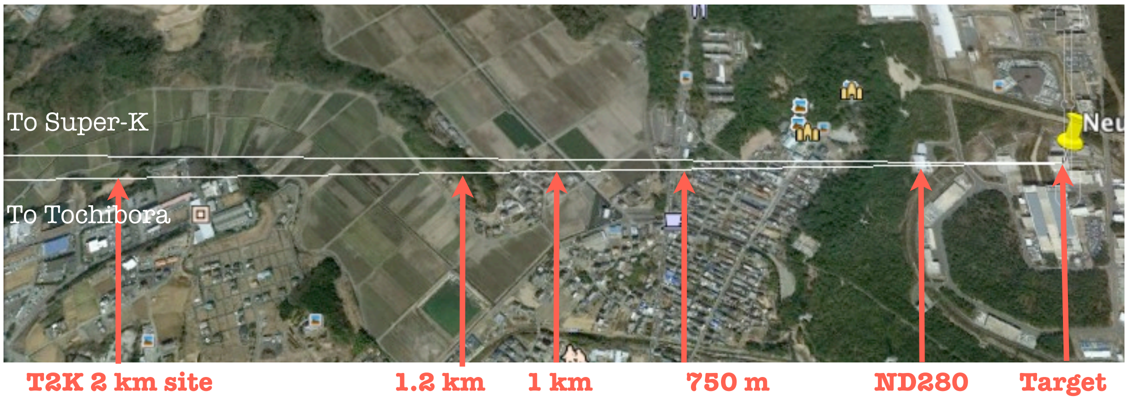

FIG. 48. Potential sites are shown for NuPRISM if all rice field locations are excluded.

bora direction. This site would have the deepest detector, 90m deep.

If the rice field can be available, there are a lot more choices. At the time of the 2km detector site study, rice fields were also considered, although not selected in the end. Changing the land use for the rice field would require additional approval process, if it were possible. The process of land use require consensus from the local community and the strong involvement of the host institution. There are facilities that are operated just outside J-PARC, the KEK-Tokai dormitory, KEK Tokai #1 building at IQBRC, and the dormitory of the Material Science Institute of Tokyo university about hundred meter north of IQBRC.

B. Civil Construction

Based on the current baseline design of the NuPRISM detector described previous sections, we have communicated with companies for the preliminary cost estimation of NuPRISM civil construction; the water tank construction and detector construction. The NuPRISM detector is also considered as a prototype detector of Hyper-Kamiokande (Hyper-K) for testing new photo-sensors, readout electronics, and the water containment system design.

Two groups have been contacted to provide preliminary cost estimates for the civil construction associated with fabricating a 50 m deep cylindrical volume with a 10 m diameter. The first group consists of a general construction company and a heavy industrial company currently providing cost estimates for Hyper-K. The second group is a single general construction company that was associated with the cost estimates from the original T2K 2 km detector proposal [57].

There are several techniques to construct the 10 mϕ and 50 m long vertical "tunnel"; Pneumatic Caisson (PC) method, Soil Mixing Wall (SMW) method, New Austrian Tunneling (NAT) method, Urban Ring (UR) method. Each of the construction methods have pros and cons, and some of the methods are not applicable depending on the actual geological condition. Cost estimates from both construction groups are given in the appendix.

C. Liner and Tank

The NuPRISM detector can be used for proof-testing various designs and components which will be adopted in the Hyper-K detector. The NuPRISM water tank will have the same liner structure as that designed for Hyper-K.

The structure of the NuPRISM tank liner is shown in Figure 49. The innermost layer contacting with the tank water must be a water-proofing component to seal the water within the tank. We use High-Density Polyethylene (HDPE) sheets, which are commonly used as a water-proofing tank liner material. The sheets have extremely low water permeability and also are resistant to long-term damages from the ultra pure water. The adjoining sheets are heat-welded, and the welded part also keeps the water-proof functionality.

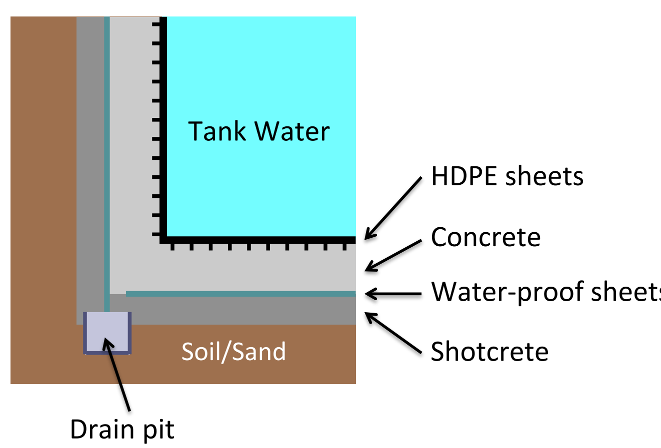

FIG. 49. A schematic view of the NuPRISM tank liner.

We select the HDPE sheet with a number of studs protruding from one side. These studs work for anchoring the sheet firmly on the backside concrete layer. To build this "HDPE on concrete" liner, a HDPE sheet is fastened to the inside of a concrete form beforehand, then the concrete is poured into the form for making the backfill concrete layer. While the thickness of the HDPE liner is 5-10mm, the thickness of the backfill concrete layer is yet to be determined.

Though we aim to construct the HDPE sheet liner such that the tank water can not leak, an additional waterproof layer is made between the backfill concrete layer and the shotcrete. This layer works as a catcher and a guide for the water by the unexpected leakage through the HDPE liner (and also the sump water through the shotcrete). This leaked water is drained via pits placed under the water tank.

D. Detector Frame and Lifting Mechanism

This section describes a proposed design for the frame that supports the NuPRISM PMTs and defines both the inner and outer detector. We will also describe the system by which this frame can be moved up and down in order to be able to make the NuPRISM measurements. Attention will be paid to the question of providing adequate water flow through the NuPRISM frame while maintaining optical separation.

1. Detector Shape, Support and Positioning

Figure 50 shows a simple cylindrical design, the walls of the Inner Detector (ID) being 0.5 meters thick. The half circles represent the 20" PMTs (0.5m) facing outward for the veto region (OD). The smaller half circles represent 8" PMTs (0.2m) facing inwards to the ID region. The 0.5m thickness of the detector wall is to contain the bodies of the PMTs (and PMT electronis) and, with internal stiffening braces, be stiff enough to accurately position the PMTs and not deform significantly under the weights and buoyancies.

Figure 50 also shows a conceptual support and positioning system. The detector is positioned on four vertical rails fixed to the shaft walls, and supported on top and bottom rings. Struts connect the detector to these two rings. The struts are positioned at the corners of the detector where the structure is strongest, and angled so that the distance from the detector to the start of the reflector is 1.7m top and bottom, and 1.5m on the sides. The reflector encloses the OD region and is required to be optically isolated from the ID volume, and from the shaft water volumes above and below. We discuss the reflector in more detail below.

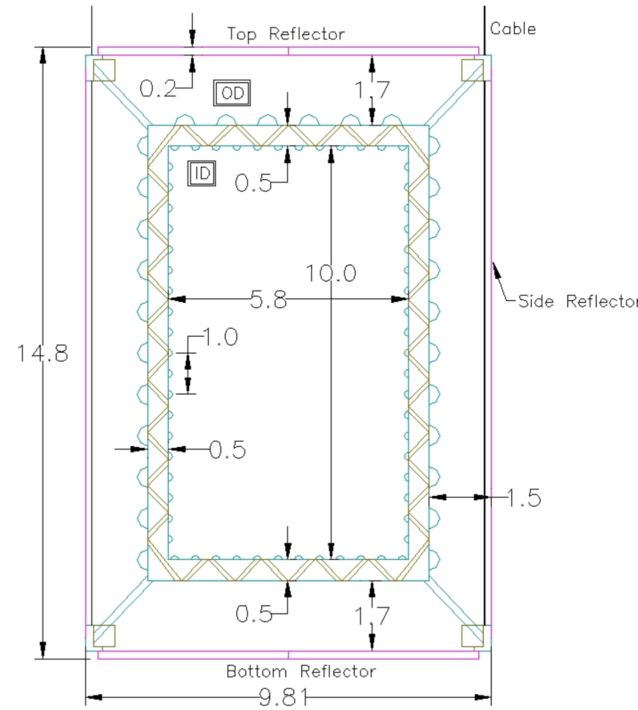

FIG. 50. The Detector is positioned on four rails inside shaft, and supported on top and bottom rings. Struts connect the detector to its rings. Four vertical cables support the assembly. Ballast can be added to the rings, if required. Distances are in meters.

2. Water Flow and Optical Isolations

Figure 51 shows views of the top-left corner of the detector and reflector. Two section views indicate the conceptual features and functions involved. The volume of the ID and OD are $\approx$264m^3 and $\approx$790m^3, respectively, with a combined volume of $\approx$1,190m^3 (including all wall volumes). If the apparatus is to traverse the shaft limits in $\approx$24 hours, the speed would be $\approx$1.5 meters/hour. Since the reflector side walls are close to the shaft, the displaced water needs to flow through the reflectors. This speed corresponds to a water flow of $\approx$118 m^3/hour = 2.0 m^3/min. Even if the water could flow past the sides of the reflector enclosure, 1,190 tons of water would also be in motion, which would be difficult to accommodate. With no water flowing through the sides of the reflector enclosure, the sides can be simple metal panels with a white inner surface to enhance the OD light collection. As indicated in Figure 51, these vertical reflector walls need to notch around the four rails and the associated couplings on the rings, and would be screwed to the top/bottom rings. With a height of 13.8m and circumference of 33.5m, it will need to be segmented with overlapping joints (or added joint strips). When the detector is out of the water, it would be useful to be able to easily remove the side reflector segments. Minimal segmentation would be four, with joints at the center of the 'notches'. This would allow the segments to slid out past the rails and the support towers. The top and bottom reflectors are also bolted to the top/bottom rings, but they have to be thicker to allow them to be strong and stiff due to the quantity of water flowing through them. The stiffness is achieved by making the top/bottom reflectors 0.2m thick and them having an internal bracing structure. The top/bottom reflectors need an optical seal to the rest of the shaft, yet allow ≈2.0 tons/min of water to flow through. Figure 51, shows two possible solutions:

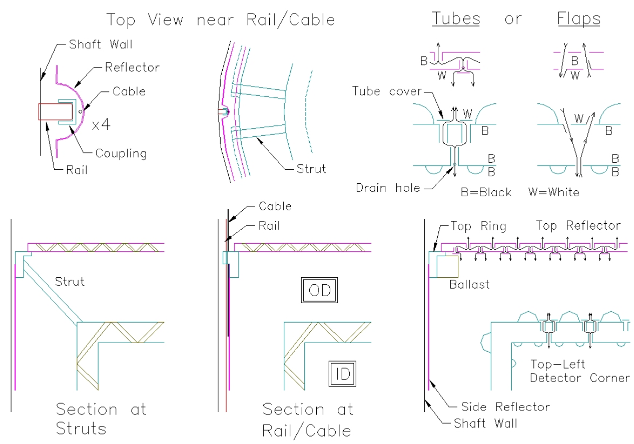

FIG. 51. This shows views of the top-left corner of the detector and reflector. Two sections views indicate the conceptual features and functions involved. A system of offset black pipes (or flaps) would allow water to flow through.

1. The first is a system of offset black pipes, so that water can flow through, but any light would need at least two reflections off black surfaces. The inner surface of the top/bottom reflectors would be white to enhance light collection. The tubes at the inner surface would have white 'tube covers'. This is easily done by having the tube extend, with the tube cover fixed to it, but the tube having four side large slots, leaving webs of material to hold the cover. The cover and outer surface of tube extension would be white. To prevent water being trapped in the reflector wall when the detector is lifted out of the water, there would be 'Drain holes' in the tubes, just inside the inner wall. Alternately, there could be some small drain tubes+covers extending slightly into OD volume. This scheme is a little complicated, but has the advantage of no moving parts. If the flow is fully distributed over the 55.0 m^2 area, the movement water flow would then be ≈36 liters/minute/m^2.

2. Another way solve this problem would to have a system of flaps that open only when the detector is moved, and close automatically when it stops. Half the flaps open when the detector moves down (water moves up), these flaps close under their own weight when movement stops. The other flaps open when the detector moves up (water down), these 'down' flaps would need to be spring loaded or counterweighted to close when movement stops. In Figure 51, we show both these flaps in the open position. The inner surfaces of the flaps would be white. In this scheme most of the water would drain through the spring loaded 'down flaps', but would also require a system to small holes or pipes to drain out the last of the water. This system has many moving parts that cannot be lubricated, so binding and galling would be concerns, but it can probably be made to work. It would need to be made very reliable, a few flaps stuck closed wouldn't be a concern, but some stuck open could be a problem. This system has the disadvantage that it prevents lower levels of circulating water during data taking. This recirculating loop will probably be required for; the purification and temperature control of the water, cooling of electronics etc. For these reasons, we prefer the offset tubes option.

When the detector is out of the water, the bottom reflector would need to be segmented to be removed between the support towers. With four towers (see Figure 52), the four bottom cover segments would be 4.6x4.6 meters. Higher segmentation (multiples of 4) would also be possible. We imagine a scissor cart rolled under the detector, lifted to contact a segment. It could then be unbolted, lowered and rolled away. The segments would need to overlap on the inner surface for light seal, and on the outer surface for joining (or have extra joint strips). The top reflector would be craned out, in one piece or in segments.

3. *Walls of Inner Detector (ID)*

The top/bottom walls of the ID would also need to allow water flow, otherwise one would have to allow for the inertia of 400 tons of trapped water. The movement flows would be 42 tons/hour = 0.7 tons/minute. Distributed, this is 27 liters/minute/m^2. This is somewhat less than the 36 liters/minute/m^2 of the reflector, but this wall has all the PMTs as well. In Figure 51, I show the tubes and flaps options for this wall, similar to that for the top and bottom reflectors.

4. *Detector in the shaft*

The detector is guided within the shaft by a set of rails. The current proposal has four rails and support cables but it could be three, five, etc. if dictated by other design considerations. It is important to understand that the ring connections to the rails do not need to be high precision rail bearings. Because the positioning accuracy required is only ≈1cm, they could be simple guides (see Figure 52). Similarly, the rails do not need to be complex. The loose tolerance makes it far less likely that the detector will jam on the rails. When the detector has been moved, there may be a system to lock two of the four guide locations to eliminate small position changes during data taking. Another reason for a looser coupling (before locking), is that then the rails do not need to be so precisely positioned on the shaft walls, i.e. several millimeters versus 0.1mm.

Figure 52 shows the detector in the shaft, the shaft covers and the external towers. Four vertical cables support the assembly. Ballast can be added to the rings, if required. Above ground, there would be four towers extending upwards 17.6 meters. Four motors, acting together, lift or lower the detector in the shaft, or even lift it completely out of the water. The load will increase as it leaves the water (loss of buoyancy), if the load is too much, the top ballast can be removed by crane as it clears the water. Or, a lifting frame could be attached when the top ring clears the water, allowing the crane to raise it further, then it can be locked in the out position, freeing the crane.

In this concept, the signal and power cables for the detector would travel up out of the water beside the four support cables. They would nominally go up and over the towers, then down to the ground racks. With this scheme there would be no extra length in the water, wherever the detector was positioned in the shaft. When the detector is slowly lowered further down the shaft, the cables etc. should be cleaned before entering the water.

Once the detector is entirely out of the water, the shaft covers can be craned back into position (see Figure 53). Adding counterweights will make sure the Center-of-Gravity (COG) of the covers are beyond the detector shadow when the covers are pushed in. The covers would be bolted to the ground. Lightweight seals cover the joints, the central region, and the four small areas where the support cables, signal and power cables exit the water.

Figure 54 shows the detector out of the water and covers reinstalled. It is important that the covers and seals are safe for people and light equipment, so that the bottom of the detector can be worked on. Scaffolding can be erected to work on all parts of the detector. The figure also shows the detector moved to a stand. To move the detector, the lifting frame would be installed, the detector supported, then the eight ring guides removed and two of the towers removed (or laid down), opening a path for the detector move.

Whether above the shaft or on a separate stand, it would probably be useful to be able to remove the reflector sections and get access to parts of the ID. If the ID were bolted together sections, it might be possible to partially disassemble to make repairs and/or replacements.

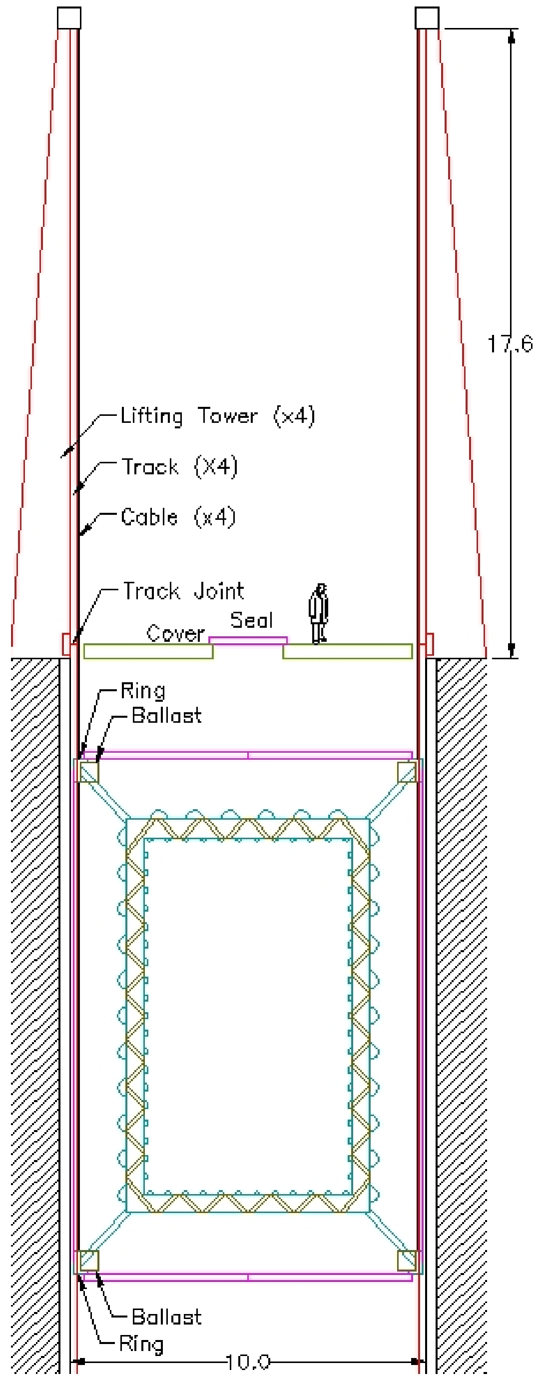

FIG. 52. This shows the detector in the shaft, the shaft covers and the external towers. Four vertical cables support the assembly. Above ground, there would be four towers upwards extending 17.6 meters. Four motors, acting together, lift or lower the detector in the shaft, or even lift it completely out of the water.

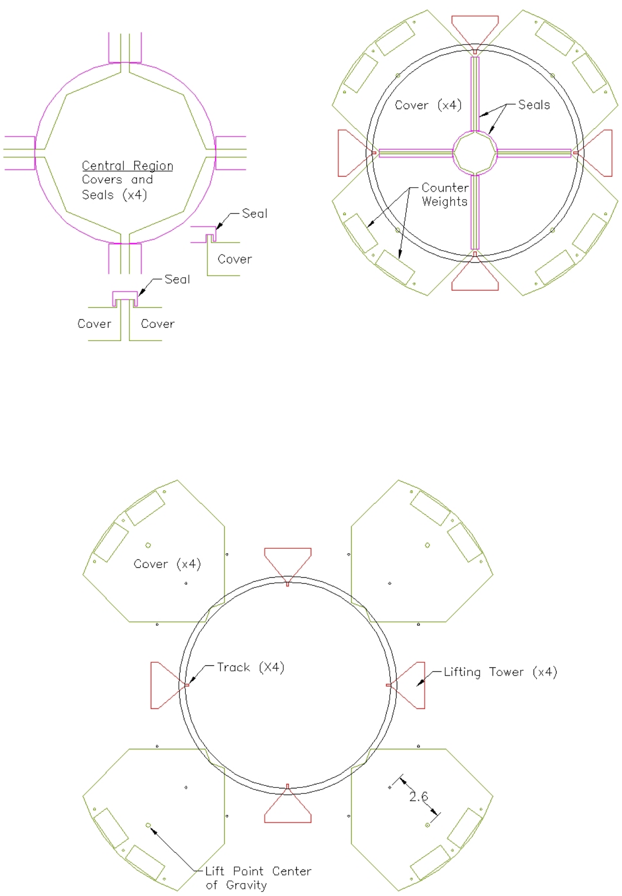

FIG. 53. The four covers can be craned in and out. Added counterweights make sure the center of gravity is beyond the detector shadow when in. The covers are bolted to the ground. Light weight seals cover the joints and the central region.

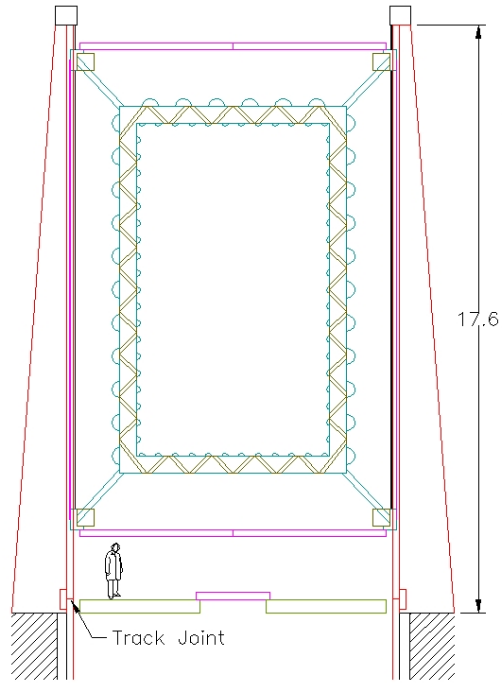

FIG. 54. The four towers allow the detector to be raised out of the water (units in meters). The covers can be reinstalled under the detector, allowing people to work underneath it. A lifting frame can be craned over the detector, attached, and the towers removed. The detector can then be craned to a stand.

5. *Detector Surveying*

As mentioned earlier, after the detector has been moved, there may be a system to lock two of the four guide locations to eliminate small position changes during data taking. A laser surveying system could be in place to look down through the water to periodically check the detector position at the four rail locations. The PMTs may have to be turned off during these times. The positioning of PMTs within the detector would be surveyed during its assembly (out of water) and then should only be subject to thermal expansion/contraction shifts in the water, plus deflections due to loads (primarily the top/bottom PMTs.

The thermal expansion/contractions of the detector will depend on its material. For a 10 meter Aluminum piece, the expansion would be 2.2mm for a 10 OC change. 306 stainless steel would be 1.6mm. The shaft, being reinforced concrete, should expand 1.3mm for 10 degrees. Stainless steel is a better thermal match, the differential expansion being 0.3mm for 10 degrees, compared to 0.9mm for an Aluminum detector frame, but the difference is not likely to be significant.

E. Scintillator panels

The veto system of the NuPRISM detector can be composed of plastic scintillator detectors which completely surround the the water Cherenkov detector. The main purpose of the veto system is to identify backgrounds from beam neutrino interactions in the surrounding pit walls and to provide a cosmic trigger signal for calibration purposes. The technology developed for the ND280 SMRD detector can be applied for this veto system.

1. Scintillator counters with WLS/avalanche photodiode readout

Scintillator counters with wavelength-shifting (WLS) fibers and opto-electronic readout are an established technology for neutrino detectors in long-baseline neutrino oscillation experiments. ND280 consists of several subdetectors which use extruded plastic scintillators of various shape and dimensions [22]. Each of these subdetectors is comprised of plastic slabs and bars, wavelength shifting fibers and compact photosensors - multi-pixel avalanche photodiodes. The Kuraray double-clad Y11 WLS fibers are used in all ND280 scintillator detectors for transportation of the reemitted light to photosensors.

SMRD counter. The SMRD detector was made of the polystyrene-based scintillator slabs, each with an embedded wave-length shifting fiber. The slabs were produced at the Uniplast Factory (Vladimir, Russia). The scintillator composition is a polystyrene doped with 1.5% of paraterphenyl (PTP) and 0.01% of POPOP. The slabs were covered by a chemical reflector by etching the scintillator surface in a chemical agent that results in the formation of a white micropore deposit over a polystyrene[30]. The chemical coating is an excellent reflector, besides it dissolves rough surface acquired during the cutting process. The WLS fiber was read out on both ends to increase light yield, improve uniformity and position accuracy, and provide redundancy.

A key feature of these counters is the usage of the one serpentine-shaped WLS fiber for readout of scintillating signal. The serpentine geometry of a groove consists of 15 half-circles, each with a diameter of 58 mm and straight sections connecting the semi-circles. A 1 mm diameter Y11 (150) Kuraray WLS fibers of flexible S-type and with double-cladding was used for the SMRD counters. Fibers are bent into a serpentine-shape and glued into grooves with BC600 Bicron glue. The mean light yield for sum of both ends was about 40 p.e./MIP after subtraction of the MPPC cross-talk and after pulses. The high light yield allowed us to obtain the efficiency of more than 99.9% for detection of minimum ionizing particles.

The light yield of about 14 p.e. per a minimum ionizing particle ($\sim$ 7 p.e./MeV for 1 cm thick bar) provides the efficiency for detection of minimum ionizing particles of more than 99% in an individual scintillator bar for a detection threshold of 1.5 p.e. Time resolution depends on the light yield as $\sim 1/\sqrt{N_{p.e.}}$ where $N_{p.e.}-$ is the number of photoelectrons. For the l.y. of 20 p.e. the typical resolution is obtained to be σ 1 ns. Detectors with shorter WLS fibers were also tested. Light yield of the detector with a 5 m long WLS Y11 fiber is shown in Fig. 55

In this case, the minimum light yield of more that 40 p.e./MIP (sum of both ends) is obtained.

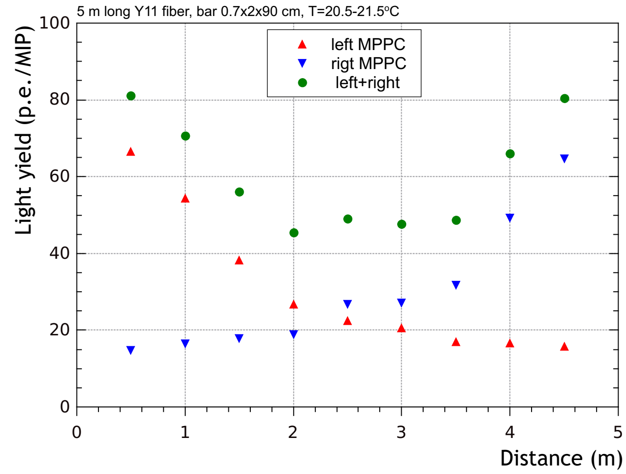

FIG. 55. Light yield of a scintillator counter with 5 m long WLS fiber vs position along the fiber. The T2K 667 pixel MPPC's were used in this measurement.

2. Veto counters for NuPRISM

The excellent performance of the SMRD counters with one serpentine WLS fiber per counter gives a possibility to make a veto system using similar approach. One option is to construct the NuPRISM veto system from scintillator counters, each of 0.2 m^2. One WLS Y11 S-type fiber is embedded in the extruded plastic slab of $2000 \times 200 \times 7\text{mm}^3$. Half-circles have the radius of 3 cm that allows to keep the performace of the fiber without loosing the transmission of the reemitted light along the fiber. A 6 m long Y11 fiber is readout on both ends by MPPC's. Taking into account the improved parameters of new MPPC's, for exmple, higher PDE, we can expect to obtain miminum light yield of 20-30 p.e./MIP and time resolution of about 1 ns for these detectors. More accurate information can be obtained after tests of the conter prototypes.

3. Integrated Design

Initial conceptual drawings of the fully integrated detector are shown in Figure 56. The structure is composed of stainless steel-coated I-beams the define both the inner and outer detector. The scintillator panels are shown covering a portion of the outer detector. The inner detector PMTs have been attached to the frame using stainless steel rods, and the optical separation between the inner and outer detectors is achieved using anodized aluminum plates. Once the experiment is approved, these drawings are intended to help guide the development of a complete set of engineering drawings for the detector.

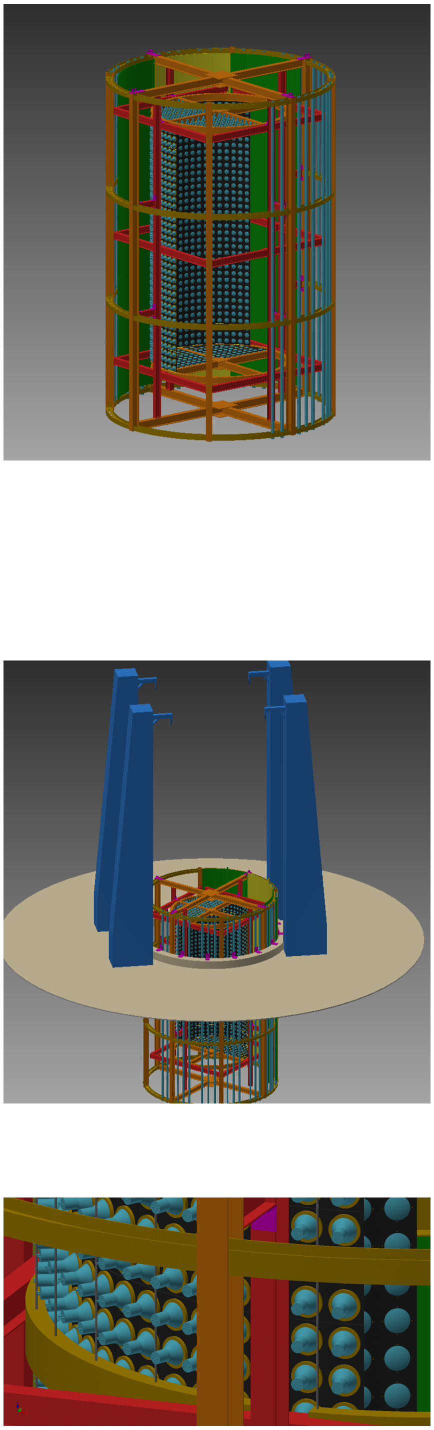

FIG. 56. A conceptual drawing of the fully integrated NuPRISM detector is shown (top), as well as the lifting towers (middle) and a detailed view of the beams supporting the inner detector PMTs (bottom).

F. Photomultiplier Tubes

The original T2K 2 km detector proposal used 8" PMTs to better match the granularity of the 20" PMTs used in the much-larger Super-K detector. The baseline design for the NuPRISM detector is only 6 m in diameter and 10 m tall, which corresponds to 3,120 PMTs for 40% photocathode coverage. This is significantly smaller than the 11,129 PMTs used at Super-K, so to improve the granularity of the detector, 5" PMTs are also being investigated, of which 7,385 PMTs would be required for 40% coverage. Additional options such as avalanche photodiodes and high quantum efficiency coating are also being explored. Initial cost estimates from Hamamatsu for a wide variety of PMT configurations are given in the appendix.

G. Electronics

Part of the goal of the NuPRISM is to serve as a prototype for the Hyper-K. We therefore want NuPRISM to use a set of electronics that is as close as possible to the electronics being proposed for Hyper-K. Some of the key features of the Hyper-K electronics are the following:

- Front-end electronics will be placed in the water, as close as possible to the PMTs.
- Front-end electronics are expected to find all hits above 0.25 PE and send all information about hits up to back-end electronics. In back-end computers trigger decisions will be made using software. No global triggers will be propagated to the front-end electronics.
- PMT digitization should provide 0.05 PE charge resolution, 0.5 ns timing resolution for 1 PE hits and 1250 PE dynamic range.

We shall note various aspects of the NuPRISM electronics where we may differ from the default HK electronics plan. In particular, one clearly different aspect of NuPRISM will be the much higher rate of 'pile-up' events during beam spills. The rate of sand muon events entering the ID may be as high as 0.19 per bunch. At minimum we therefore need electronics that can cleanly distinguish between PMT hits in different bunches; ie, hits with separation of order ≈600ns. We may also want to have some capacity to distinguish between hits within a single bunch; ie hits that differ by 10s of ns. This is a more challenging requirement.

1. *FADC Digitization*

Given this requirement for inter-bunch and intra-bunch hit resolution we propose using FADC (Flash Analog to Digital Converter) digitization with basic digital signal processing in the front-end electronics. The basic scheme is as follows:

1. The stretched/shaped PMT signal is fed into the FADC. Use of a standard commercial FADC is foreseen, with sampling frequency between 80-250 MHz and 12-14 bit resolution.

2. The digital output of the FADC is fed into an FPGA (on the front-end electronics card), where we do basic digital pulse processing (on the fly, at same rate as original digitization). Digital pulse processing would involve the following:

   (a) Digital filtering to improve signal-to-noise ratio and to remove unwanted signal component (for instance from pickup of electromagnetic interference).

   (b) Finding PMT hits.

   (c) Calculating the pulse time and charge.

3. The digital pulse information is then transferred to the back-end electronics. We send different types of data depending on the pulse charge.

It is worth emphasizing that the expected timing resolution using FADCs is not intrinsically limited by the sampling rate. For instance, if you appropriately shape a PMT pulse, you can easily achieve better than 0.5 ns timing resolution using a 100 MHz digitizer (i.e. a sample each 10 ns), as long as you have decent signal to noise ratio, reasonable ADC accuracy (i.e. number of bits) and if you apply correct signal processing algorithms. Therefore, several studies were made in order to estimate impact of noise introduced by electronics and various signal processing algorithms on the overall system performance, so that one can configure the system in an optimum way. In our case an ‘optimum system’ means that error contributions from the acquisition chain would be small compared to errors due to statistics of the observed processes and those introduced by photomultipliers. We present a description of these studies in Sections IV G 3, IV G 4 and IV G 5.

2. *Signal Conditioning And PMT HV Supply*

We propose to use differential transmission in order to deliver signals from the PMT bases to the digitization board. An advantage of such a solution is that, in principle, it would allow us to use a standard unshielded twisted pair cable, while still maintaining fairly good immunity to pickup of electromagnetic interference. The base of the PMT would contain shaping circuitry, which would stretch PMT signals, limiting their bandwidth to match FADC requirements and converting them into a symmetric form, suitable for transmission via a twisted pair cable. Preliminary studies show that signal shaping using a 4-th or 5-th order Bessel-type low pass filter should provide satisfactory results.

One of the design goals for the NuPRISM is minimization of the amount of necessary cables. As such, it would be advisable to use a single cable to provide both high voltage to the PMT and to transmit the signal from the PMT base to the digitization board. Therefore, the preferable solution would be to synthesize the high voltage directly on the PMT base, from a 48-200 V DC supply, using either a commercial high voltage module or a custom designed voltage multiplier structure. This way, power to the PMT base could be delivered via an additional twisted pair of the same cable that would be used to transmit the shaped PMT signal. The slow control link necessary to tune the high voltage for specific PMT could be realized via a DC power line, thus avoiding the need to use additional cables. In any case, it should be emphasized that the details of the PMT HV implementation will depend strongly on the exact PMTs that are chosen.

3. *Study of a Digital Constant Fraction Algorithm*

One of the frequently used algorithms for timing arrival of digitized pulses is the digital constant fraction algorithm. It works in a similar way to its analog counterpart (see Fig. 57), i.e.:

1. The pedestal is estimated using samples preceding the pulse and then it is subtracted from the original signal, thus removing the DC component.

2. An additional signal is created by delaying, inverting and optionally amplifying the original signal. If sub-sample delays are desired, then some form of interpolation is necessary.

3. A composite signal is created by summing the original and the delayed signals.

4. The sample number corresponding to the intersection point of the composite signal and the zero-level is calculated. Linear interpolation is used in order to get a sub-sample position.

An advantage of this algorithm is that, first of all, it is simple. Second, if one is able to avoid sub-sample delays and use gain factor that is a power of two, then the time of pulse arrival can be obtained using little memory and few simple operations – sign inversion, bit-shifting (multiplication by a power of 2), one addition per sample and one sub-sample interpolation, all of which are relatively little demanding on FPGA resources. Even if one uses FFT interpolation to increase sample density in order to reduce errors due to random time offset between the leading edge of the pulse and the phase of the sampling clock, the algorithm is still an attractive option in terms of overall resource usage. On the disadvantage side one should mention the algorithm is potentially unsuitable in case of noisy environments and weak signals, due to following factors:

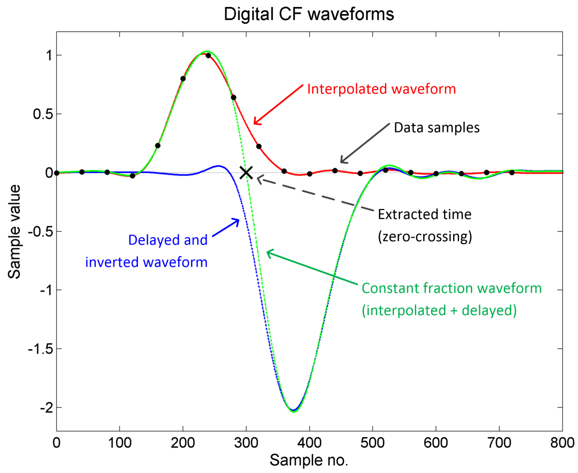

FIG. 57. Algorithm of a digital constant fraction discriminator. Sample indexes are for interpolated waveform (red curve has sample density increased by 40 times).

- the 'zero' level is obtained by subtracting the pedestal estimate from the signal, and this estimate may significantly differ from the real value if noise level is high;
- if the signal to noise ratio is poor, the signal samples will be significantly distorted.

Since only two samples are used to calculate the time of the 'zero-crossing' point, the method is prone to potentially significant errors.

Therefore, a Monte-Carlo study has been performed in order to test the limits of applicability of the digital constant fraction algorithm to signal to noise ratio and the shape of the signal. Since at present stage the major concern is defining performance requirements for the electronics, it was decided to take a general approach and make simulation at a signal layer only, disregarding detailed models of electronic circuits. The main idea was test various combinations of sampling rate, signal to noise ratio and order of the shaping filter. Also, we wanted the results to be applicable to any system, independently of the particular ADC type (i.e. its sampling frequency and the number of bits). For this reason, the following choices were made:

- All the resulting time resolutions were normalized to the pulse rise time.
- The rise time is expressed as the number of samples at the rising edge, defined as a transition from 10% to 90% of the amplitude.
- The shaper circuit has been model using a normalized, ideal Bessel-type low-pass filter.

The simulations were performed in the MATLAB environment. The algorithm of the simulations was as follows (see Fig. 58):

1. An impulse response of an ideal, normalized Bessel-type low pass filter of a given order was calculated.
2. The calculated response was sampled at a frequency giving desired number of samples at the rising edge of the pulse. No quantization was made (i.e. ADC with infinite number of bits was assumed). The sampling process started at a random sub-sample offset t_{offset}, where $t_{offset} \in [0, t_{sample})$ and had a uniform distribution; t_{sample} was the sampling period. This operation accounted for the fact that the phase of the sampling clock was not correlated with the time of pulse arrival.
3. White noise was added to the sampled signal. This step accounted for the electronics noise as well as errors introduced by the quantization process (ADC SNR = 6.02N + 1.76dB, N being the number of bits). Therefore, the finite number of the ADC bits was 'hidden' in the amount of noise added to the signal.
4. The time of pulse arrival was calculated using the digital constant fraction algorithm described above. In order to make the results comparable, FFT interpolation was used so that the constant-fraction algorithm operated on a waveform with 64 samples at the leading edge of the shaper pulse, irrespective of the actual sampling frequency used.
5. The resulting sample number is increased by the initial sub-sample offset t_{offset} and then recorded. Afterwards, the procedure is reiterated starting from point 2, up until reaching required number of iterations.
6. The standard deviation of the achieved distribution of sample indexes is calculated and then normalized by the number of samples at the rising edge.

For every combination of filter order, signal to noise ratio and pulse rise time, the algorithm tested several constant fraction delays and chose the one corresponding to the best timing resolution.

Example results are shown in Fig 59. As expected, the most important factor affecting the timing performance was the signal to noise ratio. What did came out little surprising was a relatively low impact of the sampling rate with respect to the rise time of the shaper pulse. For higher signal to noise ratios (SNR) it seems that 1.4 to 1.6 samples at the rising edge is enough to get time resolutions of better than 1% of the rise time. For poor SNR increasing sampling density has little effect on timing performance of the algorithm. The above is a significant hint as to which way to go further – while a faster system means shorter rise times, it also means wider bandwidth and hence worse signal to noise ratios. As such, it may be worth to analyze the interrelationship between the sampling rate and signal to noise ratio to see whether an optimum can be reached at some point.

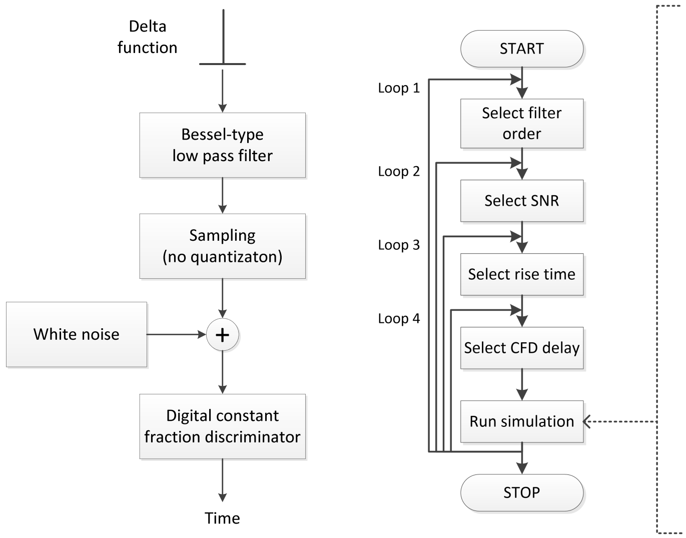

FIG. 58. Simulation setup (left) and algorithm (right) for studying the timing accuracy achievable when using the digital constant fraction algorithm, under various combinations of the order of the shaper (Bessel-type low-pass filter), sampling rate of the ADC and signal-to-noise ratio.

It may well be that the desired timing resolution can be achieved using a slower system just because the SNR will be improved. Nevertheless, the most important conclusion is that with a digital constant fraction approach it may be rather difficult to achieve desired timing resolution, given the dynamic range requirement. One needs to find signal processing methods which are better suited for low SNR scenarios.

When it comes to the order of the Bessel-type shaping filter, there was little improvement when using filters of orders above four. The major advantage of a higher order filter is a more symmetric and thus shorter pulse, which may aid if pile-up is expected. However, a filter of order four or five already outputs a pulse with nearly equal rise and fall times.

4. *Tests Using an Arbitrary Waveform Generator*

A test setup has been built in order to determine, primarily, the timing resolution of various FADC setups (Fig. 60) and, additionally, to provide validation for the simulations. The setup consisted of an arbitrary waveform generator (AWG) Agilent 33600A with 80 MHz analog bandwidth, and sampling rate of 1 GSPS, which created signals resembling what is expected to be seen from a photomultiplier (PMT). We have chosen to use an AWG instead of a PMT because the purpose of the tests was to assess the performance of the electronics only, and the PMT would introduce additional, possibly dominant errors to the time measurements. One channel of the AWG was connected directly to the ADC, while the other was connected to the shaper, which in turn was connected to the second channel of the ADC. The shaping amplifiers were designed based on the results of the study of the timing performance of the digital constant fraction algorithm. One nominally has an impulse response with a 15 ns rise-time while another has a response with a 30 ns rise-time. Lastly, three different commercial ADCs or "digitizers" have been investigated:

- The CAEN DT5724; 100 MSPS, 14-bit, 4 channels
- The CAEN V1720; 250 MSPS, 12-bit, 8 channels
- The CAEN V1730; 500 MSPS, 14-bit, 16 channels

To obtain our timing resolution measurements two pulses are simultaneously generated by the AWG, one large 'reference' pulse with a high SNR, and a smaller 'signal' of the same form that gets manipulated for testing. The reference pulse heads straight to the ADC but the signal pulse passes through one of the shapers first. The arrival time of each pulse is deduced in ROOT by fitting a skewed Gaussian to the data. The skewed Gaussian was chosen because the waveform seemed to rise slightly quicker than it dropped. This function has a number of parts but is of the form

$$f(x) = \frac{\phi(y)}{\alpha - \kappa(x - \xi)}$$

where $\phi(y)$ is a standard Gaussian, ξ is the mean, α is a scaling factor, κ is a skewing factor, and

$$y = -\frac{1}{\kappa}\log[1 - \kappa(x - \xi)/\alpha].$$

After fitting, the peak time of the fit is chosen as the pulse arrival time to be used. The difference in the pulse times between the reference and shaper signals was calculated for several thousand events, and the timing resolution is

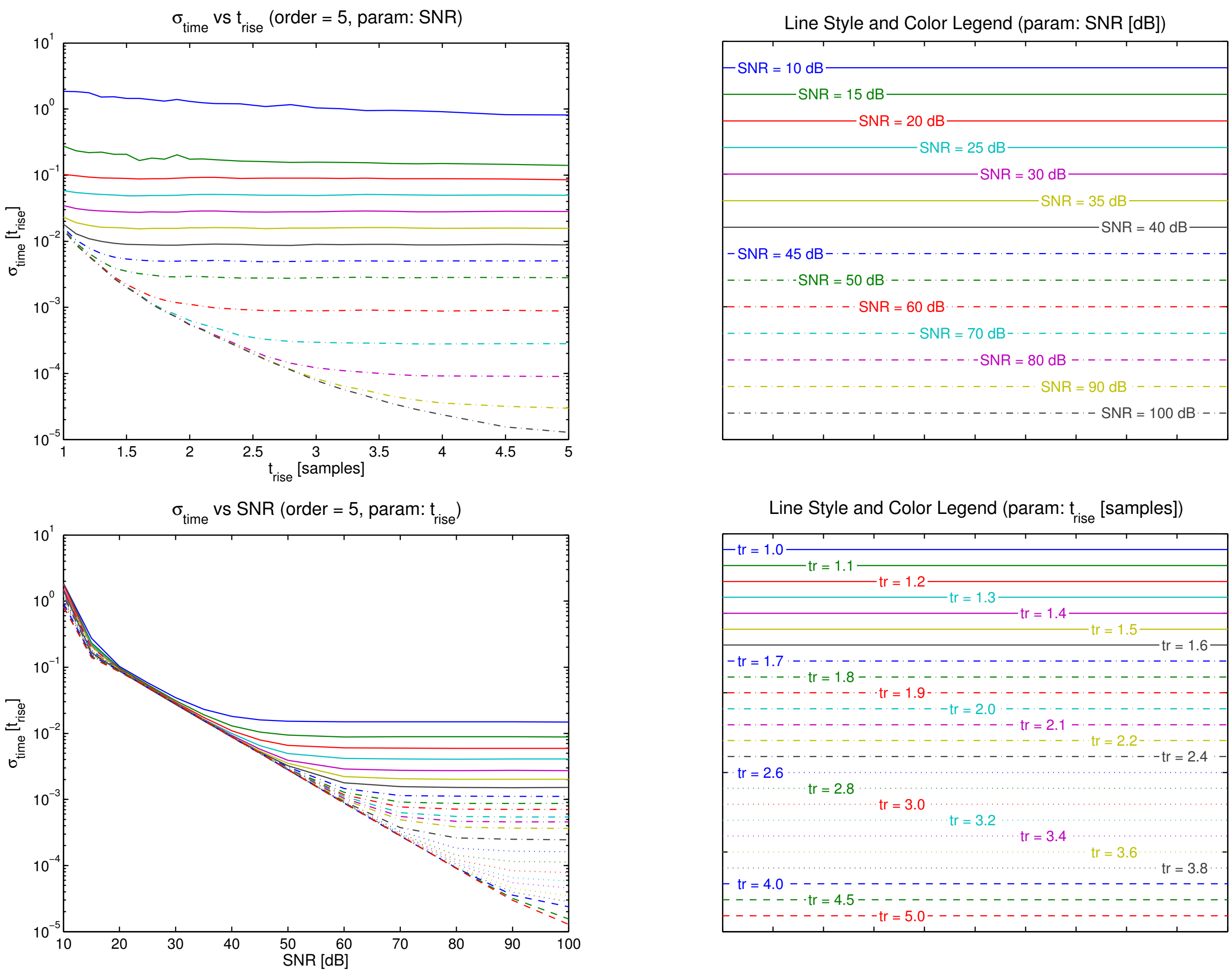

FIG. 59. Results of the study of the timing resolution of the digital constant fraction algorithm. The top row shows results parameterized by the signal-to-noise ratio (SNR), whereas the bottom row show the same data but parameterized by the amount of samples at the rising edge of the pulse (10% to 90% of the amplitude).

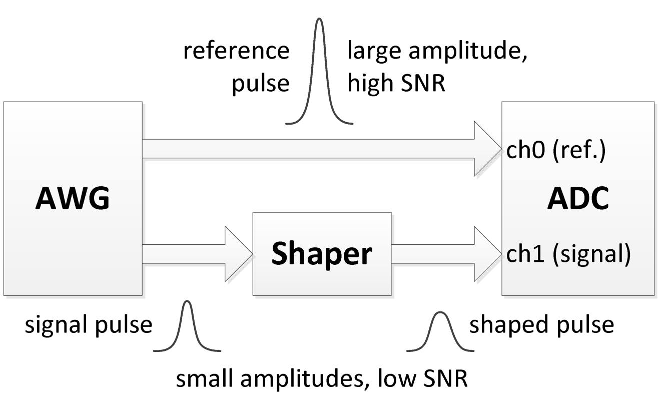

FIG. 60. Measurement setup for studying time resolution of various configurations of ADCs and shapers.

taken from the RMS of the distribution of timing differences. The signal pulse has been manipulated in various ways to see how timing resolution is affected. The modifications included varying the pulse height, passing it through long cables, and using a double or twin pulse waveform.

Fig. 61 shows timing resolution vs. signal pulse height for the three different digitizers and each shaper. Not surprisingly the 500 MSPS digitizer, offering many samples along the pulse, performed the best. Nevertheless, the 100 MSPS digitizer seems to offer near the same resolution and appears to be a better choice, as it is less expensive. Trailing behind is the 250 MSPS, which has worse SNR due to lower accuracy (12-bit as opposed to 14-bit in the other two). This seems to confirm that it is the signal to noise ration that is the key issue. However, it should be mentioned that the shapers were optimized for the 100 MSPS digitizer and in the 250 MSPS and 500 MSPS cases the pulse shape was suboptimal. Still another conclusion is that the 15 ns shaper gave better results than the 30 ns one – which again agrees with the simulation and suggest that an attention should be paid to choosing proper shaping times.

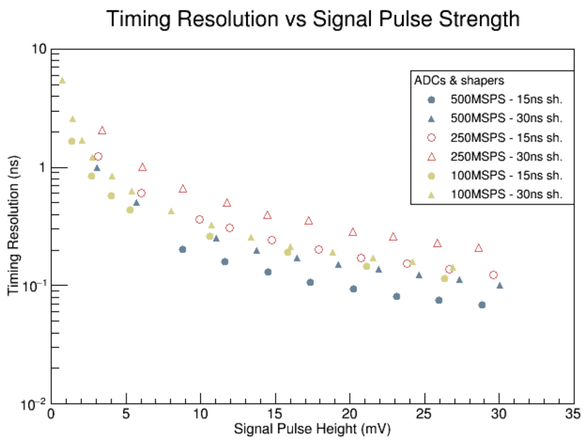

FIG. 61. Timing resolution vs. signal pulse height for both shapers and all three digitizers.

One of the tests performed was to see how sending the signal pulse through a long cable would affect characteristics such as its attenuation and the timing resolution. Fig. 62 results for the signal pulse that was sent through a 450ft cable under two different configurations – the shaper placed before the cable and the shaper placed afterwards. The 100 MSPS digitizer was used for this test. What was quite positive about these results was that, for the shaper-before configuration, the timing resolution was entirely unaffected, even after almost 50% attenuation. The shaper-after configuration however consistently worsened the resolution - which agrees with expectation, as in this configuration the SNR deteriorates with increasing the cable length. These results indicate that, with the proper signal amplification at each PMT, there is quite some freedom in the choosing PMT and electronics design, because such long cables can be used.

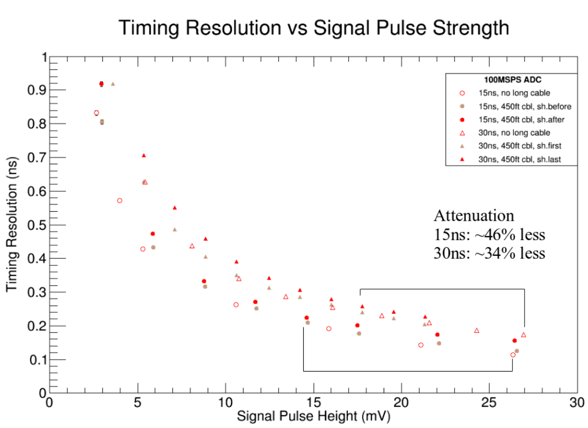

FIG. 62. Timing resolution vs. signal pulse height with and without the addition of a long 450ft cable. One configuration had the shaper placed before and another had the shaper placed after the long cable.

Finally, time resolution measurements have been done using a double pulse structure for the signal, with pulse separations ranging from 40 ns up to 120 ns. An example pulse is shown in Fig. 63. For the 15 ns shaper, the resolution was quite stable even after the pulses were significantly overlapping at around 40 ns, as shown in Fig. 64. These tests were done with the 100 MSPS digitizer, though it might be interesting to see how other digitizers perform considering that the 100 MSPS is limited in how close the pulses can be brought together. Even so, the resolution on the latter pulse compares extremely well under this configuration, deviating by only ≈0.01 ns.

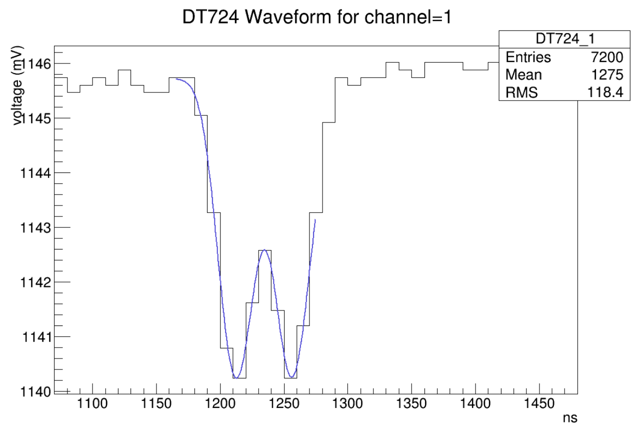

FIG. 63. Double pulse with the 15ns shaper and 100 MSPS digitizer, along with a fitted function to determine peak times.

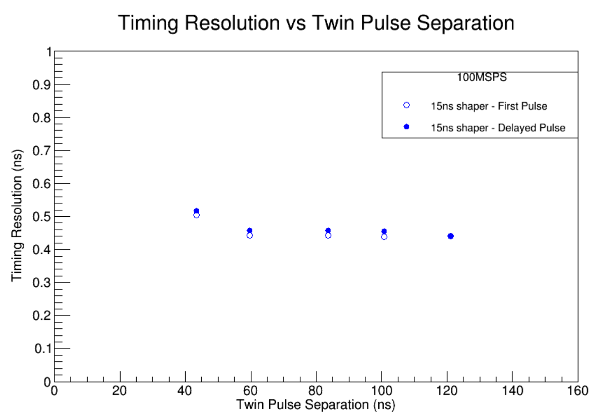

FIG. 64. Timing resolution vs. twin pulse peak separation.

5. *Noise Study and Optimum Filtering*

Since the amount of noise is a key factor determining performance of the whole system, a detailed noise study has been performed using the equipment described in section IV G 4. Noise data was acquired using several equipment configurations for the 100 MSPS and 250 MSPS digitizers, including:

1. ADC with both inputs unconnected

2. ADC with one input unconnected and the other input connected to the output of the shaper. The shaper's input was left floating.

3. Both inputs of the ADC connected to the AWG, with the AWG turned on but producing no signal.

4. One input of the ADC connected to the AWG and the other connected to the shaper. The shaper input is connected to the second channel of the ADC. The AWG was on, but again producing no signal. This was the configuration used for testing the time resolution in section IV G 4.

Runs in each of the configuration consisted of several thousands of events and the acquisition time for a single event was 100 μs. Afterwards, an estimate of noise spectrum was calculated using a smoothed, averaged periodogram, with a frequency resolution of 10 kHz. Prior to periodogram calculation, samples from each event were processed by the Hanning window. The window length was equal to the amount of samples in the event. Figs. 65 and 66 show an example noise spectrum for the configuration 'ADC+shaper' (IV G 4), for both 100 MSPS and 250 MSPS digitizers, respectively. As expected, it can be clearly observed that the 12-bit ADC is noisier that the 14-bit one. Furthermore, the noise spectrum is not white, i.e. sample-to-sample correlations are present. The frequency peaks also indicate presence of deterministic components, probably due to electromagnetic interference pickup.

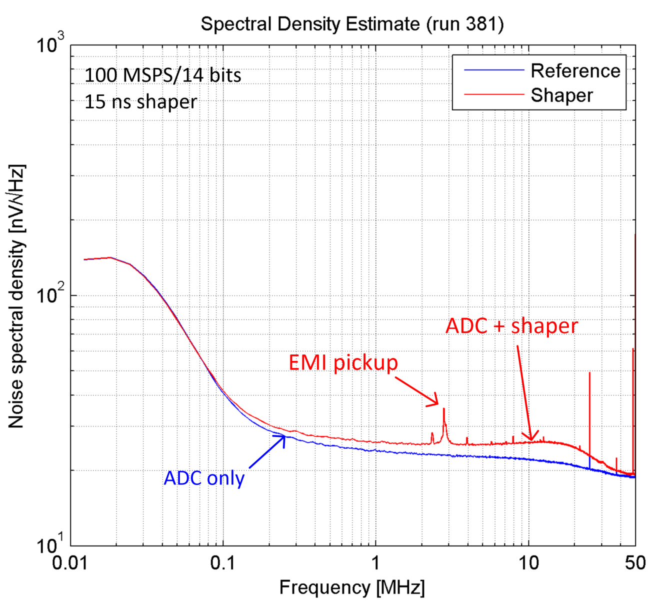

FIG. 65. Example estimates of noise spectrum of the 100 MSPS, 14-bit digitizer (CAEN DT5724). The 'reference' channel had unconnected input (blue curve), while the 'shaper' channel had it input connected to the 15 ns shaper (red curve). The input of the shaper was unconnected.

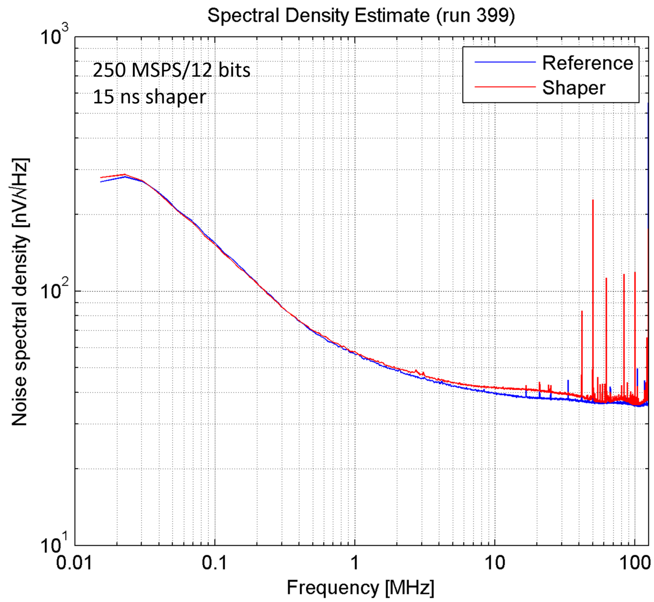

FIG. 66. Example estimates of noise spectrum of 250 MSPS, 12-bit digitizer (CAEN V1720). The 'reference' channel had unconnected input (blue curve), while the 'shaper' channel had it input connected to the 15 ns shaper (red curve). The input of the shaper was unconnected.

Based on the results of the above measurements and information available in published articles, the following requirements for the signal processing methods were formed:

- Account for arbitrary noise spectrum present in real experimental conditions, in particular ability to work in presence of correlated noise.

- Ability to filter out individual frequency components originating from a pickup of electromagnetic interference.

- Ability to remove the DC component of the signal, thus removing the need for pedestal estimation.

- Shorten the pulses by performing some form of deconvolution, thus improving the ability to properly detect events that are closely spaced in time.

- Minimize effects of quantization noise resulting from limited number of ADC bits, therefore allowing for use of less precise digitizers.

Given the above requirements, the finite impulse response (FIR) filters were chosen.

From our perspective, the FIR filter can be treated as a 'black box' that changes one signal into another, which is more appropriate for further processing, be it estimation of time of arrival or estimation of charge. Each sample of the output signal is a convolution of the filter's impulse response and the input signal or, in other words, each output sample is a weighted sum of samples of the input signal:

$$y[n] = \sum_{l=0}^{N-1} h[n] \cdot x[n-l] \tag{9}$$

where y is the output signal, x is the input signal, h is the filter's impulse response and N is the number of filter taps (i.e. number of input samples used in calculation of the output sample). Two big advantages of this approach are:

- An arbitrary filter impulse response is possible.
- By definition, the algorithm is stable.

The key issue is the choice of optimal shape of the output pulse and of the filter's impulse response.

Based on the published literature (for example [58]), we propose to use the 'Digital Penalized Least Mean Squares' (DPLMS) method [59–62] for the synthesis of the filter response. We intend to use two filters, one optimized for pulse timing [63] and the other one optimized for charge estimation (Fig. 67). The studies of the method are on-going.

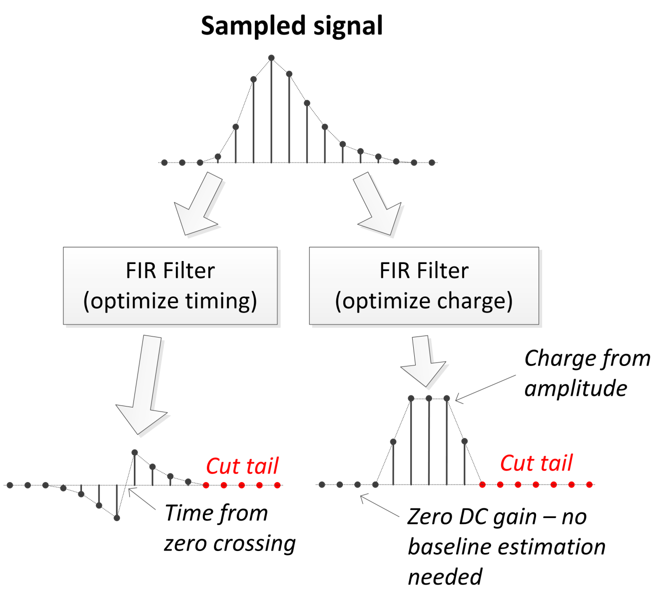

FIG. 67. Overview of the proposed signal processing using finite impulse response filters.

H. Water System

Starting with the very first large-scale Water Cherenkov detector – the Irvine Michigan Brookhaven [IMB] proton decay experiment, which began taking data in the early 1980's – exceptional water clarity has been of key importance for massive devices of this kind. There is little benefit in making a very large detector unless the target mass contained within the detector can be efficiently observed. Good water quality has two main advantages: the light generated by physics interactions in the water can propagate long distances with minimal attenuation until it is collected by photomultiplier tubes or other technologies, aiding accurate energy reconstruction, and the light can traverse these distances (10's of meters) with minimal scattering, which aids in the precise reconstruction of event vertices.

The strategy employed to create kilotons of extremely clear water has been to remove all suspended solids, dissolved gases, ions, and biologics from solution via a series of filtration elements. These include microfiltration filters, degasifiers (vacuum and/or membrane type), reverse osmosis membranes [RO], de-ionization resins [DI], and exposure to intense ultraviolet light [UV].

These water systems typically run in one of two modes: fill or recirculation. During the fill mode, water supplied by the local municipality or ground water in the vicinity of the experiment is first brought up to ultrapure levels and then injected into the detector. The capacity of the water system, along with availability of water, defines how long it will take to fill the detector. During recirculation mode, already high-quality water from the detector is continuously passed through the filtration system and returned to the detector after being cleaned even further. This is necessary as transparency-impairing materials are steadily leaching into the chemically active ultrapure water. In addition, during the process of filtration the water is typically chilled to further impede biological growth, with the added benefit of simultaneously reducing PMT dark noise which is typically strongly temperature dependent.

In the current baseline design, NuPRISM will have interior dimensions ten times smaller than Super-K. It is therefore possible that a commensurately less powerful water filtration system would be able to provide sufficient water transparency. Nevertheless, for now we will base our initial system design and flow rates on water systems known to have worked and produced useful physics in the past.

Following this approach, a baseline design and cost estimate for the NuPRISM water system has been prepared. The primary components described above are represented graphically in Figure 68. This system will be capable of filling the detector at a rate of 6.3 tons/hour, such that a complete fill can be completed in one month of operations. It will be capable of recirculating the water at a rate of 6.3 tons/hour through the entire system plus an additional 22.8 tons/hour through what is known as a secondary "fast recirculation" path which trades some filtration components for faster overall flow. The combination of complete cleaning and fast recirculation has been shown at previous experiments (including the K2K one kiloton near detector) to be the most cost-effective way of achieving the desired water transparencies. A preliminary cost estimate for this baseline water system from South Coast Water in the is $350,000, including shipping, duties, and installation at the detector site.

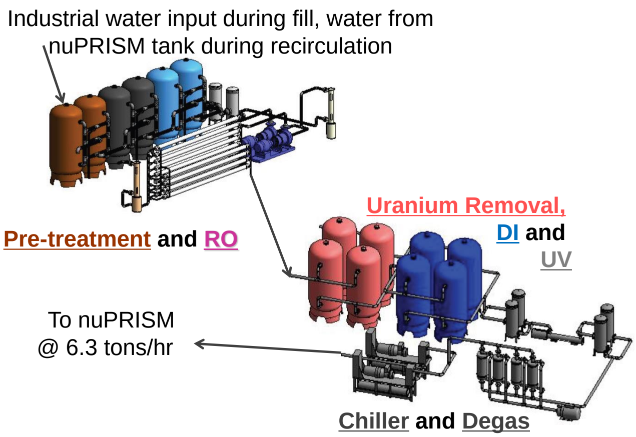

FIG. 68. A preliminary baseline design of the NuPRISM water system.

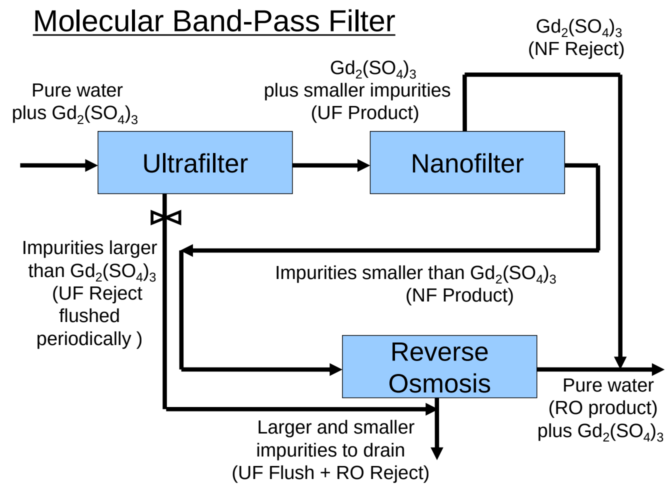

FIG. 69. A schematic illustration of the principle of the "molecular band-pass filter". Successively fine filter elements isolate the dissolved gadolinium sulfate ions and return them to the main tank, bypassing water system elements which would be fouled if they were to trap gadolinium.

1. *Gd option*

If it is decided to add 0.2% gadolinium sulfate by mass to Super-Kamiokande in order to provide efficient tagging of neutrons in water, it will likely be useful for a near detector at Tokai to also be Gd-loaded such that the responses of both detectors are as similar as possible. As a large water Cherenkov detector, NuPRISM is a natural candidate for eventual Gd-loading. Therefore, the implications this has on the water system design must be taken into account.

Over the past decade there have been focused R&D programs both in the US and Japan aimed at devising a method capable of maintaining the exceptional water transparency discussed above, while at the same time maintaining the desired level of dissolved gadolinium in solution. In other words, somehow the water must be continuously recirculated and cleaned of everything *except* gadolinium sulfate.

Starting in 2007 with a 0.2 ton/hour prototype at the University of California, Irvine, since 2009 the Kamioka-based EGADS (Evaluating Gadolinium's Action on Detector Systems) project has shown that such a selective water filtration technology – known as a "molecular band-pass filter" and schematically shown in Figure 69 – is feasible at 3 tons/hour. As the EGADS design is modular and uses off-the-shelf and readily available equipment, albeit in novel ways, scaling it up from the current 3 tons/hour to 60 tons/hour for Super-Kamiokande, is straightforward, while scaling to NuPRISM's 6.3 tons/hours would be trivial.

V. DETECTOR CALIBRATION

The calibration systems for NuPRISM will largely borrow from the existing Super-K calibration systems. However, NuPRISM will also face some unique challenges:

- The PMT frame will move within the water volume.
- Accessing the inner detector is more difficult when the position of the top of the detector is not fixed.

To address these issues, NuPRISM will consist of calibration sources that are fixed within the ID (e.g. laser balls, LEDs, and scintillation cubes), as well as sources that can be lowered though remote-controlled access portals (e.g. radioactive sources). It is expected that each time the detector is moved, all of the PMTs will need to be recalibrated. This can be accomplished using the fixed light sources within the ID, and additional calibration runs with radioactive sources will be taken for each new detector position.

In addition to the detector response, it will also be necessary to precisely determine both the relative position of the PMTs within the ID, as well as the absolute position of the PMT frame within the water volume. This will be accomplished with a laser calibration system. An R&D program is planned to demonstrate the effectiveness of such a system when operated in water.

As NuPRISM will essentially reuse many of the established Super-K calibration techniques, the remainder of this section will provide a brief description of Super-K calibration systems. Further details can be found elsewhere [27, 28].

A. Overview of Super-K Calibration Systems

This section overviews Super-K detector calibrations. For further details, reader can also refer to [27, 28].

The Super-K detector calibration can be divided into two steps; the detector hardware calibrations and the calibrations for physics analyses. The first step is common over all physics analyses, but the second step is designed for each physics analysis goal.

1. *Detector hardware calibrations*

The detector hardware calibrations (measurements) consist of several parts:

- Geometrical surveys: tank geometry, PMT positions
- Geomagnetic field
- PMT calibration: gain, photo-detection efficiency
- Readout channel (PMT and electronics) calibrations: linearity, timing, timing resolution
- Optical properties: water, PMT glass, black sheet, etc (for detector MC tuning)
- Water temperature

All of these calibrations and measurements are indispensable to understand the detector and to model the detector in the simulation. This section focuses on the PMT calibrations and readout channel calibrations, which will be most relevant to NuPRISM.

The PMT calibration procedure can be divided into three large steps; 1) pre-calibration, 2) post-installation calibration, 3) detector monitoring. At the stage of 'pre-calibration', a fraction of all Super-K PMTs have been calibrated prior to the installation, e.g. a tuning of PMT gain. The pre-calibrated PMT, called *standard PMTs*, were used to calibrate all other PMTs *in-situ* after installed, at the stage of post-installation calibration. Once all PMT are calibrated, the stability of the PMTs is monitored continuously for the lifetime of the experiment. The following sections discuss our ideas for each of the PMT calibration steps.

a. Pre-calibration SK has 420 standard PMTs, which corresponds to about 4% of all SK PMTs. The SK standard PMTs were calibrated prior to the installation by adjusting HV values to have identical charge (~ 30 p.e.) over the standard PMTs. For the pre-calibration, SK employed a xenon lamp and scintillator ball. Figure 70 shows a schematic diagram of the pre-calibration set-up.

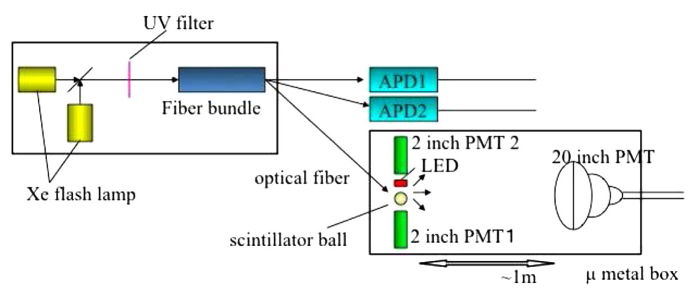

FIG. 70. SK pre-calibration set-up. (Figure quoted from [28])

The SK standard PMTs were installed in the tank in a geometrically symmetric configuration. Figure 71 shows the location of the standard PMTs in SK inner detector.

b. Post-installation calibrations In the post-installation calibration, all PMTs other than the standard PMTs were calibrated *in-situ* after installed. At this stage, all PMT parameters were determined and measured. We will discuss the following items in this section,

- HV (gain) tuning
  Tune HV for all PMTs, referencing to the standard PMTs by using the Xe lamp and deploying a scintillator ball in the tank (the same light source used in the pre-calibration). Move the scintillator ball along Z-axis (height direction), and tune

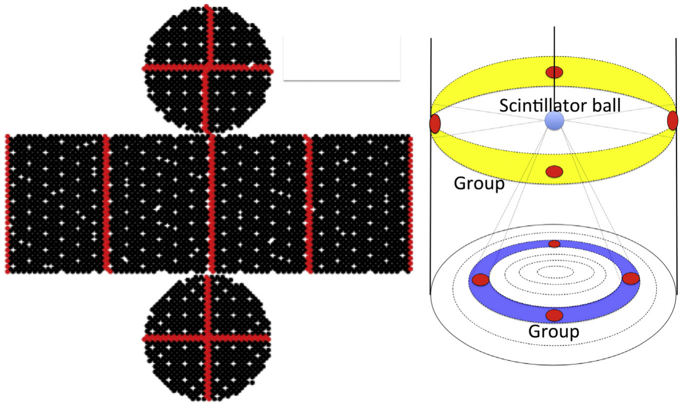

FIG. 71. Layout of SK standard PMTs. (Figure quoted from [28])

HV group-by-group, where the group is defined by Fig. 71.

- Charge to photo-electron conversion
  Conversion factor of charge (pC) to photo-electron (p.e.) were obtained by measuring 1 p.e. distribution. SK deployed "nickel source" in the tank, that generate 1 p.e. level of light, where the nickel source is nickel-californium source; Ni(n,γ)Ni, E_γ ~9 MeV. Figure 72 shows the SK nickel source.

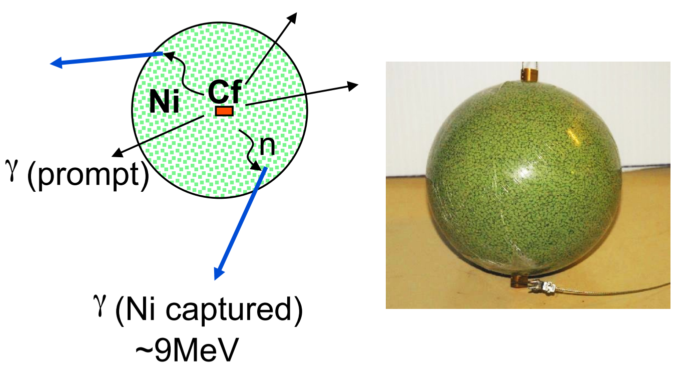

FIG. 72. SK "Nickel source" (Figure quoted from [28])

- Photo-detection efficiency
  The photo-detection efficiency, ϵ, is defined by Quantum Efficiency times Collection Efficiency (CE). Hit rate (Nhit) for 1 p.e. level of light is proportional to the photo-detection efficiency; $N_{hit} \propto N_{photon} \cdot \epsilon$. For this measurement, SK used the Nickel source to evaluate the hit rate, and compare with MC to evaluate *relative* efficiency over all PMTs.

- Timing calibration
  Calibration for time response of readout channel (PMT and electronics), e.g. *time-walk* effect. SK employed N_2-dye laser and deployed diffuser-ball in tank, that light source can generate 0.1∼1000 p.e. level light and covers the entire dynamic range of electronics. Evaluate TQ-maps for every single PMTs, and evaluate detector timing resolution (for MC input).

2. *Calibrations for physics analyses*

The calibrations for physics analyses need to be designed for physics goal basis. This section describes the calibrations used for SK atmospheric neutrino and T2K analyses, that relevant to NuPRISM physics goals.

a. Photon yield and charge scale Although several detailed detector calibrations have been carried out, there are uncertainties on the photon propagation and photon detection of the detector, that need to be tuned in the detector simulation using a well known control samples. For that, SK uses cosmic-ray muons, called "vertical through-going muons". Figure 73 shows a schematic of vertical through-going muon event of SK. The absolute

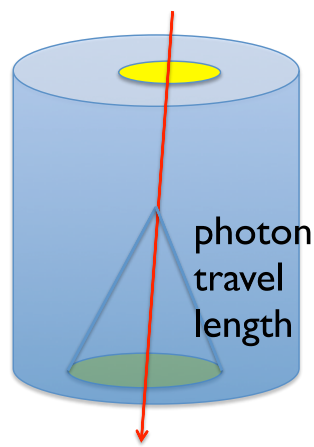

FIG. 73. Schematic of SK vertical through-going muon events.

photon yield and charge scale in the detector simulation have been tuned to data using the vertical through-going muon events that provide known muon track length and Cherenkov photon travel distance.

b. Momentum and energy scale SK event reconstruction algorithm uses a conversion table that translate the observed total charge in the Cherenkov ring to the particle (muons and electrons) momentum. The conversion table is called "momentum table" have been evaluated using the detector simulation by generating particles in momentum range of 10's MeV/c to GeV/c. Based on all detector calibrations and the simulation tuning, the detector and simulation are ready to use for physics analyses. Absolute energy scale is checked using natural sources; decay electron, π^0 mass, sub-GeV stopping muons, and multi-GeV stopping muons, these sources cover the energy range of 10's MeV to 10 GeV. SK detector simulation reproduces data within $\sim 2\%$ and that have been continuously monitored. SK defines the energy scale uncertainty as the data-MC difference. If the simulation does not reproduce the data reasonably well, the detector calibrations and simulation tuning need to be revised.

VI. NUPRISM PHASE 0

The NuPRISM detector requires the construction of a new facility off the J-PARC site that includes the excavation of a 4000 m^3 detector pit. In the scenario where funds and KEK resources are not available for the construction of the NuPRISM facility before 2020, the NuPRISM collaboration proposes a staged approach to the NuPRISM experiment. In NuPRISM Phase 0, the instrumented 14 m tall, 10 m diameter tank, that will eventually be installed in the NuPRISM pit, would first be situated at the ground level near the T2K near detector facilities on the J-PARC site. By installing the NuPRISM detector on the surface at the 280 m baseline, a number of goals can be achieved:

- The T2K Phase 2 and Hyper-K experiments will require systematic errors in near detectors at the percent level. By first placing the NuPRISM detector on the surface in the J-PARC neutrino beam, the calibration procedures can be implemented in an easily accessible, stationary detector, allowing for the in-situ refinement of the calibration and detector modelling procedure.

- Detector systems such as photo-detectors, the water system and electronics, as well as materials such as the black sheet, the PMT support structure and acrylic photo-detector vessels will be operated in an integrated environment. Operation experience may be used to refine systems and materials for the second phase of NuPRISM or even the Hyper-K detector.

- At a large off-axis angle, the ν_μ flux is suppressed relative to the intrinsic ν_e flux, allowing for a measurement of the ν_e cross-section with a high purity sample of ν_e candidates. Despite the suppression of the ν_μ flux, there will still be a significant number of ν_μ interactions that can be used to study neutrino scattering on a water target.

The calibration system for NuPRISM is discussed in Section V. To meet the requirements of T2K-II and Hyper-K, the NuPRISM detector response will need to be calibrated to the level of 2% or better. This level of precision is a challenge for a water Cherenkov detector with a significant fraction of the detector volume near to the detector walls, where uncertainties on the optical properties of detector components and alignment of the photo-detectors can significantly impact the ability to accurately model the detector response. The primary purpose of NuPRISM Phase 0 is to operate the fully integrated NuPRISM detector in an easily accessible location where the calibration systems can be deployed, operated, integrated into physics measurements and refined as necessary. The phased program will ensure that the calibration systems and procedures implemented in the final phase of NuPRISM will be tested in real neutrino beam measurements of muon and electron neutrinos and will meet the requirements necessary for the T2K-II and Hyper-K programs.

It is assumed that Phase 0 program of NuPRISM will include 2-3 years of operation starting around 2020. Given the projected J-PARC accelerator performance and the assumption of 10^7 sec of fast extraction operation per year, in total $4 \times 10^{21} - 6 \times 10^{21}$ protons on target are expected for NuPRISM Phase 0. Event rate projections shown below are for the neutrino mode operation, which is assumed to be half of the delivered beam in NuPRISM Phase 0. Hence, projected event rates are shown for 2×10^{21} protons on target.

The potential locations for the NuPRISM Phase 0 are being investigated and further details will be presented at the July 2016 J-PARC PAC meeting. At the ground level above the T2K 280 m site, the off-axis angle is 6.6°. However, the NuPRISM Phase 0 detector may be moved horizontally away from the average beam direction, so we have studied expected event rates for off-axis angles of 6°, 9° and 12°. The ν_e and ν_μ spectra are shown in Fig. 74. The integrated ν_μ flux at 9° off-axis is reduced by a factor of 40 compared to 2.5° off-axis. This lowers the event rate enough that the kiloton scale water Cherenkov detector can be operated at a 280 m baseline without too much event pile-up. On the other hand, the integrated ν_e flux is only reduced by a factor of 6 and peaked more at low energy. A softer ν_e spectrum is preferred since the uncertainties on the ν_e cross-section from form factor uncertainties and phase space differences tend to be larger at lower energy [8].

The event rates are studied by generating the neutrino fluxes at the 280 m baseline and reweighting the NuPRISM WCSim based MC with 3 m radius inner detector using the neutrino energy dependent ratio of the 280 m off-axis fluxes to the NuPRISM 1 km fluxes. Table IX lists the expected rates of 1Re and 1Rμ candidates for an exposure of 2×10^{21} protons on target in neutrino mode, and reconstructed energy spectra are shown in Fig. 75 and Fig. 76. Even at an off-axis angle of 12°, the 1Re rate is comparable to the expected rate for the NuPRISM measurement at a baseline of 1 km in the $2.5° - 4.0°$ off-axis angle range, and the purity is improved from 71% to 86%. With a fixed position, NuPRISM Phase 0 cannot match the ν_μ flux to the ν_e for the cross section ratio measurement using linear combinations of off-axis angles, however the high statistics and purity indicate that a ν_e cross-section measurement of unprecedented precision can be achieved. The 1Rμ event rates show an interesting two-peak structure for

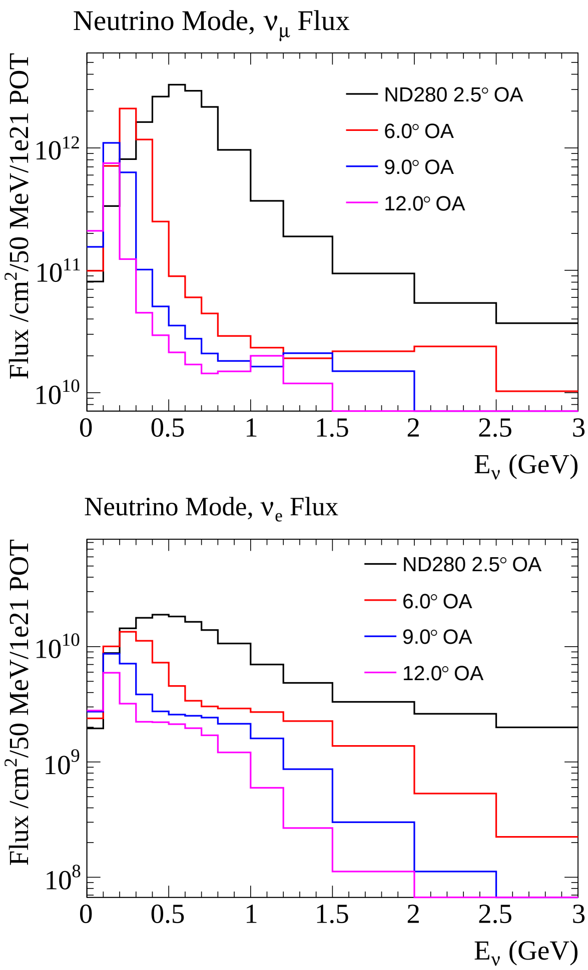

FIG. 74. The 6°, 9° and 12° off-axis ν_μ (top) and ν_e (bottom) spectra. The 2.5° off-axis spectrum is also showed for comparison.

the 9° and 12° off-axis positions with a low energy peak and a second peak around 800 MeV. The second peak comes from neutrinos produced in kaon decays and its relative fraction is enhanced as the peak from pion decays moves to lower energy where the cross-section is suppressed. The lower energy peak from pion decays provides the opportunity to study ν_μ-CC interaction near the threshold where nuclear effects are expected to be significant. The peak from kaon decays can be used to study interactions that are relevant for the accelerator and atmospheric neutrino measurements. In particular, with Gd loading in the detector, the neutron multiplicities can be studied both for events near the threshold and for $\mathcal{O}$(1 GeV) events, the energy region of interest for atmospheric neutrinos.

The physics program of NuPRISM Phase 0 will take advantage of the large off-axis properties of the neutrino flux to make measurements that compliment the ultimate NuPRISM physics program. Although NuPRISM Phase 0 cannot study the nuclear effect in detail since it does not cover ranges of off-axis angles, it can provide interesting information complimentary to NuPRISM. The Phase 0 provides large statistics of ν_e and $\bar{\nu}_e$ samples with better purity in the signal region of 0.4-1.2GeV. There are muon neutrinos in this energy region coming from kaon decays, which can provide a constraint on this component of the flux. The off-axis peak energies for ν_e and ν_μ are below 300 MeV, which will provide samples near threshold where nuclear effects and the ν_e/ν_μ cross section difference are expected to be large, allowing sensitive test of models.

TABLE IX. The expected number of selected 1Re and 1Rμ candidate events in the NuPRISM Phase 0 detector at different off-axis angles at a baseline of 280 m for 2×10^{21} protons on target in neutrino mode.

Off-axis Angle	1Re Events ($<$ 1.2 GeV)	ν_e-CC Purity
6°	10626	79.5%
9°	5781	83.5%
12°	3480	86.4%
Off-axis Angle	1Rμ Events	ν_μ-CC Purity
6°	3.33e5	92.7%
9°	1.09e5	90.4%
12°	6.23e4	91.7%

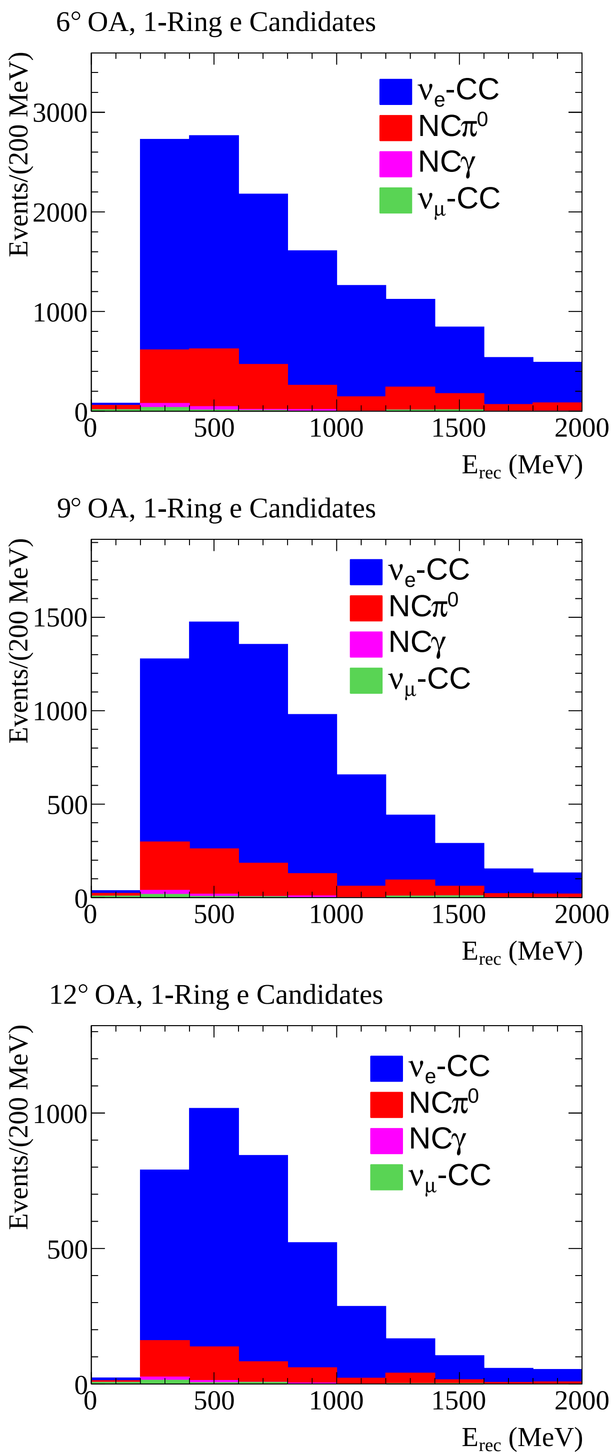

FIG. 75. The predicted 1Re candidates in bins of reconstructed energy for off-axis angles of 6°, 9° and 12°. The rates are normalized to a neutrino mode exposure with 5×10^{21} protons on target.

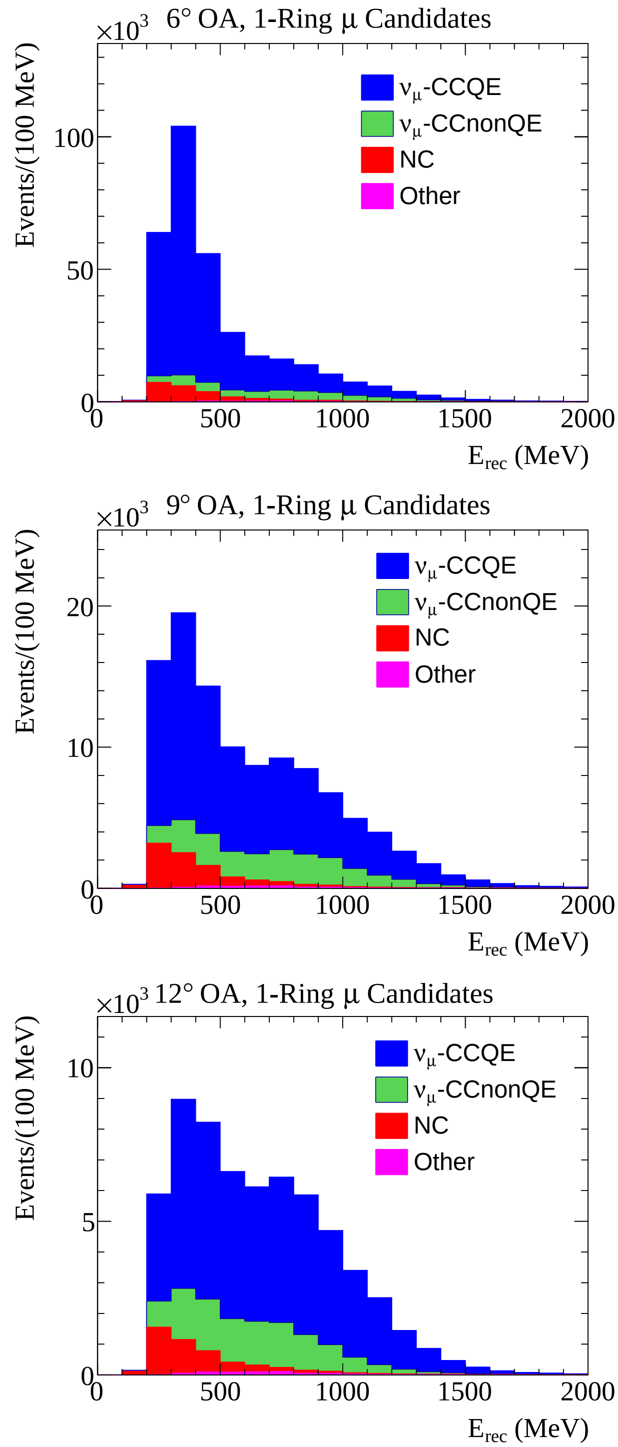

FIG. 76. The predicted 1Rμ candidates in bins of reconstructed energy for off-axis angles of 6°, 9° and 12°. The rates are normalized to a neutrino mode exposure with 5×10^{21} protons on target.

VII. CONCLUSION

The proposed NuPRISM detector has the potential to address the remaining systematic uncertainties that are not well constrained by ND280. In particular, this detector can constrain the relationship between measured lepton kinematics and incident neutrino energy without relying solely on rapidly-evolving neutrino interaction models. Since NuPRISM is a water Cherenkov detector, the neutral current backgrounds with large systematic uncertainties at Super-K, particularly NCπ^+ and NCπ^0, can be measured directly with a nearly identical neutrino energy spectrum. The ability to produce nearly monoenergetic neutrino beams also provides the first ever ability to measure neutral current cross sections as a function of neutrino energy. Finally, NuPRISM provides a mechanism to separate the many single-ring e-like event types to simultaneously constrain ν_e cross sections, neutral current background, and sterile neutrino oscillations.

The main long-baseline oscillation analysis presented in this note was a ν_μ disappearance measurement, since the effects of various cross section models on this measurement had already been well studied, which provided a useful basis for comparison. However, it is also expected that NuPRISM will provide a significant improvement to the ultimate T2K constraint on δ_{CP} by constraining neutral current backgrounds and electron-neutrino cross sections. Initial studies have also been presented that demonstrate the impact NuPRISM can have on both ν_e appearance measurements and anti-neutrino oscillation measurements. A realistic detector simulation and event reconstruction have been presented and are already use to study the ν_e cross section measurement potential. Additional analyses and sensitivities will be updated based on the realistic detector simulation.

Prior to the construction of the vertical water cavity, it is possible to begin the project with a "NuPRISM phase 0", in which the instrumented water volume is constructed first and operated on the surface near ND280. In this configuration, it is possible make low-background measurements of ν_e interactions, detailed measurements of neutron capture on Gd from charged current interactions, and provides an easily accessible setup for commissioning the detector calibration and verifying the detector modeling.

Cost estimates for NuPRISM are still preliminary, but initial quotes have been obtained for the most expensive components of the project: the civil construction and PMTs. Initial quotes have been received for these two items, which provides an initial cost estimate for the total project of US$16.3 million. There are still uncertainties associated with this cost estimate that will be reduced before the experiment proposal is submitted. More details regarding the project cost can be found in the appendix. Once funded, NuPRISM is expected to take less than 3 years to construct, based on the experience from the T2K 2 km detector.

[1] S. Bhadra *et al., "Proposal for the NuPRISM Experiment in the J-PARC Neutrino Beamline," Presented to the J-PARC PAC, July 2015, http://j-parc.jp/researcher/Hadron/en/pac_1507/pdf/P61_2015-5.pdf*

[2] *K. Abe et al. [T2K Collaboration], Phys. Rev. D* **91***, no. 7, 072010 (2015) [arXiv:1502.01550 [hep-ex]].*

[3] *A. A. Aguilar-Arevalo et al. [MiniBooNE Collaboration], Phys. Rev. Lett.* **110***, 161801 (2013) [arXiv:1207.4809 [hep-ex], arXiv:1303.2588 [hep-ex]].*

[4] *T. Dealtry et al. T2K-TN-172 (2014)*

[5] *C. H. Llewellyn Smith, Phys. Rept.* **3***, 261 (1972).*

[6] *R. A. Smith and E. J. Moniz, Nucl. Phys. B* **43***, 605 (1972) [Erratum-ibid. B* **101***, 547 (1975)].*

[7] *O. Benhar, A. Fabrocini and S. Fantoni, Nucl. Phys. A* **505***, 267 (1989).*

[8] *Melanie Day, Kevin S. McFarland, Differences in Quasi-Elastic Cross-Sections of Muon and Electron Neutrinos Phys.Rev. D86 (2012) 053003*

[9] *A. A. Aguilar-Arevalo et al. [MiniBooNE Collaboration], Phys. Rev. D* **81***, 092005 (2010) [arXiv:1002.2680 [hep-ex]].*

[10] *J. Marteau, Eur. Phys. J. A* **5***, 183 (1999) [hep-ph/9902210].*

[11] *M. Martini, M. Ericson, G. Chanfray and J. Marteau, Phys. Rev. C* **80***, 065501 (2009) [arXiv:0910.2622 [nucl-th]].*

[12] *M. Martini, M. Ericson, G. Chanfray and J. Marteau, Phys. Rev. C* **81***, 045502 (2010) [arXiv:1002.4538 [hep-ph]].*

[13] *M. Martini, M. Ericson and G. Chanfray, Phys. Rev. C* **84***, 055502 (2011) [arXiv:1110.0221 [nucl-th]].*

[14] *J. Nieves, I. Ruiz Simo and M. J. Vicente Vacas, Phys. Rev. C* **83***, 045501 (2011) [arXiv:1102.2777 [hep-ph]].*

[15] *K. Abe et al. [T2K Collaboration], Phys. Rev. D* **87***, no. 1, 012001 (2013) [Phys. Rev. D* **87***, no. 1, 019902 (2013)] [arXiv:1211.0469 [hep-ex]].*

[16] *N. Abgrall et al. [NA61/SHINE Collaboration], Phys. Rev. C* **84***, 034604 (2011) [arXiv:1102.0983 [hep-ex]].*

[17] *S. Dazeley, A. Bernstein, N. S. Bowden, R. Svoboda, Nucl. Instrum. Meth.* ***A607****, 616 (2009), arXiv:0808.0219.*

[18] *H. Ejiri, Phys. Rev. C* **48***, 1442 (1993). doi:10.1103/PhysRevC.48.1442*

[19] *H. Zhang [Super-Kamiokande Collaboration], "Neutron tagging and its application to physics in Super-Kamiokande IV," doi:10.7529/ICRC2011/V04/0353*

[20] *N. Abgrall et al. [NA61/SHINE Collaboration], Phys. Rev. C* **85***, 035210 (2012) [arXiv:1112.0150 [hep-ex]].*

[21] *K. Abe, N. Abgrall, Y. Ajima, H. Aihara, J. B. Albert, C. Andreopoulos, B. Andrieu and M. D. Anerella et al., Nucl. Instrum. Meth. A* **694***, 211 (2012) [arXiv:1111.3119 [physics.ins-det]].*

[22] *Yu. Kudenko (for the T2K Collaboration). Nucl. Instr. and Meth. A598 (2009) 289-295; K. Abe et al., (The T2K Collaboration) Nucl. Instr. and Meth. A 659 (2011) 106.*

[23] *D. Renker, and E. Lorenz, JINST 4 (2009) P04004.*

[24] *M. Yokoyama et al., Nucl. Instr. and Meth. A 610 (2009) 128; M.Yokoyama et al., Nucl. Instr. and Meth. A 622 (2010) 567; A. Vacheret et al., Nucl. Instr. and Meth. A 656 (2011) 69.*

[25] *Yu.Musienko, New developments in solid state photomultiplier, talk at the International Conference "Instrumentation for Colliding Beam Physics" (INSTR14), 24 February - 1 March 2014, Novosibirsk, Russia.*

[26] *K. Abe, T. Abe, H. Aihara, Y. Fukuda, Y. Hayato, K. Huang, A. K. Ichikawa and M. Ikeda et al., arXiv:1109.3262 [hep-ex].*

[27] *Y. Fukuda et al. [Super-Kamiokande Collaboration], Nucl. Instrum. Meth. A* **501***, 418 (2003).*

[28] *K. Abe, Y. Hayato, T. Iida, K. Iyogi, J. Kameda, Y. Kishimoto, Y. Koshio and L. .Marti et al., Nucl. Instrum. Meth. A* **737***, 253 (2014) [arXiv:1307.0162 [physics.ins-det]].*

[29] *O.Mineev et al., JINST 6 (2011) P12004; arXiv:1110.2651 [physics.ins-det].*

[30] *Y. Kudenko et al., Nucl. Instr. Meth. A469 (2001) 340.*

[31] *S. Nakayama et al. [Hyper-Kamiokande Working Group], "Hyper-K Tank", Talk at the 4th Open Meeting for the Hyper-Kamiokande Project,* `http://indico.ipmu.jp/indico/getFile.py/access?contribId=29&sessionId=4&resId=0&materialId=slides&confId=29`

[32] *MiniBooNE collaboration, Phys.Rev.Lett.102(2009)101802*

[33] *nuSTORM - Neutrinos from STORed Muons: Proposal to the Fermilab PAC, arXiv:1308.6822*

[34] *E. Wang, L. Alvarez-Ruso, Y. Hayato, K. Mahn and J. Nieves, Phys. Rev. D* **92***, no. 5, 053005 (2015) doi:10.1103/PhysRevD.92.053005 [arXiv:1507.02446 [hep-ph]].*

[35] *E. Akhmedov, Nucl. Phys. Proc. Suppl.* **188***, 204 (2009) [arXiv:0901.3450 [hep-ph]].*

[36] *S. Razzaque and A. Y. Smirnov, JHEP* **1505***, 139 (2015) [arXiv:1406.1407 [hep-ph]].*

[37] *G. D. Barr, T. K. Gaisser, S. Robbins and T. Stanev, Phys. Rev. D* **74***, 094009 (2006) [astro-ph/0611266].*

[38] *C. Consolandi [AMS 02 Collaboration], arXiv:1402.0467 [astro-ph.HE].*

[39] *K. Abe et al. [T2K Collaboration], Phys. Rev. D* **87***, 092003 (2013) [arXiv:1302.4908 [hep-ex]].*

[40] *Y. Nakajima et al. [SciBooNE Collaboration], Phys. Rev. D* **83***, 012005 (2011) [arXiv:1011.2131 [hep-ex]].*

[41] *B. G. Tice et al. [MINERvA Collaboration], [arXiv:1403.2103 [hep-ex]].*

[42] *Y. Nakajima,* `http://nuint11.in/final_nuint/cc%20quasi%20and%20nc%20elastic%20scattering/nakajima_nuint11.pdf`

[43] *VLyubushkin et al. [NOMAD Collaboration], Eur. Phys. J. C* **63***, 355 (2009) [arXiv:0812.4543 [hep-ex]].*

[44] *G. A. Fiorentini et al. [MINERvA Collaboration], Phys. Rev. Lett.* **111***, no. 2, 022502 (2013) [arXiv:1305.2243 [hep-ex]].*

[45] *R. Gran et al. [K2K Collaboration], Phys. Rev. D* **74***, 052002 (2006) [hep-ex/0603034].*

[46] *A. A. Aguilar-Arevalo et al. [MiniBooNE Collaboration], Phys. Rev. D* **83***, 052007 (2011) [arXiv:1011.3572 [hep-ex]].*

[47] *A. A. Aguilar-Arevalo et al. [MiniBooNE Collaboration], Phys. Rev. D* **83***, 052009 (2011) [arXiv:1010.3264 [hep-ex]].*

[48] *A. Rodriguez et al. [K2K Collaboration], Phys. Rev. D* **78***, 032003 (2008) [arXiv:0805.0186 [hep-ex]].*

[49] *C. Mariani et al. [K2K Collaboration], Phys. Rev. D* **83***, 054023 (2011) [arXiv:1012.1794 [hep-ex]].*

[50] *M. Hasegawa et al. [K2K Collaboration], Phys. Rev. Lett.* **95***, 252301 (2005) [hep-ex/0506008].*

[51] *O. Lalakulich and U. Mosel, Phys. Rev. C* **88***, no. 1, 017601 (2013) [arXiv:1305.3861 [nucl-th]].*

[52] *A. A. Aguilar-Arevalo et al. [MiniBooNE Collaboration], Phys. Rev. D* **81***, 013005 (2010) [arXiv:0911.2063 [hep-ex]].*

[53] *S. Nakayama et al. [K2K Collaboration], Phys. Lett. B* **619***, 255 (2005) [hep-ex/0408134].*

[54] *J. A. Formaggio and G. P. Zeller, Rev. Mod. Phys.* **84***, 1307 (2012) [arXiv:1305.7513 [hep-ex]].*

[55] *E. Hawker, Proceedings of the Second International Workshop on Neutrino-Nucleus Interactions in the Few-GeV Region, Irvine, CA, unpublished*

[56] *T. Kikawa et al. T2K-TN-132 (2013)*

[57] *E. Kearns et al. http://www.phy.duke.edu/ cwalter/nusag-members/2km-proposal-05-05-30.pdf (2005)*

[58] *S. Riboldi, R. Abbiati, A. Geraci, and Emilio Gatti. Experimental Comparison of State-of-the-Art Methods for Digital Optimum Filter Synthesis With Arbitrary Constraints and Noise.* IEEE Transactions on Nuclear Science*, 52(4):954–958, August 2005.*

[59] *S. Riboldi, A. Geraci, R. Abbiati, Emilio Gatti, and Giancarlo Ripamonti. A new method for LMS synthesis of optimum finite impulse response (FIR) filters with arbitrary time and frequency constraints and noises. In* 2002 IEEE Nuclear Science Symposium Conference Record*, volume 1, pages 198–202 vol.1, November 2002.*

[60] *E. Gatti, A. Geraci, S. Riboldi, and G. Ripamonti. Digital Penalized LMS method for filter synthesis with arbitrary constraints and noise.* Nuclear Instruments and Methods in Physics Research Section A: Accelerators, Spectrometers, Detectors and Associated Equipment*, 523(12):167–185, May 2004.*

[61] *A. Abba, F. Caponio, A. Geraci, and G. Ripamonti. Experimental implementation of LMS synthesis of optimum FIR filters with arbitrary time and frequency constraints and noises. In* 2011 IEEE Nuclear Science Symposium and Medical Imaging Conference (NSS/MIC)*, pages 862–865, October 2011.*

[62] *S. Riboldi, A. Pullia, F. Camera, S. Brambilla, and A. Geraci. Optimum synthesis of FIR filters with arbitrary time and frequency constraints for energy and time estimations in case of pulse-correlated noise. In* IEEE Nuclear Science Symposium Conference Record, 2007. NSS '07*, volume 1, pages 486–489, October 2007.*

[63] *R. Abbiati, A. Geraci, Emilio Gatti, and Giancarlo Ripamonti. Application of a Digital Technique for Timing of Events From Scintillation Detectors.* IEEE Transactions on Nuclear Science*, 53(6):3850–3854, December 2006.*

TABLE X. Summary of nuPRISM project costs, excluding any contingency. Costs taken directly from the T2K 2 km proposal are labeled with *

Item	Cost (US M$)
Cavity Construction, Including HDPE Liner	6.00
*Surface Buildings	0.77
*Air-Conditioning, Water, and Services	0.50
*Power Facilities	0.68
*Cranes and Elevator	0.31
*PMT Support Structure	1.27
3,215 8-inch PMTs	4.30
PMT Electronics	1.45
*PMT Cables and Connectors	0.13
Scintillator Panels	0.36
Water System	0.35
Gd Water Option	0.15
*GPS System	0.04
Total	16.31

Appendix A: Detector Costs

This appendix is intended to characterize the costs associated with building NuPRISM. Several companies have provided preliminary cost estimates for the cost drivers of the experiment, which allows for a preliminary estimate of the total project cost.

For many of the less expensive items, the costs presented here rely heavily on the experience from the T2K 2 km detector proposal, which was written in 2005 [57]. For now, we have assumed that the prices are the same as those listed in the 2 km detector, since inflation rates in Japan have stayed near zero during the 9 years since that proposal was written. The assumed exchange rate is 107 Japanese yen to the US$.

A summary of the total project cost is given in Table X, and each component is described in the following subsections. Note that these numbers do not contain any contingency, as was the case in the 2 km proposal.

The remaining item for which no price estimate is given is cost of acquiring or renting the experimental site. For the 2 km detector, the chosen site was initially owned by a private company before being acquired by Tokai village and offered to J-PARC to use at no cost. Other experiments in Japan, such as AGASA, instead rent the land from the owner. Since any solution for land acquisition will require input from J-PARC, and since the original 2 km site was acquired without any cost to the laboratory, no cost estimate for land acquisition is included in the total project cost at this time.

1. Civil Construction

As mentioned in Section IV B, two construction groups have been consulted for preliminary cost estimates for constructing the shaft. The first group evaluated the initial cost of the civil construction by scaling with the excavation volume based on prior vertical tunnel constructions. Table XI summarizes the initial cost estimation for each construction method.

TABLE XI. Summary of initial cost estimation for civil construction. Five methods are considered: Pneumatic Caisson (PC), Soil Mixing Wall (SMW), New Austrian Tunneling (NAT), Urban Ring (UR), and Cast in-situ diaphragm wall (RC). A 70 m deep boring survey is assumed.

(Unit: Oku JPY, roughly corresponds to Million USD)

Method	PC	SMW	NAT	UR	RC
Survey	0.1				
Designing	0.15				
Land preparation	0.15				
Construction	7.7	5.9	5.3∼6.1	7.5	7.5

The second company prefers the NAT method for constructing the shaft, and they estimate a total cost of US$6M, including the HPDE liner, although this number is contingent on a geological survey to confirm the rigidity of the earth in that region. This estimate is more consistent with the cost listed in the 2 km detector proposal, which was listed at US$9.3M, despite a much larger excavated volume that included the construction of an underground cavern.

2. Photomultiplier Tubes

Table XII shows a cost comparison of the various PMT options from Hamamatsu. The default design assumes 3,215 standard 8" PMTs, although several other options are being explored, as shown in the table. The cost of the newer Hybrid Photodetector (HPD) technology being considered for Hyper-K depends on the year in which the PMTs are requested, since further R&D is expected to bring the production costs down for these devices.

TABLE XII. The pricing scenarios from Hamamatsu for various PMT configurations are shown. All prices are given in Japanese Yen.

Name	QE%	Quantity	Price/PMT	Cost	Delivery
5" PMT	25	8,000	103,500	828M	any
5" PMT HQE	35	5,714	123,700	707M	any
8" PMT	25	3,215	143,000	460M	any
8" PMT HQE	35	2,296	170,500	391M	any
8" HPD HQE	35	2,296	209,000	480M	2016
20" PMT HQE	30	508	539,500	274M	2016
20" HPD HQE	30	508	520,000	264M	2016

The ETEL/ADIT company based in the UK and Texas has also been consulted for supplying PMTs to NuPRISM. They can provide 8" or 5" PMTs, but they do not have the APD or high-QE options available from

Hamamatsu. The provided quote for 3,000 8” PMTs is \$1,775 per tube, which is significantly higher than the Hamamatsu quote. However, further consultation is planned to determine the cost of the 5” PMT option and to explore multi-2-inch-PMT options.

3. PMT Electronics

Initial cost estimates for NuPRISM electronics were based on early HK presentations, where the cost per channel for the electronics was \$450 per channel. This included the estimate for the digitization, HV power supply, network and case components. Separate estimates for the cost per channel for an FADC option came to a lower value for the digitization part; so we might conservatively use HK's estimate for the cost per channel. Assuming that we are equipping 3,215 channels this results in \$1.45 million for NuPRISM electronics.

4. OD Scintillator Panels

TABLE XIII. Rough cost of one extruded scintillator counter of $2000 \times 200 \times 7$ mm^3 with WLS fiber readout.

Material/labor	cost in US\$
One extruded slab covered by a reflector	70
WLS fiber Y11, 6 m long, 2\$/m	12
Optical glue, 2 g/m, 0.3\$/g	3.6
Optical connectors 2×0.25	0.5
MPPC 2×10\$	20
Labor	13.9
Total	120

The rough cost estimation of one counter ($2000\times200\times7$ mm^3 is given in Table XIII. The total surface of the NuPRISM detector (10 m in diameter, 14 m in height) is about 600 m^2. About 3000 counters will be needed to cover the detector surface completely. The rough total cost of this veto detector (without mechanics and electronics) is estimated to be about 360 k\$US. Assuming similar production speed as obtained in the SMRD case it will take 12-14 months to extrude 3000 scintillator slabs of suitable dimensions and finally make all veto counters at the INR workshop.

5. Water System

The water system is modeled after the Super-K water system, just as was done for the 2 km detector. We have consulted South Coast Water for an estimate of the cost of each of the system components, which resulted in a cost of US\$0.35M. This is only slightly higher than the US\$0.32M cost assumed in the 2 km proposal.

By scaling from the running EGADS system, it is possible to estimate for adding the additional components needed to handle gadolinium to the baseline system described above. Including the extra equipment required to make the baseline water system Gd-capable primarily means adding filtration elements called nanofiltration. Beyond that, there would have to be a small standalone system for dissolving, pre-purifying, and then injecting the gadolinium sulfate, as well as a standalone system to capture the gadolinium whenever the NuPRISM tank needed to be drained for servicing. All of this would increase the total cost of the complete NuPRISM water system from US\$0.35M to US\$0.50M.

Appendix B: International Funding Status

Stage 1 status for NuPRISM can positively impact ongoing and future requests to international agencies to fund the NuPRISM detector. In Canada, an \$8 million grant request for NuPRISM R&D and capital funding from the Canadian Foundation for Innovations's 2016 (CFI) Innovation Fund competition is in progress. The review of this proposal will begin shortly after the PAC meeting, and stage 1 status is essential for this request to proceed. The UK will be submitting a new 3-year proposal for Hyper-Kamiokande R& D to the Science and Technology Facilities Counsil (STFC) in late 2016. If a technical design of NuPRISM with a refined cost estimate is available by that time, a request for a several million dollar contribution to NuPRISM can be included. In other NuPRISM collaborating countries, such as Switzerland, Russia, Poland, and the United States, stage 1 status will provide a basis for which new funding for NuPRISM can be sought.